3-D Structure of Forests at L-Band: Experiments Towards a Spaceborne Implementation

Matteo Pardini
Andrea Cantini
Konstantinos Papathanassiou
Fabrizio Lombardini

DLR

Institut für
Hochfrequenztechnik
und Radarsysteme

INTERNER BERICHT

DLR-HR-IB-551-2/2014

DLR

3-D Structure of Forests at L-Band: Experiments Towards a Spaceborne Implementation

Bearbeiter:	Dr. Matteo Pardini	5.02.2014 Datum
Betreuer:	Dr. Konstantinos Papathanassiou	5.02.14 Datum
Abteilungsleiter:	Dr. Gerhard Krieger	6.2.14 Datum
Institutsdirektor:	Prof. Dr. Alberto Moreira	6.2.14 Datum

Der Bericht enthält: 78 Seiten, Bilder, Tabellen, Literaturzitate

Signatur Bibliothek FZ-OP	Barcode Bibliothek FZ-OP

Dokument Nummer: DLR-IB-551-2/2014

Titel: 3-D Structures of Forests: Experiments Towards a Spaceborne Implementation

Verfasser: Matteo Pardini

Projekt:

Fachgruppe: Information Retrieval

Abteilungsleiter: Dr. Gerhard Krieger

Kurzbeschreibung: Due to its ecological importance, the monitoring of the vertical structure of forests is continuously raising the interest of the synthetic aperture radar (SAR) scientific community. In particular, SAR Tomography allows reconstructing the 3-D distribution of the radar power backscattered by a forest by combining more than two SAR acquisitions with baseline diversity. Beyond specific estimation algorithms, the link between the estimated tomograms (depending in general on frequency, polarization and acquisition geometry) and physical forest structure is essential for establishing potential applications.
The main objective of this work is to present and discuss the results of some airborne tomographic experiments, considering forest stands with different biomass levels and different species composition. The analysis has been carried out by processing an L-band multibaseline fully polarimetric data set acquired over the temperate forest of Traunstein (Germany) by means of the DLR's E-SAR platform, and by exploiting an auxiliary Lidar acquisition and a set of ground measurements. The effects of the weather conditions on the estimated profiles have been analyzed as well by processing data acquired after a dry and a rainy period. It is worth noting that the variability of the profiles with the environmental conditions can be seen as a critical aspect for the implementation of 3-D forest structure monitoring from space. For this reason, considering a single-pass interferometric implementation as proposed for the Tandem-L mission, the impact of the inhomogeneity of the interferometric coherences on structure estimation has been quantified.

Schlüsselworte: SAR, tomography, forest structure, forest dynamics, Tandem-L

Deutsches Zentrum für Luft- und Raumfahrt e.V.
Institut für Hochfrequenztechnik und Radarsysteme
Institutsdirektor Prof. Dr. Alberto Moreira
Oberpfaffenhofen - 82234 Weßling

Verteiler:

1 Stück Bibliothek Forschungszentrum Oberpfaffenhofen
1 Stück Institutsleiter Prof. Dr. Alberto Moreira
1 Stück Prof. Dr. Helmut Süß
1 Stück Dr. Gerhard Krieger
1 Stück Dr. Manfred Zink
1 Stück Dr. Andreas Reigber
5 Stück Information Retrieval and PolInSAR Gruppen

3-D STRUCTURE OF FORESTS AT L-BAND: EXPERIMENTS TOWARDS A SPACEBORNE IMPLEMENTATION

Technical Report

M. Pardini[1], A. Cantini[2], K. Papathanassiou[1], F. Lombardini[2]

[1] Deutsches Zentrum für Luft- und Raumfahrt (DLR)
Microwave and Radar Institute (HR) – Weßling (Germany)

[2] University of Pisa (Italy) – Department of Information Engineering

November 2013

The experiments presented in this report were carried out during the stay of A. Cantini in DLR-HR for his M.Eng. thesis work, supervised by M. Pardini (DLR-HR), K. Papathanassiou (DLR-HR) and F. Lombardini (Univ. of Pisa) between January and July 2013.

- This page intentionally left blank -

ABSTRACT

Due to its ecological importance, the monitoring of the vertical structure of forests is continuously raising the interest of the synthetic aperture radar (SAR) scientific community. In particular, SAR Tomography allows reconstructing the 3-D distribution of the radar power backscattered by a forest by combining more than two SAR acquisitions with baseline diversity. Beyond specific estimation algorithms, the link between the estimated tomograms (depending in general on frequency, polarization and acquisition geometry) and physical forest structure is essential for establishing potential applications.

The main objective of this work is to present and discuss the results of some airborne tomographic experiments, considering forest stands with different biomass levels and different species composition. The analysis has been carried out by processing an L-band multibaseline fully polarimetric data set acquired over the temperate forest of Traunstein (Germany) by means of the DLR's E-SAR platform, and by exploiting an auxiliary Lidar acquisition and a set of ground measurements. The effects of the weather conditions on the estimated profiles have been analyzed as well by processing data acquired after a dry and a rainy period. It is worth noting that the variability of the profiles with the environmental conditions can be seen as a critical aspect for the implementation of 3-D forest structure monitoring from space. For this reason, considering a single-pass interferometric implementation as proposed for the Tandem-L mission, the impact of the inhomogeneity of the interferometric coherences on structure estimation has been quantified.

- This page intentionally left blank -

TABLE OF CONTENTS

CHAPTER 1

INTRODUCTION

In the late 1970s spaceborne and airborne imaging radars began to play an important role in remote sensing, first for investigation of planetary surfaces, and later for Earth observation [*Campbell*, 2002]. Synthetic aperture radar (SAR) can map reliably the Earth surface and acquire information about its physical properties [*Olmested.*, 1993]. As the SAR systems operate in the microwave (cm to dm wavelength) regime of the electromagnetic spectrum and provide their own illumination, they can acquire information independently of meteorological conditions and sun illumination. The side-looking imaging geometry, together with pulse compression techniques and the synthetic aperture concept are employed to achieve geometric resolutions in the order of 1m with physical antennas of modest size. After the launch of the ESA satellite ERS-1 in 1991, the use of SARs as interferometers (InSAR) became popular and a series of research groups began to investigate intensively SAR technologies and techniques. Today, SAR configurations are extremely powerful tools for mapping the Earth surface.

1.1 Basics of SAR Imaging

Radar sensing has been developed on the basis of four technological principles [*Cumming*, 2004]. These are: 1) the ability of an antenna to emit a brief electromagnetic pulse in a precise direction, 2) the ability to detect, also with directional precision, the greatly attenuated echo scattered from a target, 3) the ability to measure the time delay between emission and detection and thus the range to the target, and 4) the ability to scan with the directional beam and so examine an extended area for targets. By using precisely phase-controlled signals, it is possible to achieve extreme enhancements of the application of the four physical principles. In this way, SAR systems can detect small Doppler shifts in signals from targets in motion relative to the radar, obtaining high imaging resolution [*Olmested*, 1993].

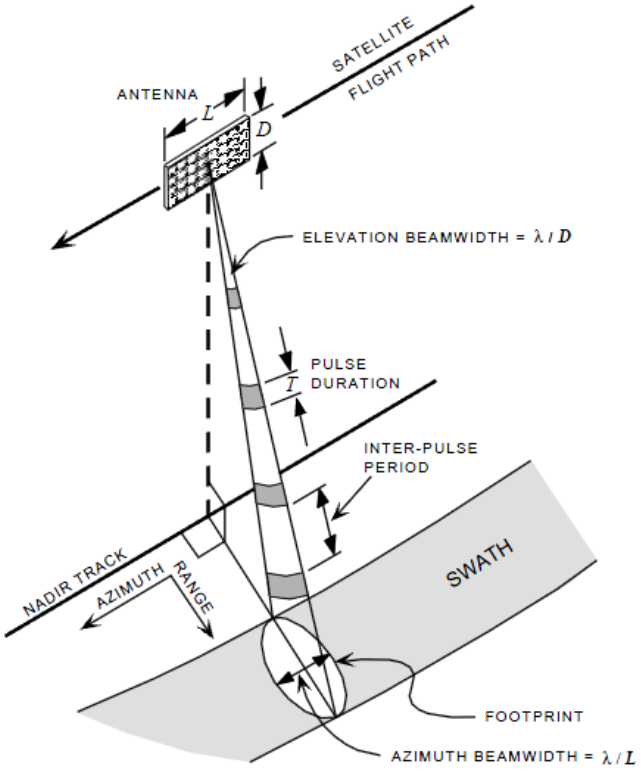

Figure 1.1 – Example of a SAR system with rectangular antenna (reproduced from [*Olmested*, 1993]).

In the classical imaging configuration for remote sensing, the radar is carried on an aircraft or spacecraft platform moving at uniform speed and altitude in order to realize the relative motion between the radar and the imaged (static) scene. The forward motion provides scanning in the along track (*azimuth*) direction as shown in Fig. 1.1, in the side looking mode. The radar beam is directed to the side (most commonly perpendicular) and down toward the surface. The beam is wide in the vertical direction and intersects the surface in an oval with the long axis extended in the across track (*range*) direction. Digitizing the signal in time provides scanning in the range direction.

To better understand how SAR processing can achieve high resolution in both azimuth and range direction, it is convenient to consider the SAR signal first in the range direction, then in the azimuth direction [*Cumming*, 2004]. In the range direction, the radar transmits a linear FM pulse (also called *chirp*) given by

$$S_{pul}(\tau) = w_r(\tau)\cos\left(2\pi f_0\tau + \pi K_r\tau^2\right), \tag{1.1}$$

where τ is the range time and K_r is the FM (frequency modulation) rate. The pulse envelope is usually approximated by a rectangular function:

$$w_r(\tau) = rect\left(\frac{\tau}{T_r}\right), \tag{1.2}$$

where T_r is the pulse duration. The signal or pulse bandwidth is a very important parameter, since it governs the range resolution and the sampling requirements and it is given by $|K_r|T_r$. It is possible to demonstrate

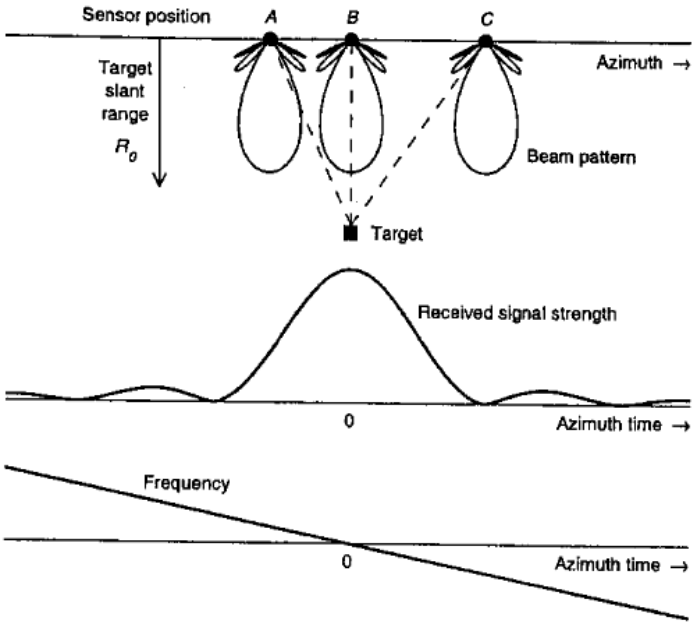

Figure 1.2 – Azimuth beam pattern and its effect on signal strength and Doppler frequency (reproduced from [*Olmested*, 1993]).

that, after a *matched filtering*, the range resolution (that it would be $\rho_r \approx cT_r / 2$ in absence of the phase modulation), is:

$$\rho_r \approx \frac{c}{2}\frac{1}{|K_r|T_r}. \tag{1.3}$$

After this filtering, normally called *pulse compression*, the result is a narrow pulse that improves the resolution of several times depending on the FM rate.

The received signal from a target has the same waveform as the transmitted signal, but is much weaker and has a frequency shift (SAR Doppler frequency) depending on the relative speed of the sensor (antenna) and the scatterer. As the platform advances, a target on the ground is illuminated by many hundreds of pulses. For each pulse, the strength and the Doppler frequency of the signal varies, as shown in Fig. 1.2. Approximating the curved Earth geometry as rectilinear and considering the squint angle equal to 0°, the *target exposure time*, T_a, defined as the time interval in which the target persists in the -3dB beam limits, is given by

$$T_a = 0.886\frac{\lambda R_0}{LV}, \tag{1.4}$$

where R_0 is the slant range when the radar is closest to the target, V is the speed of the platform and λ the center wavelength. In equation (1.4), the ratio $0.886\lambda / L$ is the azimuth beam width of a beam pattern considered approximately shaped as $\mathrm{sinc}(tL / \lambda)$. Without any integration, the azimuth resolution is the projection of the beam width onto the ground and it is on the order of several hundreds of meters in an airborne case, and several kilometers in a satellite case [*Olmested*, 1993]. It can be demonstrated that the

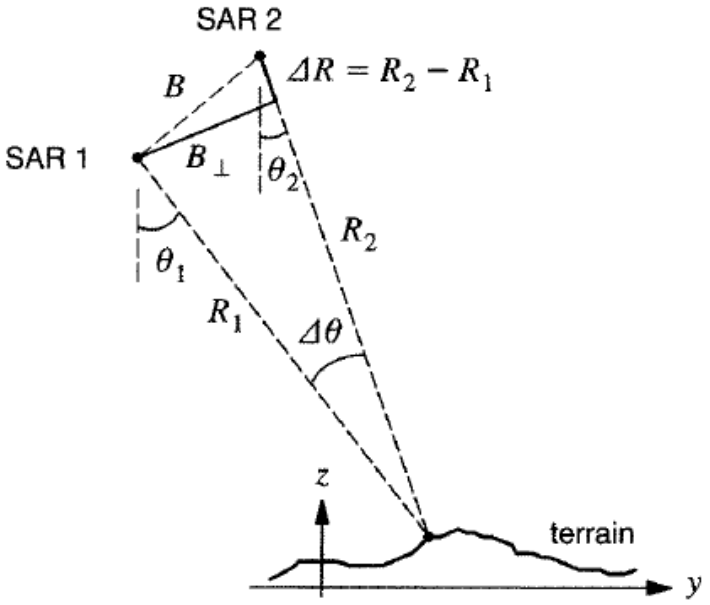

Figure 1.3 – Across-track SAR interferometric configuration (flight paths perpendicular to *z-y* plane). The y-axis denotes the ground range (reproduced from [*Bamler*, 1998]).

relative movement between the target and the platform results into a linear modulation of the Doppler frequency that makes the same effect of the chirp in range with *azimuth FM rate* given by:

$$K_a = \frac{2V^2}{\lambda R_0}. \tag{1.5}$$

To improve the azimuth resolution, it is therefore possible to synthesize a narrow beam width in azimuth, similarly to the synthesis of a narrow pulse in range. Since the beam width is inversely proportional to the antenna aperture, this processing is equivalent to synthesizing a large aperture, explaining in this way the name of *synthetic aperture* radar. It is possible to demonstrate that, taking advantage of the azimuth synthesis, the azimuth resolution in a SAR systems becomes:

$$\rho_a = \frac{L}{2}, \tag{1.6}$$

and it is independent of range, velocity or wavelength, reaching values on the order of meters depending on the size of the antenna.

From a system point of view, the SAR imaging process can also be seen to provide a geometric projection of the 3-D radar reflectivity function $\beta(x,y,z)$ into a 2-D cylindrical coordinates system (R,x), followed by a 2-D convolution with the azimuth-range point-spread function (PSF) $g(R,x)$, [*Bamler*, 1998], [*Gini*, 2005]:

$$y(R,x) = \left[\int \beta(x,y,z) R d\theta \exp\left(-\frac{4\pi}{\lambda} R\right)\right] \otimes g(R,x) \tag{1.7}$$

where $y(R,x)$ is the complex SAR image, R is the distance between the sensor and the target (slant-range), θ is the look angle, and "$\otimes$" denotes the convolution operator.

1.2 SAR Interferometry

The term SAR interferometry or Interferometric SAR (abbreviated, InSAR) is used for those methods that employ at least two complex-valued SAR images to derive more information about the focused object than present in a single SAR image by exploiting the phase of the SAR signals [*Bamler*, 1998]. For a second SAR image to provide additional information, at least one imaging parameter (e.g. flight path, acquisition time, wavelength) must be different compared with the first image. One of the most important interferometric configurations is the cross-track one, mainly used to reconstruct the Earth topography. Two SARs fly on parallel tracks and view the terrain from slightly different directions (Fig. 1.3). The separation of the flight paths is called *baseline* B, and its component perpendicular to the look direction is the *orthogonal baseline* $B_\perp$. Given the sensor locations and the two ranges R_1 and R_2, every point of the Earth surface can be mapped back into the space by triangulation. To measure the difference ΔR between the two ranges precisely, InSAR techniques use phase information. After compensating the range and azimuth differences existing between the two acquisitions by *co-registering* the two complex images

$$\begin{aligned} y_1(R,x) &= |y_1(R,x)| \exp\{j\varphi_1(R,x)\}, \\ y_2(R,x) &= |y_2(R,x)| \exp\{j\varphi_2(R,x)\}, \end{aligned} \tag{1.8}$$

the *interferogram* $v(R,x)$ can be obtained by:

$$v(R,x) = y_1(R,x)\, y_2^*(R,x) = |y_1(R,x)|\,|y_2(R,x)| \exp\{j\varphi(R,x)\}, \tag{1.9}$$

where

$$\varphi(R,x) = \varphi_1(R,x) - \varphi_2(R,x) \tag{1.10}$$

is the *interferometric phase*. An additional phase component is present on the interferometric signal due to the curvature of the reference surface, called the flat-Earth phase. If the orbits of the interferometric pair are known, the flat-Earth phase is estimated using the orbital and metadata information and subtracted from the complex interferogram. Assuming that the scattering phase is the same in both images, the interferometric phase can be used to determine the terrain height for each pixel according to the following relationship [*Rosen*, 2000], [*Bamler*, 1998]:

$$z = H - r\cos\left[\xi - \cos^{-1}\left(-\frac{\varphi\lambda}{4\pi B_\perp}\right)\right], \tag{1.11}$$

where H is the platform altitude and ξ is the baseline tilt angle (the angle between the baseline and the ground range axis). In this way, cross-track InSAR systems can be used to produce Digital Elevation Models (DEMs).

The interferogram formulation (1.9) can not be used directly due to the presence of *speckle*, a multiplicative noise which is originated by the backscattering from extended (natural) targets, causing difficulties for image interpretation. Due to the stochastic nature of the speckle noise, a way to estimate robustly the interferometric phase is to make use of statistical averaging. For this reason, the fundamental InSAR observable is the complex correlation coefficient γ (or *coherence*) between the two SAR images:

$$\gamma = \frac{\mathrm{E}\left\{y_1(R,x)\, y_2^*(R,x)\right\}}{\sqrt{\mathrm{E}\left\{\left|y_1(R,x)\right|^2\right\}\mathrm{E}\left\{\left|y_2(R,x)\right|^2\right\}}}, \tag{1.12}$$

where $E\{\cdot\}$ denotes the statistical expectation operator. By introducing $I = \sqrt{\mathrm{E}\left\{\left|y_1(R,x)\right|^2\right\}\mathrm{E}\left\{\left|y_2(R,x)\right|^2\right\}}$, it is easy to see that γ is related to the interferogram expression (1.9) by:

$$\gamma = \frac{E\{v(R,x)\}}{I}. \tag{1.13}$$

In practical application, as no more than one realizations of the two SAR images with the same speckle statistics can be acquired, it is assumed that the speckle is ergodic and the statistical average is substituted by the multilook operation, a complex average in range and/or azimuth directions. While the interferogram corresponds to the phase of γ and can be used to retrieve topographic information, the magnitude of γ is a quality parameter of the interferometric phase and consequently of the obtained DEM. Many reasons can reduce the correlation between the two SAR images. First of all, the receiver noise may decorrelate the two images, i.e. $|\gamma| < 1$, reducing in this way the precision of the extracted information [*Bamler*, 1998]. On the other hand, decorrelation can also occur due to changes on the scene under investigation or to particular scattering mechanisms related for instance to the presence of volumes like forests or ice. In this way, by analyzing the statistical correlation between two SAR images, it is possible to retrieve information about soil moisture changes, the thickness of the scattering layer (canopy thickness, penetration depth, etc), or to carry out object classification.

1.3 Polarimetric InSAR

Polarimetric SAR Interferometry (PolInSAR) is an innovative tool which combines the capability of interferometry to extract height information with polarimetric decomposition techniques in order to separate different scattering mechanisms, like ground and canopy cover. This separation and the consequential estimation of vertical structure parameters is achieved by relating the polarimetric-interferometric coherences to scattering models [*Cloude*, 1998], [*Papathanassiou*, 2001]. PolInSAR techniques are nowadays well-assessed for forest applications, and they can estimate forest height with a precision in the order of magnitude of 1m.

In [*Cloude*, 1998] the polarization-dependent behaviour of backscattering was demonstrated and exploited for an improved interferometry. Using the $\{H,V\}$ polarisation basis, a generalization is possible of the classical scalar interferometry by starting from the following Pauli scattering vector in a single pixel in the case that a quad-pol system is available[2]:

[2] The dependency on pixel coordinates (R,x) has been dropped for the sake of notation simplicity. The notation y_{ij}, where $i,j \in \{H,V\}$, is related to a SAR image acquired by a radar system with the incidence wave transmitted in polarization i and the backscattered wave observed in polarization j.

$$\mathbf{k} = \frac{1}{\sqrt{2}}\left[y_{HH} + y_{VV}, y_{HH} - y_{VV}, 2y_{HV}\right]^T, \tag{1.14}$$

where the superscript $(\cdot)^T$ denotes the transpose operator and the vector $\mathbf{k}$ is 3-dimensional due to the assumption of backscattering from a reciprocal scatterer ($y_{HV} = y_{VH}$). The resulting 6×6 interferometric-polarimetric covariance matrix is [*Cloude*, 1998]:

$$\mathbf{T}_6 = E\left\{\begin{bmatrix}\mathbf{k}_1 \\ \mathbf{k}_2\end{bmatrix}\begin{bmatrix}\mathbf{k}_1^H & \mathbf{k}_2^H\end{bmatrix}\right\} = \begin{bmatrix}\mathbf{T}_{11} & \boldsymbol{\Omega}_{12} \\ \boldsymbol{\Omega}_{12}^H & \mathbf{T}_{22}\end{bmatrix} \tag{1.15}$$

where the superscript $(\cdot)^H$ denotes the Hermitian transpose operator, $\mathbf{k}_i$ is the Pauli scattering vector for the *i*-th acquisition, and:

$$\begin{aligned}\mathbf{T}_{11} &= E\left\{\mathbf{k}_1\mathbf{k}_1^H\right\}, \\ \mathbf{T}_{22} &= E\left\{\mathbf{k}_2\mathbf{k}_2^H\right\}, \\ \boldsymbol{\Omega}_{12} &= E\left\{\mathbf{k}_1\mathbf{k}_2^H\right\}.\end{aligned} \tag{1.16}$$

The objective is to generalize the concept of interferogram to embed all the possible combinations of polarization states. Introducing a couple of normalized complex column vectors $(\boldsymbol{\omega}_1, \boldsymbol{\omega}_2)$ that represent two generic scattering mechanisms, the projections of $(\mathbf{k}_1, \mathbf{k}_2)$ on the subspace spanned by $(\boldsymbol{\omega}_1, \boldsymbol{\omega}_2)$ are:

$$\left[\mu_1, \mu_2\right] = \left[\boldsymbol{\omega}_1^H\mathbf{k}_1, \boldsymbol{\omega}_2^H\mathbf{k}_2\right]. \tag{1.17}$$

Thus, by changing the vectors $(\boldsymbol{\omega}_1, \boldsymbol{\omega}_2)$ it is possible to generate any kind of interferogram with corresponding interferometric phase given by:

$$\varphi_{12} = \arg\left(\boldsymbol{\omega}_1^H\boldsymbol{\Omega}_{12}\boldsymbol{\omega}_2\right). \tag{1.18}$$

In this way, assuming that at least two orthogonal scattering mechanisms *i* and *j* can be separated by means of a proper choice of the combination vectors[3], it is possible to achieve additional information for instance by computing the phase difference between the corresponding interferograms:

$$\Delta\varphi_{ij} = \arg\left(\mu_{1i}\mu_{2i}^*\right) - \arg\left(\mu_{1j}\mu_{2j}^*\right), \tag{1.19}$$

which represents the phase difference between the effective phase centers of the scattering mechanisms *i* and *j*. [*Cloude*, 1998]. Considering forest scenarios, if two orthogonal scattering mechanisms could be received from the ground and the vegetation layer, the difference between the corresponding height centroids could be simply obtained from (1.19), thus allowing to estimate the elevation of the top of the canopy. Unfortunately, experimental analyses showed the presence of both volume and scattering contributions in all polarizations, so that orthogonal scattering mechanisms, even though present, are not the only ones received from the polarimetric sensors. Recent advances have shown different ways to obtain more significant scattering

[3] It is possible to demonstrate that two orthogonal scattering mechanisms can be obtained by means of the eigendecomposition of the polarimetric-interferometric coherence matrix [*Cloude*, 1998].

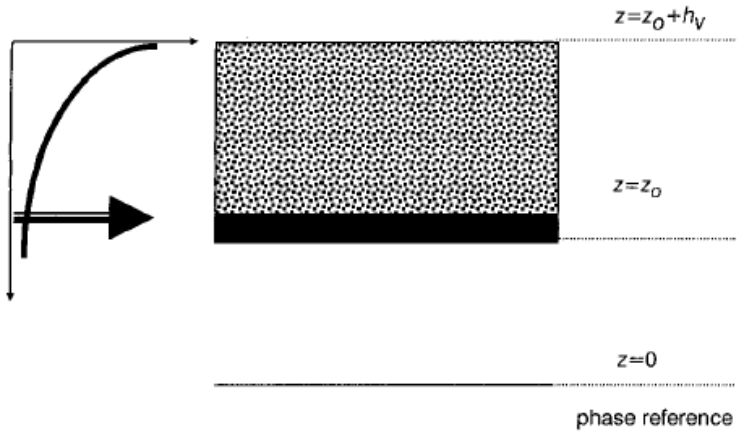

Figure 1.4 – Schematic representation of the RVOG model (reproduced from [*Papathanassiou*, 2001]).

mechanisms in terms of separation between ground and volume scattering [*Lopez*, 2010].

More complex model-based inversion algorithms have then been developed to estimate the parameters of different scatterers in the same cell [*Lopez*, 2010], [*Cloude*, 2003]. For SAR acquisitions over forest stands, a simple but reliable model is the Random Volume over Ground (RVoG), which relates the observed multipolarimetric-interferometric coherences with the forest parameters. Basically, two layers are assumed to be present in the height dimension, as shown in Fig. 1.4. A ground scatterer is located at height $z = z_0$ with scattering amplitude per volume unit m_G, whereas the vegetation layer is seen as a volume of thickness h_V, filled with randomly oriented particles, and scattering amplitude m_V. According to the model, it is possible to express the complex interferometric coherence $\gamma(\boldsymbol{\omega})$ associated to a generic scattering mechanism $\boldsymbol{\omega}$ as follows:

$$\gamma(\boldsymbol{\omega}) = \exp(j\phi_0)\frac{\gamma_V + m(\boldsymbol{\omega})}{1 + m(\boldsymbol{\omega})}, \tag{1.20}$$

where ϕ_0 denotes the ground phase (which is a linear function of the ground height through the baseline-dependent height-to-phase conversion factor k_z), and

$$m(\boldsymbol{\omega}) = \frac{m_G(\boldsymbol{\omega})}{m_V(\boldsymbol{\omega})}\exp\left(-\frac{2\varepsilon h_V}{\cos\theta_0}\right) \tag{1.21}$$

is the effective ground-to-volume amplitude ratio. In (1.20) and (1.21) γ_V and ε indicate the complex coherence accounting for the volumetric contribution alone and the extinction coefficient through the volume, respectively, respectively, and θ_0 is the incidence angle. In [*Cloude*, 2003] a three-stage inversion method has been tested by employing a simulated coherent electromagnetic scattering model and its effectiveness in parameter estimation, especially forest height, has been validated when at least one polarimetric channel can be found where the ratio $m(\boldsymbol{\omega})$ is small. Since then, forest height estimation matured and developed from a pre-operational to an operational PolInSAR product that has been validated in the frame of several campaigns over a wide range of forests, terrain and environmental conditions. The limitations of the individual inversion approaches and the error propagation through them are today well

understood as well as the options available to compensate for them.

As a final note, Multi-Baseline (MB) PolInSAR inversion approaches, in which at least three acquisitions are coherently combined together, have been investigated recently. In [*Lee*, 2011], it has been shown that MB approaches are useful to reduce constraints for single baseline PolInSAR inversion such as non-volumetric decorrelation effects and the height sensitivity of the vertical wavenumber. Moreover, MB PolInSAR inversion could contribute to compensate and/or filter out inversion results with strong height errors, improving significantly the accuracy of the estimation of the forest height.

1.4 SAR Tomography: 3D imaging with multiple baselines

Assuming that just one single target is present inside the resolution cell, InSAR estimates the height of its scattering centroid and outputs a map which establishes a correspondence between each pixel of the scene and the height of the scatterer inside them, i.e. a DEM. However, this hypothesis may not be verified in real scenarios where usually one resolution cell can be characterized by multiple superimposed backscattering responses. As a result, the single-scatterer hypothesis is not sufficient to characterize the radar signal. For instance, in urban areas it would be useful to resolve scattering mechanisms coming from the basis and the top of the buildings. In natural areas like forests, depending on the carrier frequency, different contributions come from ground, tree trunks, or canopy, the latter contribution being generally modeled as *volume scattering*. In these cases, as a result of the combination of multiple contributions, any kind of single-baseline InSAR processing cannot resolve them and returns just an estimate of the height of the scattering centroid. The generation of a synthetic aperture along the cross-range direction (i.e. in elevation) with height resolution capability is a possible solution to overcome this limitation. This can be obtained by exploiting information acquired by K passes of the radar platform with different cross-track baselines, and by coherently combining them in order to get a profile of the power backscattered from targets placed at different heights inside the same range-azimuth resolution cell. This kind of MB techniques are commonly referred to as SAR Tomography (Tomo-SAR). In the last decade, Tomo-SAR techniques have been developed by different European and not research groups in the SAR community, growing as a consequence very fast.

Consider the acquisition geometry of Fig. 1.5, where a set of K SAR images is acquired, corresponding to K nominal sensor flight tracks shifted along the cross-range direction. $K-1$ images (*slaves*) are supposed to be co-registered with respect to a reference master image. The flat-Earth phase is assumed to be compensated. The complex amplitude received by the k-th sensor of this interferometric array can be expressed as [*Fornaro*, 2003]

$$y_k(R,x) = \iint g(R',x') \int \beta(R',x',z) \exp\left(j \frac{4\pi B_{\perp k} z}{\lambda R} \right) dR'dx'dz, \tag{1.22}$$

where $g(R',x')$ is the post-focusing 2-D SAR impulse response, (R',x') are the dummy ntegration variables for the range-azimuth coordinates, $B_{\perp k}$ is the k-th baseline orthogonal to the line of sight, λ is the radar

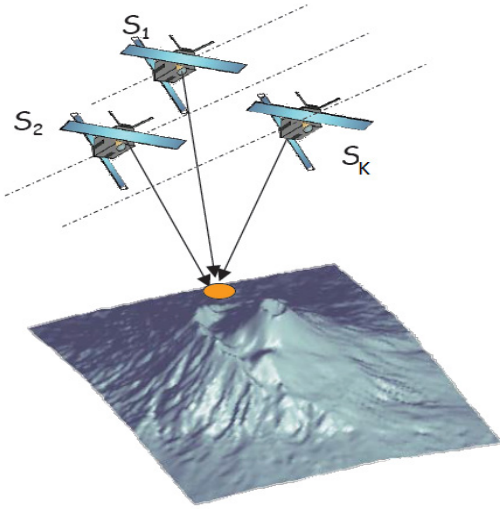

Figure 1.5 – MB acquisition with *K* sensors (reproduced from [*Tebaldini*, 2010]).

wavelength, and $\beta(R',x',z)$ is the scene reflectivity function. After some manipulations (see [*Fonaro*, 2003] for details), $y_k(R,x)$ can be rewritten as:

$$y_k(R,x) = \int \beta(R,x,z)\exp\left(j\frac{4\pi B_{\perp k} z}{\lambda R}\right)dz\,. \tag{1.23}$$

Assuming for the moment that the orthogonal baselines are uniformly distributed, equation (1.23) shows that a Fourier relation exists between SAR data and the target projection. Hence, $\beta(R,x,z)$ can be obtained by collecting all the samples $y_k(R,x)$, with $k=1,...,K$, and performing a Discrete Fourier Transform of the observable vector $\mathbf{y}=\left[y_1(R,x),...,y_K(R,x)\right]^T$ in the height-dependent spatial frequencies domain, as follows [*Fornaro*, 2003]:

$$\hat{\beta}(R,x,z) = \sum_{k=1}^{K} y_k(R,x)\exp(-j2\pi B_{\perp k}\omega_z)\,, \tag{1.24}$$

where

$$\omega_z = \frac{2z}{\lambda R} \tag{1.25}$$

is a spatial frequency in the height dimension. Let *d* and *L* be the sampling distance and the overall length of the synthetic aperture along the cross-range dimension, respectively. The achievable (geometric) Rayleigh resolution in the *z*-direction is given by [*Reigber*, 2000]:

$$\delta_z = \frac{\lambda R}{2L}\,. \tag{1.26}$$

According to the Nyquist criterion, an upper bound can be found to the sampling distance d in order to avoid height ambiguities [*Reigber*, 2000]:

$$d \leq \frac{\lambda R}{2\Delta H}, \tag{1.27}$$

where ΔH is height interval in which the scattering of the target of interest is included.

At least in principle, the sampling (i.e. baseline) distance should be kept uniform to properly reconstruct the vertical backscattering profiles of the scene. However, due to practical constraints, it is almost impossible to keep a constant baseline separation for all the tracks both in airborne and in spaceborne acquisitions. Furthermore, the limited number of sensor passes often results in a strongly undersampled observable vector, leading to increased sidelobes. As a consequence, the imaging quality worsens with respect to the ideal case, in terms of contrast and height ambiguities, as anomalous side and grating-lobes can arise [*Gini*, 2005], [*Reigber*, 2000], [*Fornaro,* 2005]. Many approaches have been proposed in the literature to solve this problem. In particular, research efforts have been spent to cast the problem of the height profile estimation in a more general signal processing framework. Spectral estimation approaches in the array processing framework have also proposed and successfully tested [*Gini*, 2005], [*Lombardini*, 2000]. In this latter framework, the Tomo-SAR output is the backscattered power calculated in a statistical sense:

$$P(z) = \mathrm{E}\left\{\left|f(z)\right|^2\right\}. \tag{1.28}$$

1.5 Objective of the thesis

This work deals with radar remote sensing techniques for monitoring forest vertical structure and biomass. In a more general perspective, the understanding of the relationship between forest vertical structure and biomass distribution gives access to the characterization of the terrestrial carbon budget. Classical PolInSAR techniques, using two-layer random media-scattering model, can estimate forest height, which is a proxy to biomass estimates in homogenous environments [*Papathanassiou*, 2001]. To increase this potentiality, many authors have proposed the reconstruction of vertical forest profiles by means of Tomo-SAR using high-resolution spectral analysis techniques [*Lombardini,* 2005]. Until now, these developments have been tested only with airborne data, as no suitable space borne data are available. However, spaceborne implementations of SAR tomographywith low carrier frequencies over forests are particularly appealing when considering applications on a global scale. In fact, while L- or P-band signals can penetrate through the forest volume until the ground and "interact" with its structure, a space borne platform of the latest generation can guarantee high coverage, high resolution and frequent revisit time, thus allowing to monitor forest ecosystem changes.

For these reasons, several research groups are currently working to extend tomographic techniques to a spaceborne implementation. In this regard, remarkable is the importance of tomographic techniques for the P-band ESA Biomass mission (accepted for realization) and the L-band DLR Tandem-L mission proposal. In both of them, forest vertical structure constitutes an important product. One of the main limitations of speceborne acquisitions is constituted by the *temporal decorrelation* between two different revisits of the satellite. To overcome these problems, two solutions are possible: (*i*) change data processing mode, i.e. move from a tomographic mode to a differential tomographic mode [*Lombardini, 2005*] in which the temporal

dimension is explicitly taken into accont, or (*ii*) change data acquisition mode, i.e. acquire single-pass temporal decorrelation-free PolInSAR data. The latter solution has already been implemented for the DLR TanDEM-X mission and constitutes the core of the Tandem-L proposal. Therefore, the inputs of the tomographic problem are not the complex images, but the complex single-pass coherences acquired with varying baselines. In this case, the so-called *coherence tomography* (CT) is a possible solution to the structure estimation problem. The vertical reflectivity is represented as a weighted sum of given functions, and the weights can be estimated from the available multibaseline coherences.

On the other hand, beyond the technological implementation of Tomo-SAR from space, many scientific questions are still open in multidimensional forest remote sensing, and this thesis contributes to the answers. First of all, it is important to assess the performance of CT techniques in reconstructing the forest vertical profiles. Secondly, the sensitivity of the L-band vertical profiles to vegetation (biomass) components has to be addressed. Thirdly, it is interesting to evaluate how different weather conditions can change the profiles, and to quantify the sensitivity of different profile components to these changes. Fourthly, since for a spaceborne implementation the revisit time is on the order of some days, it is very likely that the acquisitions will be carried out in different weather conditions. It is therefore of interest to quantify the changes in the vertical profiles induced by the combination of coherences referring to different conditions.

The analyses reported in this thesis have been carried out by means of simulated and real MB SAR data. Concerning the real data, an L-band multibaseline fully polarimetric data set has been processed. The data set was acquired by the Microwaves and Radar Institute of DLR in 2008 over the temperate forest of Traunstein (south of Germany) using the DLR's E-SAR platform, with auxiliary LIDAR mapping and ground measurements. This radar data set is particularly valuable as MB acquisitions were performed on different days, before and after a heavy rainy event.

This report is structured as follows.

In Chapter 2, the methods used for the proposed analysis will be described. Two classical tomographic estimators, the Fourier-based beamforming and the adaptive beam forming based on the Capon spectral estimator, are described. Then, the RELAX estimator is presented. In this thesis work, RELAX has been employed to separate the ground and volume layer in order to quantify their individual backscattering powers. Finally, vertical profile estimation by means of CT is recalled. In the frame of this thesis, for the sake of simplicity, we considered the Legendre polynomials as an expansion basis, as it is common in the literature.

In Chapter 3 the performance of Legendre-based CT in the reconstruction of the vertical profiles of the vegetation is derived and analysed by means of simulated data. For this analysis, three different vertical structures have been modeled with Gaussian functions. Moreover, different acquisition geometries, different G2V ratios and other forest parameters have been considered and the effects on the CT profiles quantified.

In Chapter 4, the results of the real data processing are reported. First of all, the test site, the radar data set and the available ground measurements are presented. Then the experimental results are reported and discussed. By means of two acquisition days, one before and one after a rainfall, the rain-induced effects on

the estimated profiles are analyzed and quantified. In particular, profiling solutions are considered in which low spatial frequency components are employed to reconstruct the profile. This can be realized by using the Legendre CT inversion with a low number of basis functions.

Finally, Chapter 5 draws the conclusions of the entire work, and some future directions of investigation are proposed.

- This page intentionally left blank -

CHAPTER 2

METHODS

2.1 Fourier-based beamforming estimator

As reported in Section 1.4., spectral estimators can be employed to reconstruct the vertical profile in the tomographic framework. The simplest way to make a spatial spectral estimation is to apply the *classical Fourier-based beamforming* (BF) filtering to the observable MB data vector $\mathbf{y}$ [*Gini*, 2005], [*Stoica*, 1997], which collects the SLC samples $y_k(R,x)$, $k=1,\ldots,K$. As usual in SAR imaging, N looks are considered to reduce statistical variations, e.g. multiple homogenous adjacent pixels. After selecting one image as master, the phase variations of a point-like scatterer of each image pixel with respect to the master pixel can be expressed by means of the K-dimensional *steering vector* $\mathbf{a}(z)$:

$$\mathbf{a}(z)=\left[1,\exp\left(j\frac{4\pi B_{\perp 1}}{\lambda R}z\right),\ldots,\exp\left(j\frac{4\pi B_{\perp k}}{\lambda R}z\right)\right]^T. \tag{2.1}$$

The *k*-th element of the steering vector is given by:

$$\left[\mathbf{a}(z)\right]_k=\exp\left(j\frac{4\pi B_{\perp k}}{\lambda R}z\right)=\exp\left(jk_{z,k}z\right) \tag{2.2}$$

where $k_{z,k}=4\pi B_{\perp k}/(\lambda R)$ is the vertical wavenumber of the *k*-th SAR image. Of course, at the master track it results $k_{z,k}=0$. The N-look estimate[4] of the covariance matrix $\mathbf{R}_y$ of vector $\mathbf{y}$ is given by:

$$\hat{\mathbf{R}}_y=\frac{1}{N}\sum_{n=1}^{N}\mathbf{y}(n)\mathbf{y}^H(n), \tag{2.3}$$

[4] The expression in (2.3) coincides with the maximum likelihood estimate of the data covariance matrix in the case in which the data vector is complex Gaussian.

where $\mathbf{y}(n)$ is the data vector for the n-th look. Using $\hat{\mathbf{R}}_y$, the beamforming spectrum can be obtained as [*Gini*, 2005]:

$$\hat{P}_{BF}(z) = \frac{\mathbf{a}^H(z)\hat{\mathbf{R}}_y\mathbf{a}(z)}{K^2}. \tag{2.4}$$

The BF estimated tomograms, although radiometrically linear, can be strongly affected by anomalous sidelobes with a non-uniform baseline distribution. Moreover, a limited resolution downgrades the performance of this tomographic processor. For this reason, in this work the non-model based adaptive (data dependent) filterbank Capon (ABF) method is used (instead of BF) to achieve a better resolution and to make the tomographic processing more robust to a non-uniform baseline distribution.

2.2 Adaptive spectral estimator (Capon)

In this work, airborne L-band ESAR data acquired during the TempoSAR 2008 campaign are used to investigate the impact of different environmental conditions on the estimated tomographic profile. Under these experimental conditions, the Fourier-based BF technique is limited by the low number of flight tracks and their irregular distribution [*Lombardini,* 2003]. With this conventional tomographic focusing based on Fourier-transforms, an ideal point-spread function cannot be obtained from such data. Anomalous side- and grating-lobes of the point-spread function can be observed mainly due to the non-uniform distribution of the tracks. However, experiments have demonstrated that adaptive (data-dependent) spectral estimators produce better imaging quality than Fourier methods with a limited and not fully sampled overall baseline.

The Capon method is a non-model based adaptive method, originally derived for time-series analysis of seismic signals [*Capon,* 1969]. Using a bank of (bandpass) filters, this estimator allows to adaptively reject interference coming from noise and scattering from other directions than the selected one, varying the shape of its frequency response during the spectral scan depending on the input data. The array concept can also be implemented in a tomographic sense. Indeed, K repeated flight tracks over the area of interest synthesize a non-uniform cross-track array of K phase centers. After motion compensation, K registered complex SAR images are produced from the acquired data.

As already stated in Section 1.4, the purpose of a (non-model based) tomographic spectral estimator is to reconstruct the profile of the backscattered power along height for a given range-azimuth cell, i.e. to estimate the backscattered power $P(z)$ from the MB multilook data. The Capon method adaptively designs an array re-phasing filter $\mathbf{h}(z)$ that passes the signal component coming from height z in $\mathbf{y}(n)$ without distortion and, at the same time, attenuates all the other signal components from different heights as much as possible. From an algebraic point of view, the filter is designed in order to solve the following optimization problem [*Stoica*, 1997]:

$$\arg\min_{\mathbf{h}(z)} \mathbf{h}(z)\hat{\mathbf{R}}_y\mathbf{h}(z) \text{ subject to } \mathbf{h}^H(z)\mathbf{a}(z) = 1. \tag{2.5}$$

The filter impulse response optimizing (2.5) is:

$$\mathbf{h}(z) = \frac{\hat{\mathbf{R}}_y^{-1}(z)\mathbf{a}(z)}{\mathbf{a}^H(z)\hat{\mathbf{R}}_y^{-1}(z)\mathbf{a}(z)}, \tag{2.6}$$

and the resulting Capon estimate of the intensity distribution is given by:

$$\hat{P}_{ABF}(z) = \mathbf{h}^H(z)\hat{\mathbf{R}}_y(z)\mathbf{h}(z). \tag{2.7}$$

These data-adaptive changes of the beam shape during the height scan allow gains in terms of both resolution and leakage (sidelobe) level. These improvements with respect to the BF estimator have been tested both with simulated data and with real data sets [*Lombardini*, 2003], becoming a standard imaging method as a matter of fact, also due to its simplicity of implementation.

2.3 Estimation of ground and volume powers

High resolution spectral estimators, as the ABF described in the previous section, allow to investigate how the backscattered power components change their distribution in height. In order to quantify these changes, one way is to measure the variation of the total power of vertical layers. According to a generally accepted assumption, the vertical profile of a forest can be divided in two different layers: the volume, which includes all the backscattering components with a phase center over the ground level, and the ground, which includes only the backscattered power from the terrain. In this work, the Multilook RELAX (M-RELAX) estimator [*Pardini*, 2011] is employed as a sub-optimal solution to separate these two different power contributions.

The M-RELAX separates ground and volume basing on a relaxation approach which uses a simplified coherence model for the two layers. This method, under the assumption that the ground and canopy are point-like scatterers (i.e. both with a vertical structure shaped as a Dirac-δ), estimates the ground topography, the volume phase center and the ground and volume scattering powers by means of an iterative method that for each iteration optimizes a one-dimensional functional [*Pardini*, 2012]. The M-RELAX estimates are obtained by minimizing [*Gini*, 2002] the following functional:

$$Q_N(\boldsymbol{\tau}_n, \mathbf{z}) = \sum_{n=1}^{N} \left\| \mathbf{y}(n) - \sum_{m=1}^{2} \tau_m(n)\mathbf{a}(z_m) \right\|^2, \tag{2.8}$$

where the vector $\mathbf{z} = [z_1, z_2]^T$ contains the height of the two scattering centroids to be separated, whose complex radar amplitudes in the I-th look are in the vector $\boldsymbol{\tau}_n = [\tau_1(n), \tau_2(n)]^T$. Employing an iterative method, the multidimensional non-linear minimization of (2.8) is transformed into a sequence of simpler one-dimensional problems. Indeed, after the initial estimation of z_1 and $\{\tau_1(n)\}_{n=1}^N$ (for instance using BF), the algorithm defines the residual data as

$$\mathbf{y}_2(n) = \mathbf{y}(n) - \hat{\tau}_1(n)\mathbf{a}(\hat{z}_1), \tag{2.9}$$

and replaces $\mathbf{y}(n)$ with $\mathbf{y}_2(n)$ in (2.8). By minimizing with respect to z_2 and $\tau_2(n)$, it results:

$$\hat{z}_2 = \arg\min_z \mathbf{a}^H(z)\hat{\mathbf{R}}_2\mathbf{a}(z), \tag{2.10}$$

$$\hat{\tau}_2(n) = \frac{1}{K}\mathbf{a}^H(\hat{z}_2)\mathbf{y}_2(n), \tag{2.11}$$

where $\hat{\mathbf{R}}_2$ is the multilook estimate of the covariance matrix of vectors $\mathbf{y}_2(n)$. Therefore, z_2 is estimated from the BF spectrum of the residual data. One complete iteration finishes repeating the previously described procedure also for z_1 and $\tau_1(n)$. Thus, after the convergence criterion is satisfied, the minimum between $\hat{z}_1$ and $\hat{z}_2$ and the related complex amplitudes are labeled as the ground height $\hat{z}_G$ and the ground complex amplitudes, respectively, whereas the other estimated height ($\hat{z}_V$) and the respective complex amplitudes are associated to the volume contribution. It is worth remarking that it has been demonstrated that M-RELAX is asymptotically statistically efficient when the scenario can be really approximated as two point-like scatteres [*Li*, 1996], but it is also robust to a model mismatch [*Gini*, 2002].

In this work, as the ground topography is available from LIDAR measurements, the separation of the ground and volume layers by means of the M-RELAX method is simplified. In fact, as z_G is known, only one iteration is needed to estimate z_V, and after the removal of the volume component (assumed δ-shaped) from the total signal, the ground power contribution is calculated as $\hat{P}_G = \sum_{n=1}^{N}\left|\hat{\tau}_G(n)\right|^2$. As z_G and $\{\hat{\tau}_G(n)\}_{n=1}^{N}$ are available, in order to consider all of the scattering components, the volume power P_V is estimated from the total backscattered power coming from the residual signal data $\mathbf{y}_V(n)$, after removing the ground component like in (2.9). Finally, the ground-to-volume power ratio μ is estimated as $\mu = \hat{P}_G / \hat{P}_V$.

2.4 Coherence Tomography

High-resolution non-parametric spectral analysis techniques have demonstrated the capability of imaging the vertical structure of forests using the estimated data covariance matrix $\mathbf{R}_y$, with remarkable results. However, especially considering space-borne implementations in which the interval between different passes is on the order of some days or weeks, the structure information contained in $\mathbf{R}_y$ is corrupted by temporal decorrelation. To overcome this issue, one way is to acquire single-pass (Pol)InSAR coherences (instead of a full covariance matrix) and to invert them by means of the so-called Coherence Tomography (CT) [*Cloude,* 2006]. The CT inversion decomposes the vertical profile on a set of (possibly, but not necessarily) orthogonal basis functions [*Cloude,* 2006]. In this way, the estimation of the vertical structure can be performed through the estimation of a set of coefficients, and it can be carried out with a low number of acquisitions. In terms of practical applications, the CT inversion is a good candidate for a spaceborne implementation of tomography for instance in the TanDEM-L mission proposal, in which two fully-polarimetric L-band SAR satellites would pass over the same area every 7-10 days forming a single-pass baseline each time without temporal decorrelation effects. However, an a priori knowledge is needed of the two height boundaries containing the scattering components, i.e. for a forest scenario the ground height

z_0 and the total height H_V. These two parameters can be estimated from the data, reaching around 10% error for the volume depth and 1.5m for the ground topography, or measured with external sources. Since in this work the main interest lies only on the estimated profiles, LIDAR maps of ground topography and forest height are used to obtain the required input parameters for the CT inversion.

The CT technique aims to estimate the vertical structure of forest scenarios using a multibaseline dataset (possibly multipolarimetric). At each baseline, corresponding to a vertical number k_z, the vertical profile $B(z)$ [5] generates the complex coherence $\gamma(k_z)$:

$$\gamma(k_z) = e^{jk_z z_0} \frac{\int_0^{H_V} B(z) e^{jk_z z} dz}{\int_0^{H} B(z) dz}, \tag{2.12}$$

with $0 \le |\gamma(k_z)| \le 1$. B(z) can then be decomposed on a function basis:

$$B(z) = \sum_m c_m f_m(z), \tag{2.13}$$

where $f_m(z)$ are the basis functions and c_m are the real-valued unknown expansion coefficients [*Cloude,* 2006]. As commonly done in the available literature, in this thesis, the Legendre polynomials are used as basis functions:

$$\begin{aligned} &f_0(z) = 1, \\ &f_1(z) = z, \\ &f_2(z) = \left(3z^2 - 1\right)/2, \\ &f_3(z) = \left(35z^4 - 30z^2 + 3\right)/2, \\ &\vdots \\ &f_m(z) = \frac{2m-1}{m} z f_{m-1}(z) - \frac{m-1}{m} f_{m-2}(z). \end{aligned} \tag{2.14}$$

As Legendre polynomials are defined over $[-1,1]$, the z axis needs to be rescaled from $[z_0, z_0 + H_V]$ to $[-1,1]$. For the sake of simplicity and with a slight abuse of notation, the variable z has been kept to indicate also the rescaled height axis. The values of the Legendre polynomials ranges in $[-1,1]$ and the first four polynomials are plotted in Fig. 2.1. After the height rescaling, equation (2.12) can be rewritten as

$$\gamma(k_z) = e^{jk_z z_0} e^{jk_V} \sum_m c_m \varphi_m(k_V), \tag{2.15}$$

where $k_V = k_z H_V / 2$ and $\varphi_m(k_V) = \int_{-1}^{1} f_m(z) e^{jk_V z} dz$ [*Cloude*, 2006]. The Fourier transforms $\varphi_m(k_V)$ of the Legendre polynomials have the following closed recursive form:

[5] Notice that $B(z)$, $\beta(z)$ in equation (1.23), and $P(z)$ in (1.28) are three different quantities. $B(z)$ is a power spectral density in height, therefore real-valued and positive by definition. $\beta(z)$ is a complex reflectivity, and it is embedded in the complex data. $P(z)$ is a power distribution. Although these three quantities are different, they express the vertical structure. A deep clarification of the relationship between the three of them is still an open issue in the Tomo-SAR community, and it is out of the scope of this report.

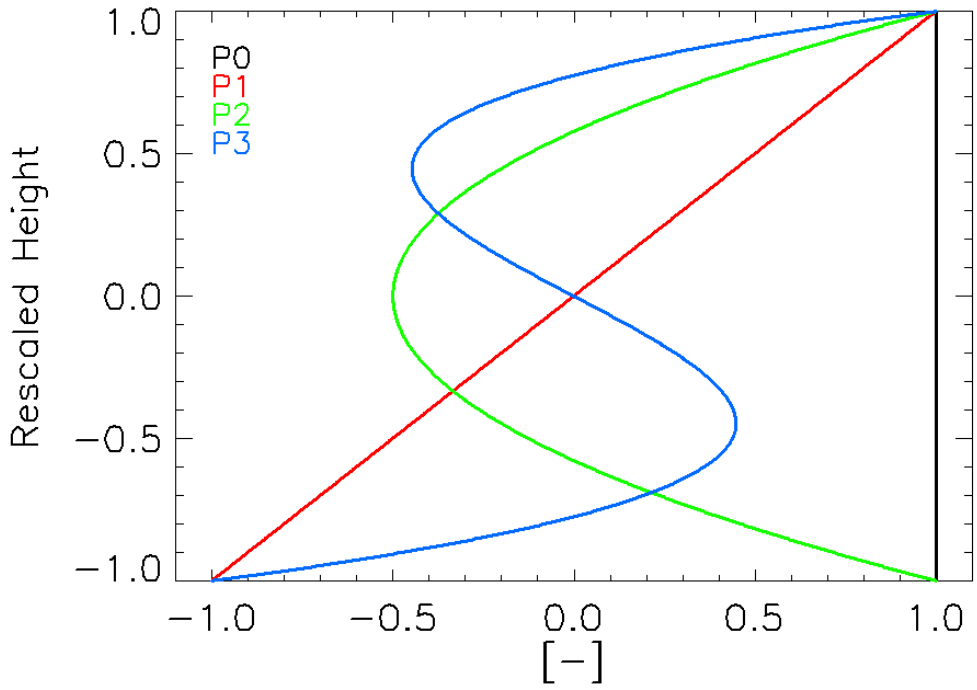

Figure 2.1 – First four Legendre polynomials.

$$\begin{aligned}
&\varphi_0(k_V) = 2\frac{\sin(k_V)}{k_V},\\
&\varphi_1(k_V) = 2j\left(\frac{\sin(k_V)}{k_V^2} - \frac{\cos(k_V)}{k_V}\right),\\
&\vdots\\
&\varphi_m(k_V) = \frac{2m-1}{jk_V}\varphi_{m-1}(k_V) + \varphi_{m-2}(k_V).
\end{aligned} \tag{2.16}$$

From (2.16), it can be noticed that the even-index functions are real while the odd-index functions are pure imaginary.

As mentioned earlier, CT processing uses a finite number of interferometric coherences to reconstruct the vertical structure of forests by estimating a finite set of $M+1$ expansion coefficients. Considering K non-zero baselines from all the available acquisitions, the coherences $\gamma(k_{z,k})$ are collected in the K-dimensional column vector $\boldsymbol{\gamma}$. The CT inversion is performed by means of a least square (LS) fitting between the available coherences and the reconstructed ones. Hence, defining the coefficient vector $\mathbf{c}$, whose elements are $[\mathbf{c}]_m = c_m$, with $m = 0,...,M$, and fixing $c_0 = 1$, the CT inversion can be formulated as:

$$\hat{\mathbf{c}} = \arg\min_{\mathbf{c}} J\,, \tag{2.17}$$

where $J = \|\boldsymbol{\gamma} - \boldsymbol{\gamma}_L\|^2$ and the vector $\boldsymbol{\gamma}_L$ contains the Legendre-reconstructed coherences [*Pardini,* 2011]. To resolve this minimization problem, a matrix approach can been used. For each baseline, or equivalently for each k-th coherence, the following $M \times 2$ matrix can be defined:

$$\mathbf{F}_k = \begin{bmatrix} \varphi_1\left(k_{V,k}\right) & 0 & \varphi_3\left(k_{V,k}\right) & \cdots \\ 0 & \varphi_2\left(k_{V,k}\right) & 0 & \cdots \end{bmatrix}, \tag{2.18}$$

together with a 2-dimensional vector:

$$\mathbf{b}_k = \begin{bmatrix} \Im\{\tilde{\gamma}_k\} \\ \Re\{\tilde{\gamma}_k\} - f_0\left(k_{z,k}\right) \end{bmatrix}, \tag{2.19}$$

where:

$$\tilde{\gamma}_k = \gamma_k e^{-jk_{V,k}} e^{-jk_{z,k}z_0}. \tag{2.20}$$

Finally, by defining a matrix $\mathbf{F}$ and a vector $\mathbf{b}$ as:

$$\mathbf{F} = \begin{bmatrix} \mathbf{F}_1 \\ \vdots \\ \mathbf{F}_K \end{bmatrix}, \ \mathbf{b} = \begin{bmatrix} \mathbf{b}_1 \\ \vdots \\ \mathbf{b}_K \end{bmatrix}, \tag{2.21}$$

the functional (2.17) becomes:

$$J = \left\| \mathbf{F}\mathbf{a} - \mathbf{b} \right\|^2, \tag{2.22}$$

and the minimization problem can be resolved in a closed form as follows:

$$\hat{\mathbf{c}} = \left(\mathbf{F}^T\mathbf{F}\right)^{-1}\mathbf{F}^T\mathbf{b}. \tag{2.23}$$

With these estimated coefficients, the profile reconstruction problem becomes a simple weighted sum of Legendre polynomials as:

$$\hat{B}(z) = \sum_{M=0}^{M} \hat{c}_m f_m(z). \tag{2.24}$$

- This page intentionally left blank -

CHAPTER 3

CT PERFORMANCE ANALYSIS

A performance analysis of the CT inversion with simulated data is presented in this chapter. This analysis is useful to characterize the inversion accuracy and CT potentials for tandem-like missions. On the other hand, the results reported here can be used to understand better the results obtained with real data in the next chapter. For these simulations, acquisition parameters typical of the airborne DLR's E-SAR platform have been used: a radar carrier frequency 1.3 GHz (L-Band), a look angle θ varying form 25° to 50°, an SNR=15dB and a horizontal baseline set [0, 5, 10, 15, 25]m.

In this analysis, different sets of simulation have been carried out, and they can be divided mainly into three sections:

- *Variation of the baseline distribution (Section 3.2)*
  In this section, the performances achievable from different geometric acquisitions, and consequently from different k_z, are analyzed, keeping as reference typical E-SAR parameters and fixing the incidence angle $\theta = 30°$ (near range) and $SNR \to \infty$. In the next step, with reference to the usual E-SAR baseline set [0, 5, 10, 15, 25]m, the performance achievable varying the total height H_V, the incidence angle θ and the ground contribution are presented. Finally, the performance reached with different dual-baseline datasets by fixing the maximum baseline to 25m and varying the smaller baseline is reported.
- *Variation of SNR and sensitivity to different ground contributions (Section 3.3)*
  In this section, the performances achievable varying the *SNR* and the contribution of the ground are analyzed using only two baseline sets, the reference one [0, 5, 10, 15, 25]m and a dual-baseline one [0, 10, 25]m .
- *Analysis of the CT sensitivity to different polarizations (Section 3.4)*

This last section presents the differences between the CT reconstructed profiles using HH-channel and HV-channel, simulating the two polarizations and using both the baseline sets of the previous section.

To create realistic simulated profiles, different LIDAR measurements, acquired in the same area of the available real data, are considered. LIDAR is an optic remote sensing technique using Laser pulses that can also provide vertical profiles of the scenery. Furthermore, for these simulations, a sum of Gaussian-shaped functions is used to create the modeled profiles $B(z)$, allowing a closed-form expression for the associated coherences. Considering a volume profile with a depth H_V, the expression of the coherence for a particular k_z using one Gaussian profile is:

$$\gamma_V\left(H_V,\delta,\chi\right)=\frac{\int_0^{H_V} e^{-\frac{(z-\delta)^2}{2\chi^2}+jk_z z}dz}{\int_0^{H_V} e^{-\frac{(z-\delta)^2}{2\chi^2}}dz}, \tag{3.1}$$

where δ represents the scattering mean height and χ the corresponding standard deviation. Integral (3.1) can be solved in closed form [*Garestier*, 2010] , and it results:

$$\gamma_V\left(H,\delta,\chi\right)=e^{-\frac{\chi^2k_z^2}{2}+j\delta k_z}\frac{erf\left(\frac{1}{\sqrt{2}}\left(j\chi k_z+\frac{\delta}{\chi}\right)\right)-erf\left(\frac{1}{\sqrt{2}}\left(j\chi k_z+\frac{\delta-H_V}{\chi}\right)\right)}{erf\left(\frac{H-\delta}{\sqrt{2}\chi}\right)+erf\left(\frac{\delta}{\sqrt{2}\chi}\right)}. \tag{3.2}$$

At L-band, a realistic scattering model has to consider both the vegetation and ground components. One of the most used models for forest scenarios in this band is the Random Volume over Ground (RVoG) model [*Papthanassiou,* 2001], in which the vegetation layer is modeled as a layer of thickness H_V containing a volume with randomly oriented particles, and the ground is a perfect surface scatterer located at height z_0. In general, scattering mechanisms different from the pure surface may happen at the ground level. For this reason, the ground profile may be different from a Dirac-δ. This has been accounted for in the simulations, and the ground scattering profile has been modeled with a Gaussian function as well. The total coherence can be written:

$$\gamma(\boldsymbol{\omega})=\frac{\mu(\boldsymbol{\omega})\gamma_G+\gamma_V}{1+\mu(\boldsymbol{\omega})}e^{jk_z z_0}, \tag{3.3}$$

where γ_G and γ_V are, respectively, the ground and volume interferometric coherences depending on the vertical profiles of the two layers, $\boldsymbol{\omega}$ is an unitary complex vector defining the choice of the polarization channel (see Section 1.3), and $\mu(\boldsymbol{\omega})$ is the ground-to-volume power ratio associated to $\boldsymbol{\omega}$.

For the performance analysis, three different profiles for the volume have been created with a total height of 30m. Profile no. 1 approximates a scenario with a dense canopy and consequently high extinction, and it is plotted in Fig. 3.1. Profile no. 2 approximates scenarios with a sparse canopy from the top to the

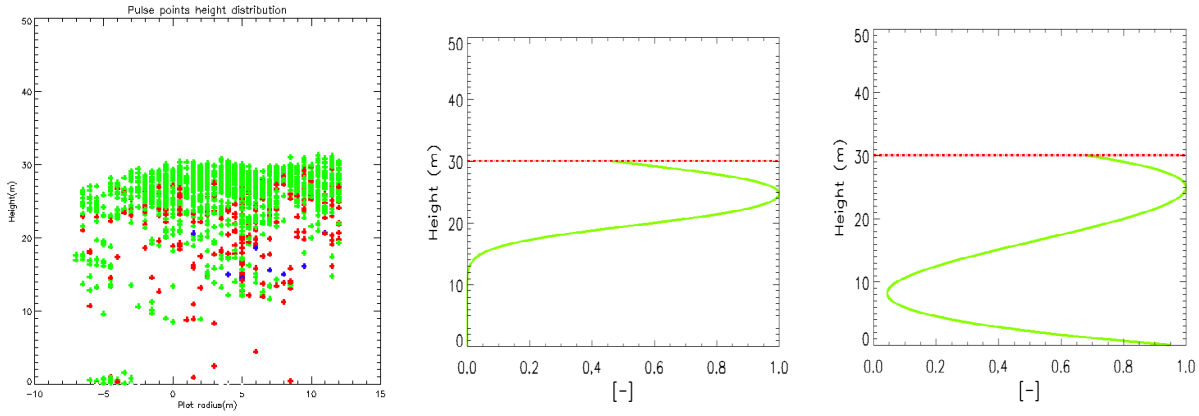

Figure 3.1 – Volume profile no. 1: LIDAR returns (left), model (mid), and CT profile with 4 coefficients (right).

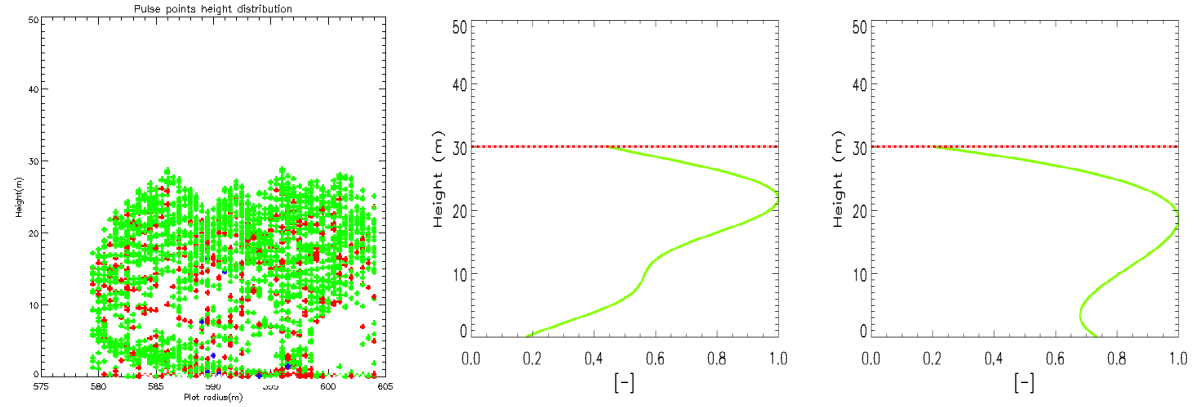

Figure 3.2 – Volume profile no. 2: LIDAR returns (left), model (mid), and CT profile with 4 coefficients (right).

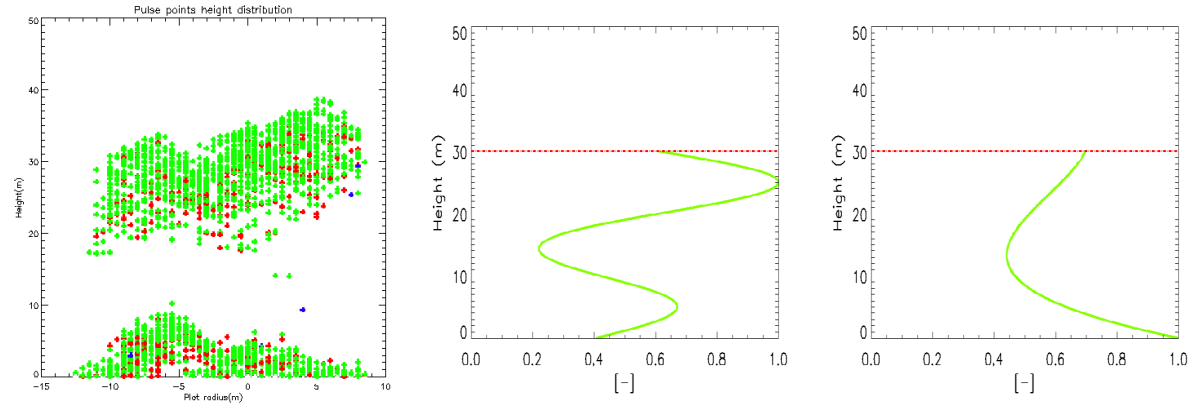

Figure 3.3 – Volume profile no. 3: LIDAR returns (left), model (mid), and CT profile with 4 coefficients (right).

ground level (Fig. 3.2). Finally, profile no. 3 approximates scenarios with a dense canopy on the top, but with an important scattering contribution also at low heights simulating the presence of understory vegetation (Fig. 3.3). Furthermore, a ground profile is created using only one Gaussian-shaped function, with mean value in correspondence of 0m and 1m of standard deviation. In this way, the ground is not considered a perfect surface scatterer.

3.1 Performance measures

In order to measure the profile reconstruction accuracy, we chose as main performance measure the relative power of the reconstruction error between the reconstructed profile and the reference one. In formulas, this error power can be written as:

$$\xi = \frac{\int_0^{H_V} \left[\hat{B}(z) - B_{ref}(z) \right]^2 dz}{\int_0^{H_V} \left[B_{ref}(z) \right]^2 dz} \times 100, \tag{3.4}$$

where $B_{ref}(z)$ is the reference profile.

Furthermore, the identification of the height zones where the profiles vary more and where less can be useful. For this reason, the calculation of the error power (3.4) can also be restricted to smaller height zones inside the volume. In the frame of this work we considered three zones. The first zone, from 0m to 1m, includes the ground contribution. The second zone, from 1m to 16m, corresponds to the central part of the structure, in which the volume scattering components at low height are present (e.g. understory). The third zone, from 16m to 30m, includes the main contribution of the canopy.

For all of these analyses, four coefficients are used. The reason behind this choice is that, with only four coefficients, the necessary baselines for the inversion are two. The use of a small number of baselines reduces temporal effects, especially if spaceborne acquisitions, with long revisit times, are considered. Using four coefficients, CT aims to estimate only the low frequency components of the profiles, where biomass information is more likely to be contained [*Toraño*, 2010]. Indications about this assumption have been obtained in previous investigations.

3.2 Analysis of different baselines sets

The first set of analysis aims to understand how the CT reconstruction varies with different baseline sets and if these variations depend on particular vertical profiles. In this section, the simulated data are created considering only volume contribution modeled according to profiles no. 1-3. For these analyses, the Legendre decompositions of the real profiles are used as reference, representing the best reconstruction of a CT vertical profile, being equivalent to a CT inversion with an infinite number of baselines. Ground and volume heights are supposed perfectly known. To improve the readability of the experiment descriptions, the figures are reported in the end of this Section.

In the first simulation, the total baseline varies from 10m to 100m and the spacing is fixed to 5m, varying in this way also the number of baselines. The tomographic resolution improves from 28m to 2,8m, whereas the height ambiguity remains fixed to 56,3m. The total difference between Legendre profiles and CT profiles with $SNR \to \infty$ are plotted in Fig. 3.4, as a function of the total baseline. With a total baseline of 10m, the reconstruction error power can reach the 45%, and it varies significantly with the profile used. Notice that in this case, only 2 baselines and a low tomographic resolution of 28m are available for processing. Increasing the maximum baseline (and consequently the maximum baseline), an improvement on the performance can be immediately seen. For a total baseline of 25m and 5 baselines, the total difference is

less than 10% and the differences among different profiles are not significant. Furthermore, after 25m, a sensitive improvement of this performance cannot be observed. In conclusion, a set of 5 baselines with a total baseline of 25m is enough to obtain a satisfactory reconstruction (error power lower than 10%) for profiles with $H_V = 30\,\text{m}$ and using $M = 4$ coefficients.

Still using only volume profiles, the second analysis presented in this section is made by varying the spacing between the baselines and by maintaining a maximum baseline of 25m. The baseline spacing ranges from 1m to 12.5m, and in this way the number of baselines varies from 25 to 2. Accordingly, the tomographic resolution is fixed to 11,6m, whereas the height ambiguity varies from 281m to 22,5m. The total reconstruction errors between the CT estimated profiles with $SNR \to \infty$ and the reference Legendre profiles are shown in Fig. 3.5 for the three assumed profiles. Starting with 1m spacing (25 baselines), the reconstruction error is lower than 5%. Moreover, the three profiles exhibit comparable errors, showing that with this acquisition geometry a suitable CT inversion is achievable almost independently of the real profile. Considering now a spacing of 5m (5 baselines), typical of DLR E-SAR data sets, approximately the same results can be observed. With larger spacings, the reconstruction error increases and it is profile dependent. In the extreme case of a spacing of 12,5m (only 2 baselines), between profile no. 2 and no. 3 there is an error difference of 60%. This is a first indication that a dual-baseline inversion is to be considered carefully.

From here on, taking into account the results of the two previous analyses, a maximum baseline of 25m and a spacing of 5m are considered if not otherwise specified, since this spatial sampling (beyond reflecting a typical real situation) leads to well-performing inversions, at least for a volume height of 30m. It is therefore of interest to evaluate the performance of CT by varying the total height H_V of the profiles from 10m to 70m, again using volume-only profiles. Two different incidence angles are used for these simulations, $\theta = 30°$ and $\theta = 43°$, representing usual near range and far range acquisitions, respectively. The power of the reconstruction errors between Legendre profiles and CT estimated profiles as a function of the total height H_V are plotted in Fig. 3.6 for the three profiles. To judge the inversion performance, we assume that a maximum error power equal to 20% can be accepted. Considering the results in near range (top panel), problems in the estimation of the profile are visible for H_V from 10m to 17m because the resolution of 11,6m is comparable with the profile height. Then, from 17m to around 56m, good performances are achievable for the three profiles. Notice that the increase of resolution acts differently for each profile. It is apparent how after $H_V = 56\text{m}$ the height ambiguity caused by this acquisition geometry affects the CT performances. Considering now the results in far range (bottom panel), problems of resolution are visible for H_V from 10 to around 30m, because with this acquisition geometry the resolution is worse than before. Problems of ambiguity are not visible in far range because the ambiguity interval is now larger than 70m.

The last analysis as a function of the acquisition geometry considers again volume-only profiles and it has been carried out by varying the incidence angle from 25° to 50°, with $H_V = 30\text{m}$. The powers of the reconstruction error between Legendre profiles and CT estimated profiles are reported in Fig. 3.7 for the three different structures. In this plot, a vertical green line is drawn in correspondence of the acquisition

geometry with a resolution of 20m, which corresponds to $\theta = 42°$. For incidence angles lower than 42° a good profile estimation is achievable (height resolution is high enough), whereas for incidence angles greater than 42° problems due to low resolution are observable.

For the next analyses, a ground contribution is added to each of the three profiles. The ground vertical structure is modeled as explained in the Chapter introduction. Analyzing the performances of the CT inversion by varying the ground-to-volume power ratio μ is now of interest. Only two baseline sets are used, the typical DLR E-SAR campaign set (5 baselines, with maximum baseline of 25m), and a 20-baseline set with a maximum baseline of 100m. With these two sets, the ambiguity is fixed to 56.3m, whereas the tomographic height resolution amounts to 11.6m for the first set and 2.8m for the second set. Starting from the volume profile no. 1, the power of the reconstruction error between the Legendre profiles (including volume and ground) and the CT estimated profiles with $SNR \to \infty$ as a function of μ is shown in Fig. 3.8. Small error powers (lower than 10%) can be observed for both datasets. However, it is worth noting that the error power slowly increases at the increase of μ for the acquisition with 25m maximum baseline. Instead, with the increase of the height resolution obtained with a total baseline of 100m, a better estimation of the profiles can be achieved for higher μ. The homologous plots obtained with profile no. 2 and profile no. 3 (Fig. 3.9 and Fig. 3.10 respectively) report the same trend and almost the same accuracies. This is another indication that a larger total baseline with the same density of sampling does not produce a considerable improvement on the CT inversion, even with $\mu = 10\,\text{dB}$ (at least with $M = 4$ and $H_V = 30\,\text{m}$).

It is also important checking if non-uniformly spaced baseline (most frequently found in practical applications) can lead to the same reconstruction performance as obtained until now. Therefore the reconstruction error of the CT profiles obtained with the baseline set [0, 5, 10, 15, 25]m with respect to the ones obtained with uniform distribution [0, 5, 10, 15, 20, 25]m have been evaluated as a function of μ. The obtained results are plotted in Fig. 3.11 for the three volume profiles. Almost no differences in the error power can be appreciated, and its maximum achieves the 2.5%. Thus, it is possible to conclude that the thinning of the typical E-SAR baseline distribution do not causes particular inversion problems.

Since the CT inversion with four coefficients needs at least two baselines for algebraic reasons, it is of interest to analyze which is the achievable performance in the extreme case in which only dual-baseline data are available for processing. In the following experiments, the maximum baseline has been kept equal to 25m. The plot in Fig. 3.12, referred to profile no. 1, shows the power of the reconstruction error between CT and Legendre profiles by varying the length of the shorter baseline. Two different μ are considered, i.e. $\mu = -3\,\text{db}$ and $\mu = 3\,\text{db}$. The best results are obtained for the smaller baseline ranging from 5m to 10m, whereas around 16m there is an unstable behavior of the inversion. In terms of the typical E-SAR baselines, the set [5, 10, 15]m produces better results, with low error power and negligible differences between the two chosen values of μ. The results of profile no. 2, shown in Fig. 3.13, confirm the trend of the error power observed for the profile no. 1. To get more insights about this trend, the plot obtained with profile no. 3 is shown in Fig. 3.14, together with the condition number of the matrix $\mathbf{F}\mathbf{F}^H$, the one that is inverted in

equation (2.23). Furthermore, the MB point-spread function[6] (PSF) of the system with each baseline set is shown in the bottom panel of the same figure. In this panel, two white horizontal lines have been drawn to delimit the height interval of interest between 0m (position of the scatterer) and 30m (volume height). A white dot indicates the half of the ambiguity height interval for a uniform dual-baselines dataset. From the PSF plot, an apparent problem of ambiguity can be noticed into the 0-30m height interval for smaller baseline ranging from 0m to 4m, from 11m to 14m and from 21m to 25m. Consistently, CT profiles estimated by these acquisition geometries produce high values of the reconstruction errors. Furthermore, problems in the CT inversion are also visible for smaller baselines around 16m. This phenomenon has been explained with the poor conditioning of the inversion (mid panel).

In Fig. 3.15 the same plots of Fig. 3.14 are reported considering two different profiles (solid and dotted lines) and three different H_V (different colors) for each profile, in the same acquisition geometry. In the top panel, the power of error between the CT profiles estimated with the dual-baseline and the CT profiles estimated with a full 5-baseline configuration (25m maximum baseline) is plotted. Starting from $H_V = 10\,\mathrm{m}$, the error powers are are very low for most of the smaller baselines and for both the simulated profiles. For $H_V = 20\,\mathrm{m}$, different vegetation structures give different error powers, but in general reconstruction problems arise with the small baseline shorter than 8m or longer than 20m. From the other panels, it is reasonable to affirm that this low reconstruction accuracy can be mainly attributed to height ambiguities. Indeed, a bad PSF increases its negative effects on the profiles with the increase of their total height. No particular problems of ill conditioning of the inversion are observable. Finally, for $H_V = 30\,\mathrm{m}$, a higher sensitivity of the dual-baseline reconstruction to both the vegetation structure and the particular baseline set is apparent. High error powers due to ambiguity problems are still visible in the same positions as for $H_V = 20\,\mathrm{m}$. Problems of conditioning are visible for small baselines around 15m.

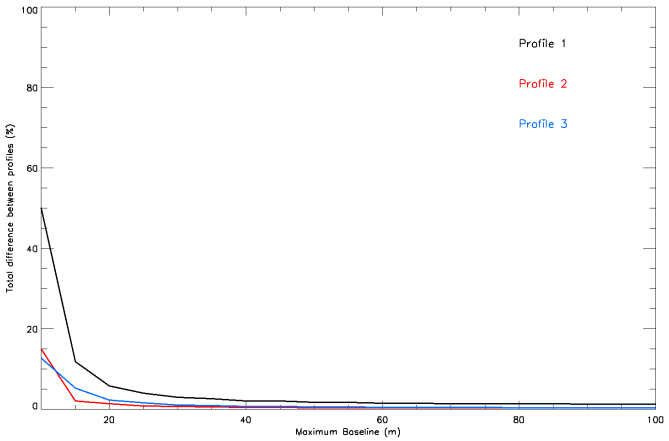

Figure 3.4 – Reconstruction error power (CT estimated vs Legendre) as a function of the maximum baseline, with a fixed height ambiguity interval (i.e. varying number of baselines with the same spacing).

[6] The tomographic PSF is the BF spectrum obtained for a point-like scatterer. It is therefore a function of the steering vector only.

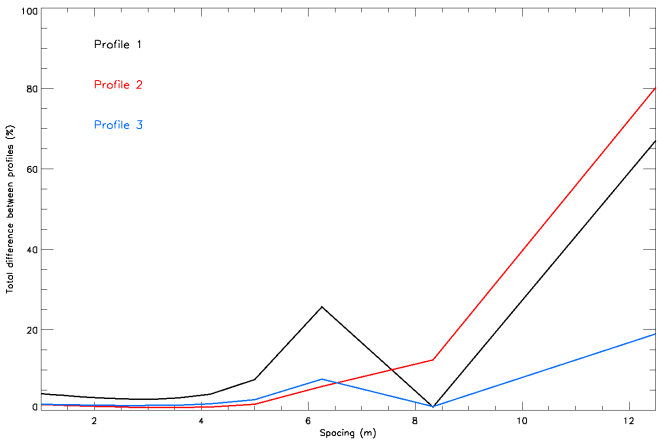

Figure 3.5 – Reconstruction error power (CT estimated vs Legendre) as a function of the spacing between the baselines, fixed a maximum baseline of 25m. The number of baselines varies accordingly.

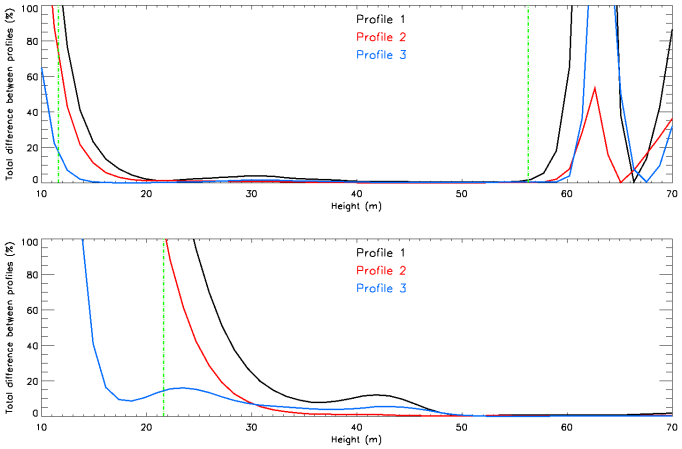

Figure 3.6 – Reconstruction error power (CT estimated vs Legendre) with θ=30° (top panel) and θ=43° (bottom panel) as a function of the total height of the profiles. In the top panel, the green line on the left side indicates the height resolution whereas the one on the right one indicates the height of ambiguity. In the bottom panel, the green line indicates the height resolution. Horizontal baselines (airborne E-SAR configuration): [5, 10, 15, 20, 25].

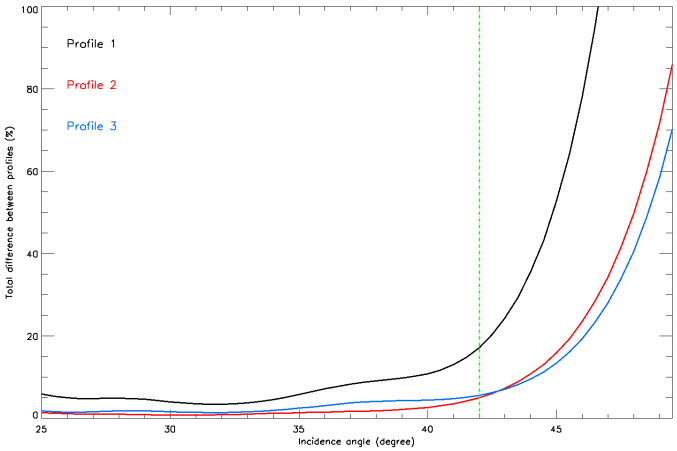

Figure 3.7 – Reconstruction error power (CT estimated vs Legendre) as a function of the incidence angle. The green line is in correspondence of the acquisition geometry with a resolution of 20m. Horizontal baselines (airborne E-SAR configuration): [5, 10, 15, 20, 25].

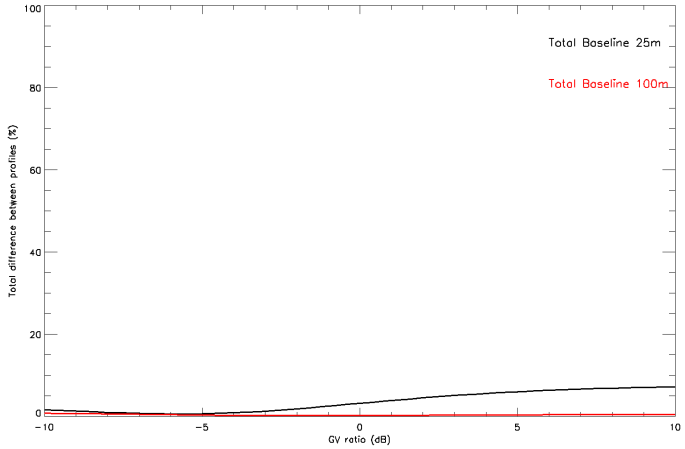

Figure 3.8 – Reconstruction error power (CT estimated vs Legendre) as a function of the ground-to-volume ratio for profile no. 1. Horizontal baselines (airborne E-SAR configuration): uniformly spaced with 5m sampling and maximum baseline indicated in the plot legend.

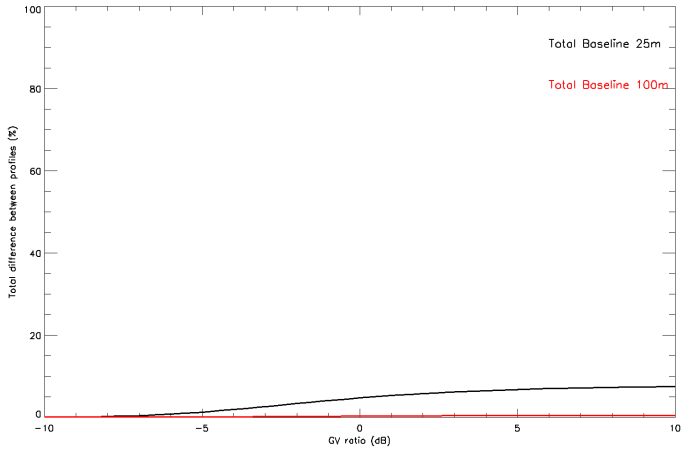

Figure 3.9 – Reconstruction error power (CT estimated vs Legendre) as a function of the ground-to-volume ratio for profile no. 2. Horizontal baselines (airborne E-SAR configuration): uniformly spaced with 5m sampling and maximum baseline indicated in the plot legend.

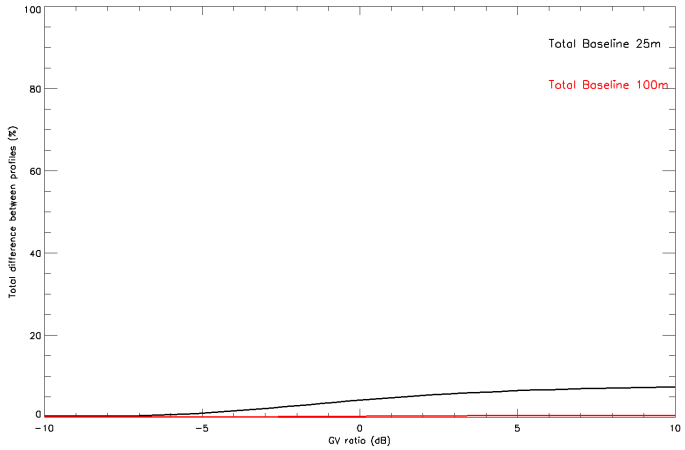

Figure 3.10 – Reconstruction error power (CT estimated vs Legendre) as a function of the ground-to-volume ratio for profile no. 3. Horizontal baselines (airborne E-SAR configuration): uniformly spaced with 5m sampling and maximum baseline indicated in the plot legend.

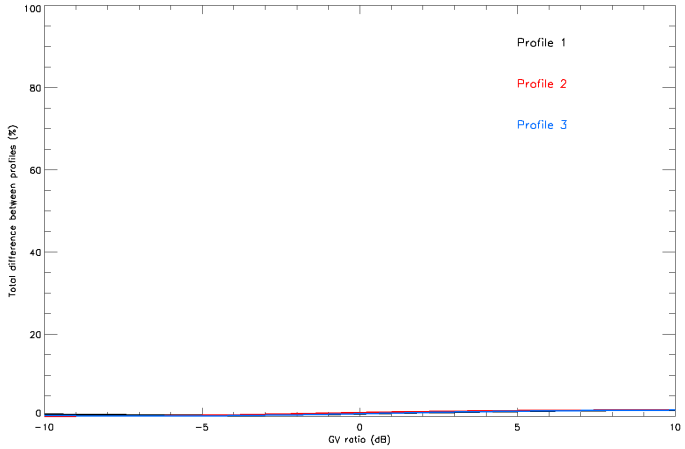

Figure 3.11 – Reconstruction error power (CT estimated, non-unif. vs unif. baselines) as a function of the ground-to-volume ratio for the three profiles. Horizontal baselines (airborne E-SAR configuration): unif. [5, 10, 15, 20, 25], non-unif. [5, 10, 15, 25].

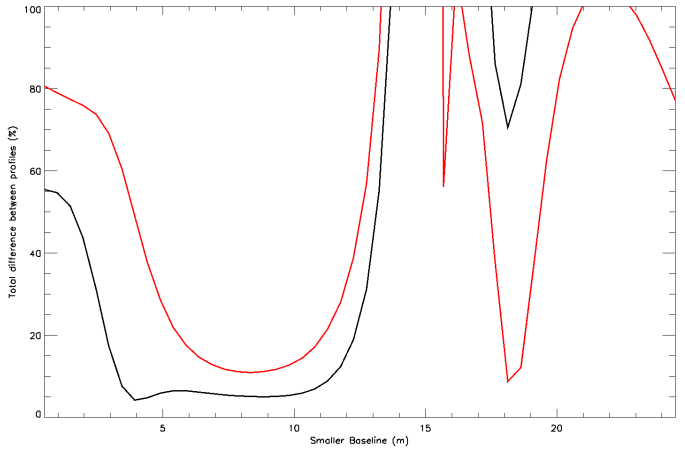

Figure 3.12 – Reconstruction error power (CT estimated vs Legendre) as a function of the small baseline in a dual-baseline set with max. baseline equal to 25m, profile no. 1. Black curve: μ = -3dB; red curve: μ = 3dB.

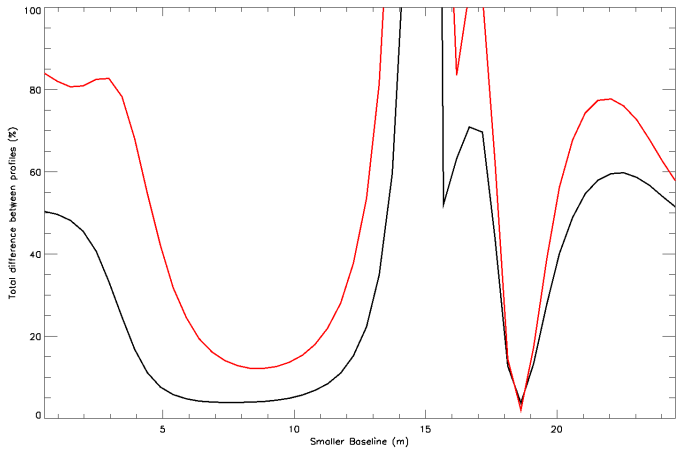

Figure 3.13 – Reconstruction error power (CT estimated vs Legendre) as a function of the small baseline in a dual-baseline set with max. baseline equal to 25m, profile no. 2. Black curve: μ = -3dB; red curve: μ = 3dB.

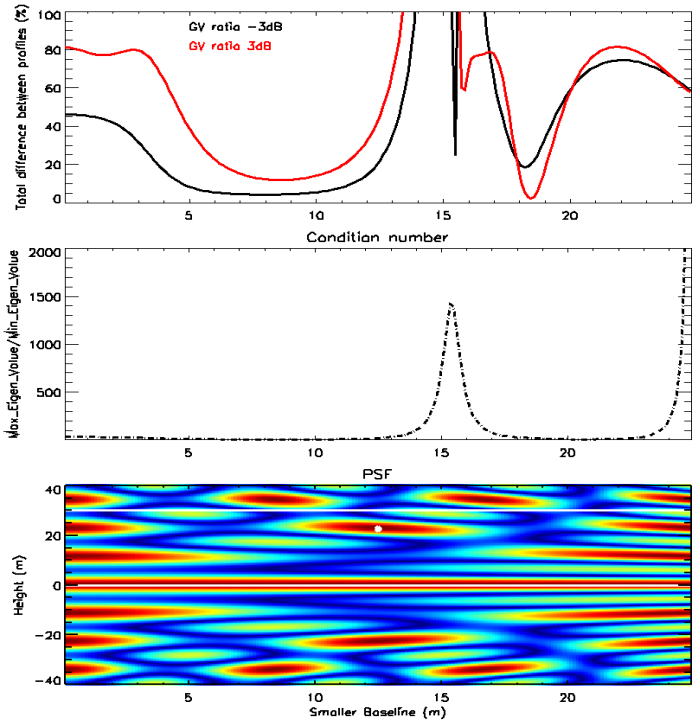

Figure 3.14 – Top panel: reconstruction error power (CT estimated vs Legendre) as a function of the small baseline in a dual-baseline set with max. baseline equal to 25m, profile no. 3. Mid panel: condition number of the inversion. Bottom panel: PSF.

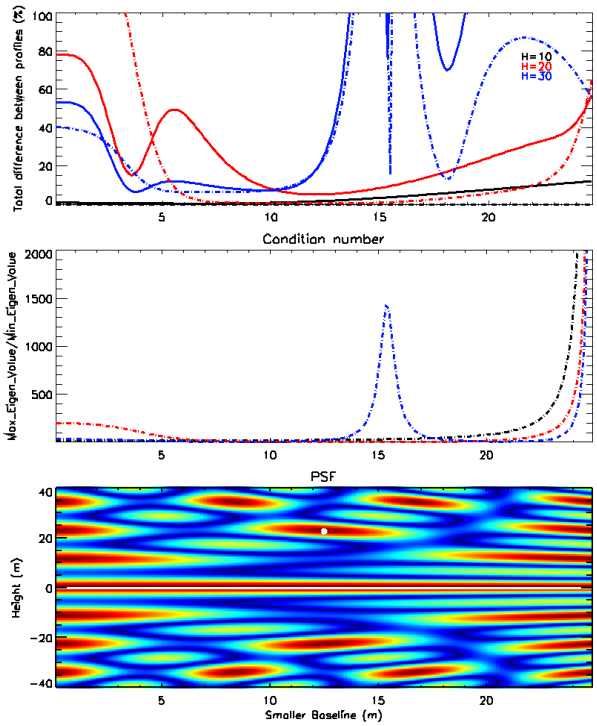

Figure 3.15 – Top panel: reconstruction error power (CT, estimated dual-baseline with max. baseline 25 m vs baselines [5, 10, 15, 20, 25]m) as a function of the small baseline of the dual-baseline set, profile no. 1 and no. 2, for different volume heights. Mid panel: condition number of the inversion for profile no. 1. Bottom panel: PSF.

3.3 Analysis of the robustness and sensitivity of CT

In this section, using the two baseline sets selected in Section 3.2, the robustness of the CT inversion is analyzed against the presence of additive noise and in the retrieval of the volume only contribution when also ground scattering is present. A comparison will also be carried out with the ABF estimator. For the sake of simplicity, from here on, the baseline distributions [5, 10, 15, 20, 25]m and [10, 15]m will be called "full-baseline set" and "dual-baseline set", respectively.

To understand the robustness against noise, Monte Carlo simulations have been used. For each Monte Carlo run, 100 independent looks of Gaussian distributed MB complex-valued data are generated imposing an MB coherence equal to the one corresponding to the selected profile. To evaluate the reconstruction performance, *P* realizations have been used. For each *p*-th realization, the reconstruction error power ξ_p is evaluated according to equation (3.4). Afterwards, the global performance is measured by means of the RMS of ξ:

$$\mathrm{RMS}(\xi) = \sqrt{\frac{1}{P}\sum_{p=1}^{P}\xi_P^2}\,, \tag{3.5}$$

where P is the total number of the realizations . For this analysis, we considered $P = 1000$.

The first analysis presented in this section has been made varying the *SNR*. The plots in Fig. 3.16 show $\mathrm{RMS}(\xi)$ for both the full- and the dual-baseline sets. The error power is calculated between the CT estimated profiles and the CT profiles estimated in absence of noise. In general, $\mathrm{RMS}(\xi)$ shows the most of the variation between $SNR = 0\mathrm{dB}$ and $SNR = 10\mathrm{dB}$, and it decreases at the increase of *SNR*. For $SNR > 10\mathrm{dB}$, $\mathrm{RMS}(\xi)$ does not decrease anymore. The reached limit value depends on the profiles and the baseline configuration, and it is approximately equal to 5% for the full-baseline set and 10% for the dual-baseline set for profiles no. 2 and no. 3, while it is halved for profile no. 1. It has been observed that if the number of independent looks grows up to 1000, these "asymptotic" values decrease to around 0%. It is of interest to investigate also the *SNR* sensitivity of the ABF estimator. For this purpose, Fig. 3.17 show $\mathrm{RMS}(\xi)$ of ABF obtained in the same conditions of Fig. 3.16, compared to the ABF profiles estimated in absence of noise. From these simulations, it results that ABF is less sensitive to the *SNR* than CT. Nevertheless, the difference of $\mathrm{RMS}(\xi)$ between the two estimators is negligible for the applications, especially for the full-baseline set.

To understand if 100 looks are satisfactory to estimate the coherences, theoretical and estimated coherences have been compared by varying the *SNR*. In Fig. 3.18, this comparison is shown for profile no. 1 and the 5m baseline. Considering $SNR = 15\mathrm{dB}$ (a value typically observed in spaceborne SAR data), it is apparent that 100 independent looks are enough for a very accurate estimation of the coherence. However, it is worth remembering that a very good estimate of the coherence does not necessarily imply a very accurate CT inversion, as previously analyzed in the case of infinite *SNR*. In the following analysis, we set 100 independent looks and $SNR = 15\mathrm{dB}$.

The second set of simulations reported in this section aims to investigate how close is the reconstructed CT profile to the volume-only Legendre profile in the case in which the data contain also ground scattering. For this reason, $\mathrm{RMS}(\xi)$ has been now evaluated between the reconstructed CT profiles and the volume only Legendre profiles, using both baseline sets. The obtained $\mathrm{RMS}(\xi)$ as a function of the ground-to-volume ratio μ are plotted in Fig. 3.19, 3.20 and 3.21, corresponding respectively to profile no. 1, no. 2 and no. 3, together with the fractions of $\mathrm{RMS}(\xi)$ for three height intervals between 0 and $H_V = 30\mathrm{m}$. It is apparent that the CT profiles with ground are very different from the volume profiles. Even considering $\mu = -5\mathrm{dB}$, the $\mathrm{RMS}(\xi)$ is around 20% for the full-baseline set and around 50% for the dual-baseline set. Fixing $\mu = 10\mathrm{dB}$, $\mathrm{RMS}(\xi)$ equals 230% and 370% for profile no. 1 and profile #2, respectively, for the full-baseline set. Higher values are obtained with the dual-baseline set. Focusing on the relative differences inside the three zones of the profile, it is visible how the brown zone, corresponding to the ground contribution (between 0m and 1m height), produces the 20-40% of the total $\mathrm{RMS}(\xi)$. Furthermore, each volume profile performs differently. Hence, it is possible to conclude that if the interest is in the reconstruction of the volume-only profiles, the ground scattering needs to be cancelled. The same analysis has been carried out also for the ABF estimator, and the results are shown in Figs. 3.22, 3.23 and 3.24. It can be observed that ABF is less sensitive to the ground contribution, independently of the specific volume profile, and that the dual-baseline set produces lower values of total difference than the full dataset, unlike with the CT inversion. Focusing on the fraction of $\mathrm{RMS}(\xi)$ in each zone, the greatest contribution on the total difference comes from the ground as for the CT, but the increase of μ produces a non-monotonic variation of the $\mathrm{RMS}(\xi)$ fraction for height interval. This phenomenon can be explained by remembering that the ABF estimator outputs a power distribution (not a power spectral density) and that it is based on a filterbank implementation. However, a deeper analysis is required and it is left for future work.

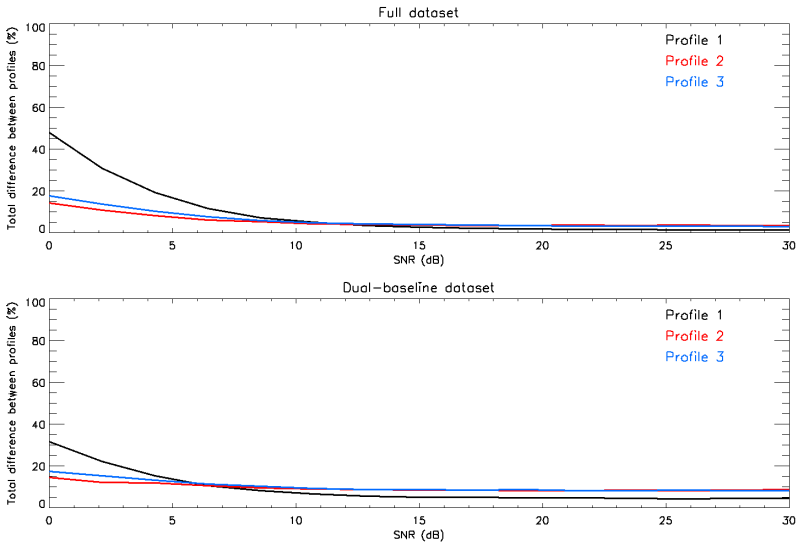

Figure 3.16 – RMS(ξ), CT estimated profiles vs CT profiles estimated in absence of noise, full-baseline set (top panel) and dual-baseline set (bottom panel) as a function of *SNR*.

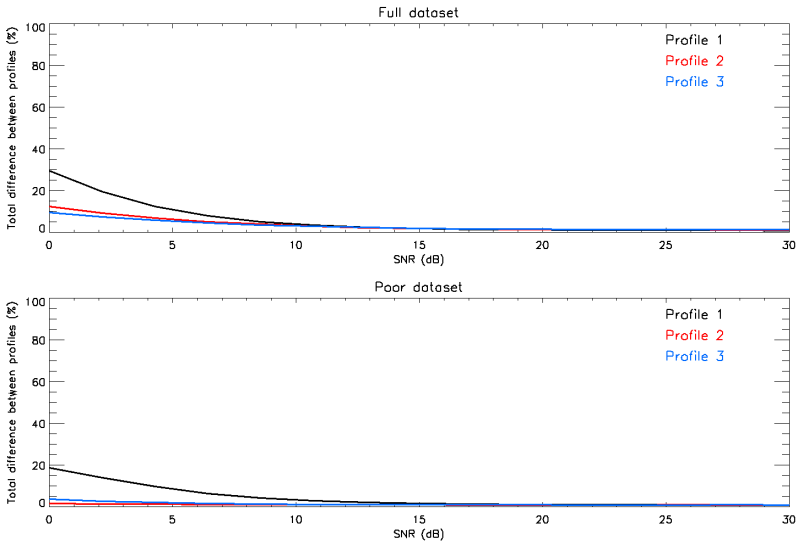

Figure 3.17 – RMS(ξ), ABF estimated profiles vs ABF profiles obtained in absence of noise, full-baseline set (top panel) and dual-baseline set (bottom panel) as a function of *SNR*.

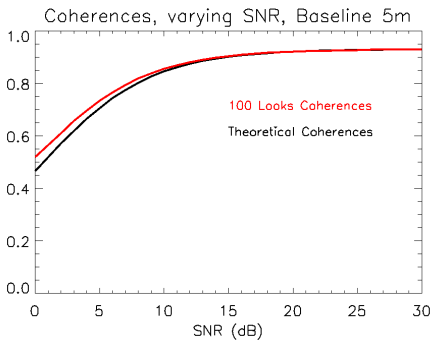

Figure 3.18 – Theoretical coherences (black curve) and coherences (red curve) estimated with 100 independent looks as a function of *SNR*, profile no. 1.

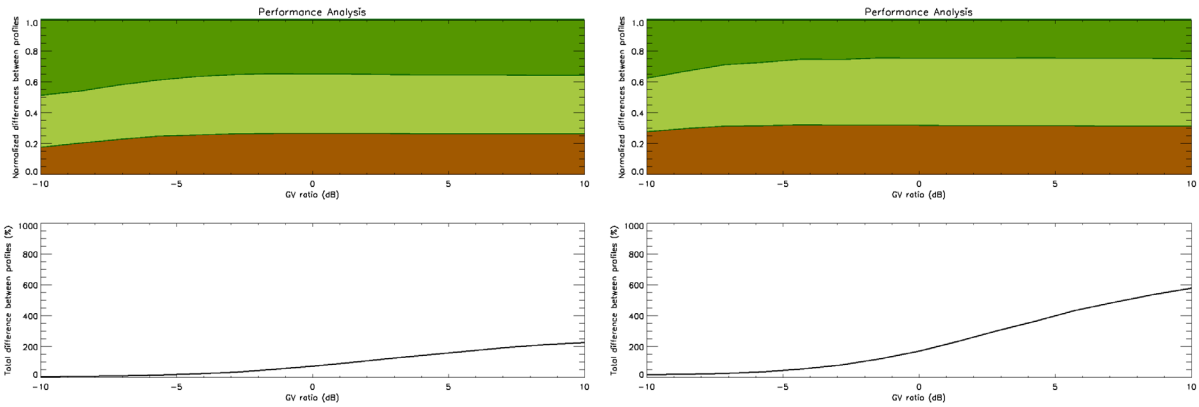

Figure 3.19 – CT estimated profiles vs Legendre profiles as a function of μ, profile no. 1. Top panel: Fractions of RMS(ξ) calculated between 0m and 1m height (brown), between 1m to 16m (light green) and between 16m to 30m (dark green). Bottom panel: total RMS(ξ). Left side: full-baseline set. Right panel: dual-baseline set.

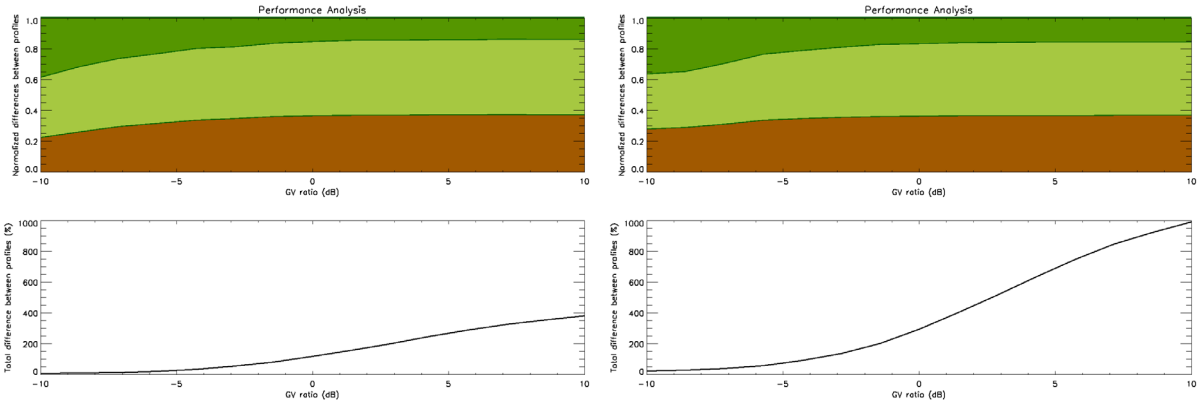

Figure 3.20 – CT estimated profiles vs Legendre profiles as a function of μ, profile no. 2. Top panel: Fractions of RMS(ξ) calculated between 0m and 1m height (brown), between 1m to 16m (light green) and between 16m to 30m (dark green). Bottom panel: total RMS(ξ). Left side: full-baseline set. Right panel: dual-baseline set.

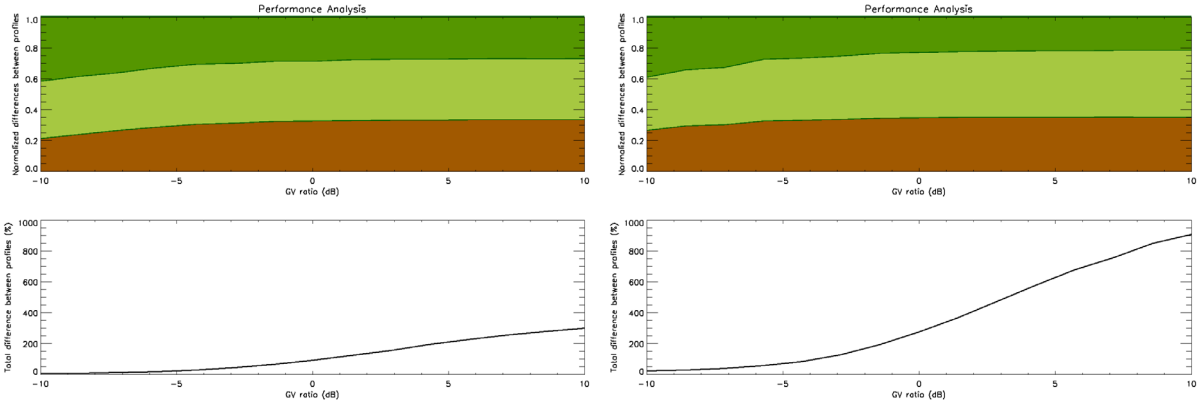

Figure 3.21 – CT estimated profiles vs Legendre profiles as a function of μ, profile no. 3. Top panel: Fractions of RMS(ξ) calculated between 0m and 1m height (brown), between 1m to 16m (light green) and between 16m to 30m (dark green). Bottom panel: total RMS(ξ). Left side: full-baseline set. Right panel: dual-baseline set.

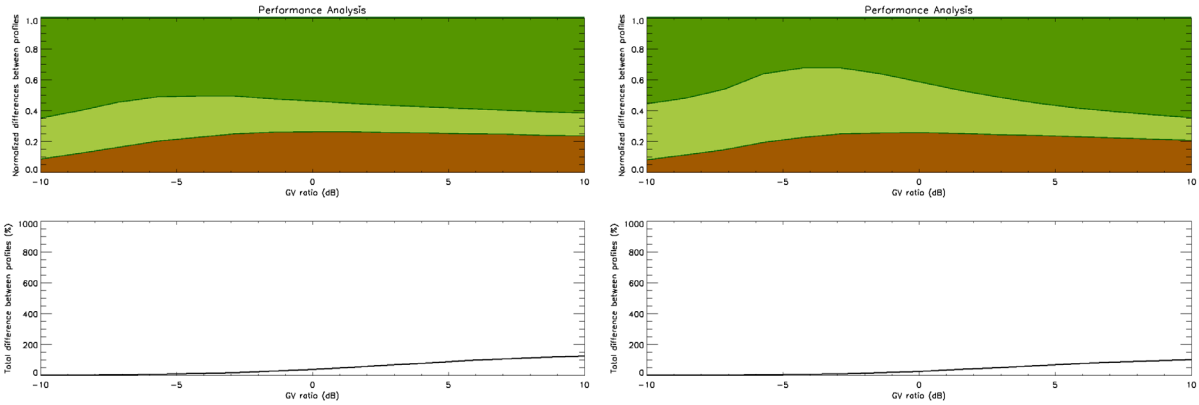

Figure 3.22 – ABF estimated profiles vs theoretical ABF profiles (infinite number of baselines) as a function of μ, profile no. 1. Top panel: Fractions of RMS(ξ) calculated between 0m and 1m height (brown), between 1m to 16m (light green) and between 16m to 30m (dark green). Bottom panel: total RMS(ξ). Left side: full-baseline set. Right panel: dual-baseline set.

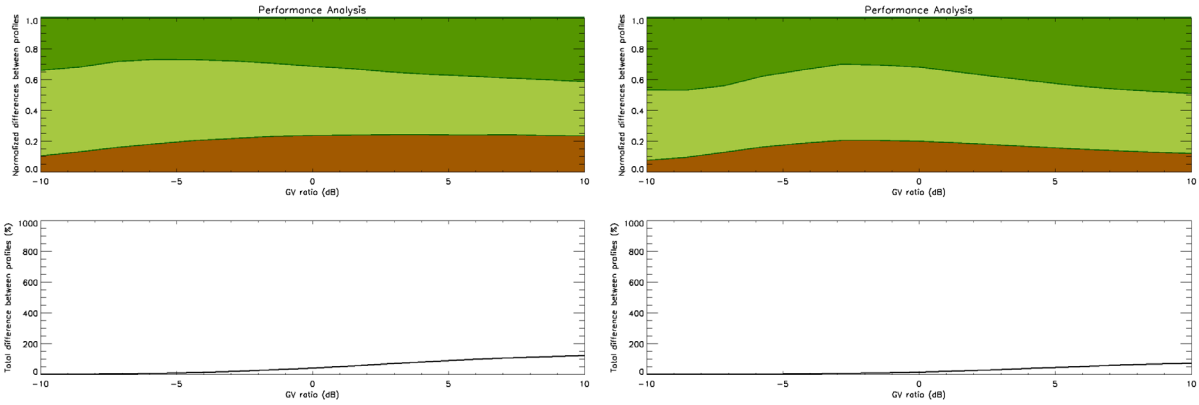

Figure 3.23 – ABF estimated profiles vs theoretical ABF profiles (infinite number of baselines) as a function of μ, profile no. 2. Top panel: Fractions of RMS(ξ) calculated between 0m and 1m height (brown), between 1m to 16m (light green) and between 16m to 30m (dark green). Bottom panel: total RMS(ξ). Left side: full-baseline set. Right panel: dual-baseline set.

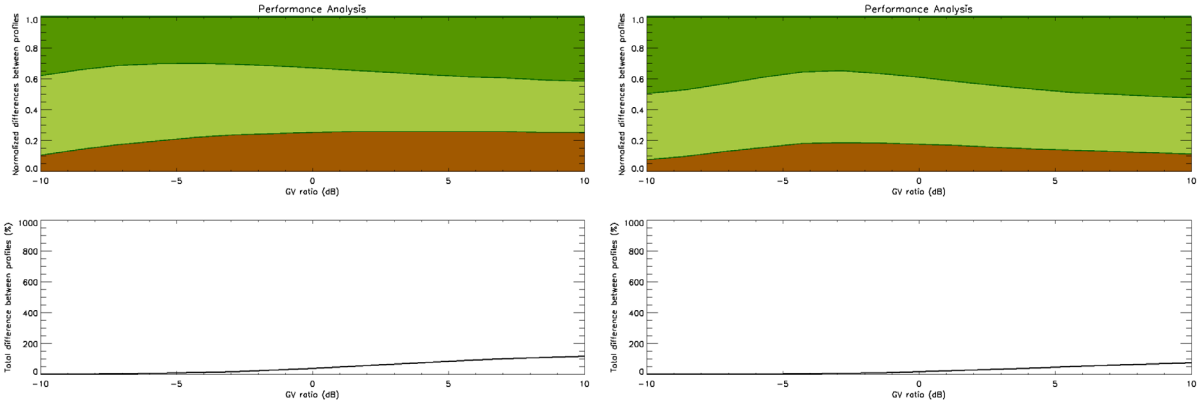

Figure 3.24 – ABF estimated profiles vs theoretical ABF profiles (infinite number of baselines) as a function of μ, profile no. 3. Top panel: Fractions of RMS(ξ) calculated between 0m and 1m height (brown), between 1m to 16m (light green) and between 16m to 30m (dark green). Bottom panel: total RMS(ξ). Left side: full-baseline set. Right panel: dual-baseline set.

3.4 Analysis of the CT sensitivity to different polarizations

In this last analysis, MB acquisitions in the polarization channels HH and HV are simulated using a MB extension of the RVoG model. This polarimetric-interferometric model needs: (1) two K-dimensional vectors containing the MB coherences related to the vertical structure of the volume component ($\boldsymbol{\gamma}_V$) and of the ground component ($\boldsymbol{\gamma}_G$); (2) two polarimetric coherence matrices in the lexicographic basis, one for the volume component ($\mathbf{C}_V$) and one for the ground component ($\mathbf{C}_G$). Defining $\boldsymbol{\Omega}$ as the $(3K \times K)$-dimensional matrix which contains K polarimetric-interferometric (3×3)-dimensional coherence matrices (one for each baseline), it is possible to demonstrate that [*Tebaldini*, 2009]:

$$\boldsymbol{\Omega} = \mathbf{C}_G \otimes \boldsymbol{\gamma}_G + \mathbf{C}_V \otimes \boldsymbol{\gamma}_V , \tag{3.6}$$

where "$\otimes$" denotes the Kronecker product. The coherences for each polarization channel can therefore be extracted from $\boldsymbol{\Omega}$. The volume layer has been assumed random, thus the volume polarimetric covariance matrix can be written as [*Cloude*, 1992]:

$$\mathbf{C}_V = \begin{bmatrix} 1 & 0 & 1/3 \\ 0 & 2/3 & 0 \\ 1/3 & 0 & 1 \end{bmatrix}. \tag{3.7}$$

The ground layer is assumed composed by double bounce scattering (due to interaction between trunks and ground) and direct surface scattering. Considering also the roughness of the ground and of the trunks, the polarimetric coherence matrix can be modeled as [*Freem.*, 1998]:

$$\mathbf{C}_G = \begin{bmatrix} \mu_{HH} & 0 & \delta a_{VV} \\ 0 & \mu_{HH} a_{HV}{}^2 & 0 \\ \delta^* a_{VV} & 0 & \mu_{HH} a_{VV}{}^2 \end{bmatrix} \tag{3.8}$$

where μ_{HH} is the ground-to-volume ratio in HH, δ is a complex number with $|\delta| = 1$, and a_{VV} and a_{HV} are two real parameters.

In forest scenarios, the received signal in HH differs from the one received in HV. The (L-band) signal usually penetrates the (volume) canopy layer and reaches the ground before backscattering. The surface backscattering mechanism is stronger for the co-polarization channels (HH, VV), than for the cross-polarization channel (HV). According to the selected model, this physical behavior results into different ground-to-volume ratios in HH and HV. This difference of μ can be simulated by varying a_{HV}.

In this section, the variations of the CT estimated profiles from one polarization to the other are quantified statistically, considering as a measure of performance $\mathrm{RMS}(\xi)$ in a Monte Carlo analysis with 1000 realizations. As always, the usual three volume profiles are considered to investigate profile dependencies. Fig. 3.25 shows $\mathrm{RMS}(\xi)$ calculated between the CT profiles estimated in HH and HV with $\mu_{HH} = -3\mathrm{dB}$ and by varying a_{HV}^2. From this plot, it is apparent that profiles estimated in different polarization channel are different. Considering for example the full-baseline set and $a_{HV}^2 = 0.25$ (around $-6\mathrm{dB}$), the $\mathrm{RMS}(\xi)$ ranges from 15% to 20% depending on the profile. Considering the dual-baseline set,

the trend is maintained, but the values of total difference are around the double. Hence, the dual-baseline set seems being more sensitive to the change of polarization channel than the full one. The same analysis has been repeated with $\mu_{HH} = 3\text{dB}$, and it is presented in Fig. 3.26. As the ground scatterer is more visible (remember the results in Section 3.3), the increase of the μ_{HH} seems to produce slightly higher sensitivity to different polarizations for both the datasets.

3.5 Conclusions

In conclusion of this chapter, a summary of the performance analysis is reported.

Different baseline sets have been tested. Focusing on airborne acquisitions, it has been observed that an horizontal baseline spacing lower than 5m or a maximum horizontal baseline higher than 25m does not improve significantly the CT inversion with 4 coefficients and for tree heights around 30m[7]. Then, normalized powers of the reconstruction error lower than 5% have been observed between profiles estimated by a 25m uniform array (with a 5m of spacing) and by the typical E-SAR baseline set [0, 5, 10, 15, 25]m. In perspective, we do not expect particular profile inversion inaccuracies with real E-SAR data (see next Chapter). Furthermore, considering a possible dual-baseline implementation with a fixed maximum baseline of 25m and the available baseline from the typical E-SAR baseline set, the best dual-baseline profile reconstruction has been obtained with the baseline set [0, 10, 25]m (*best* dual-baseline configuration) whereas with the baseline set [0, 15, 25]m the inversion is affected by heavy problems of conditioning (*worst* dual-baseline configuration). It is worth remarking that the performance of a dual-baseline reconstruction is heavily affected by the kind of profile to be estimated.

The impact of different *SNR*s on the profile estimation has been measured as well. With typical values of *SNR* around 15dB and by averaging 100 looks the CT inversion has not shown apparent problems on the profile reconstruction. Moreover, the sensitivity of the CT inversion to the presence of the ground has been investigated, comparing then the results with the ABF ones. Inaccuracies of the CT reconstruction of the vertical structure of the volume only due to the presence of a ground component have been observed, even with low ground-to-volume ratios. For instance, with a ground-to-volume ratio of -6dB, the power of the reconstruction error between a volume-only and a complete (volume and ground) estimated profile can be higher than 20% with the full-baseline set, depending on the profile itself. On the other hand, the ABF estimator is in general less sensitive to the presence of the ground, obtaining significant errors only for ground-to-volume ratios greater than 0dB.

Finally, different polarization channels have been simulated by means of a MB extension of the RVoG model. Important changes on the estimated profiles have been observed at the change of the polarization channel, depending mainly on the difference in terms of ground-to-volume ratio between the channels, but also on the profile itself.

[7] Airborne horizontal baseline requirements can be easily translated into k_z requirements for a spaceborne mission.

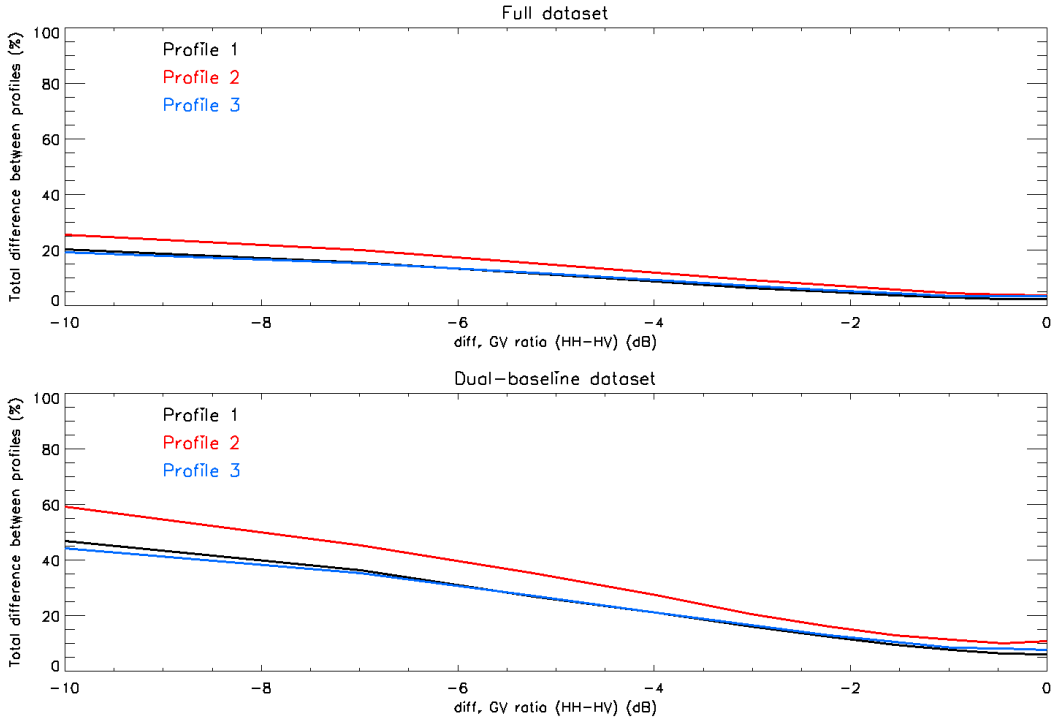

Figure 3.25 – RMS(ξ) as a function of a_{HV}^2, CT estimated profiles in HH vs CT estimated profiles in HV for the three reference profiles, with μ_{HH} = -3dB. Top panel: full-baseline set; bottom panel: dual-baseline set.

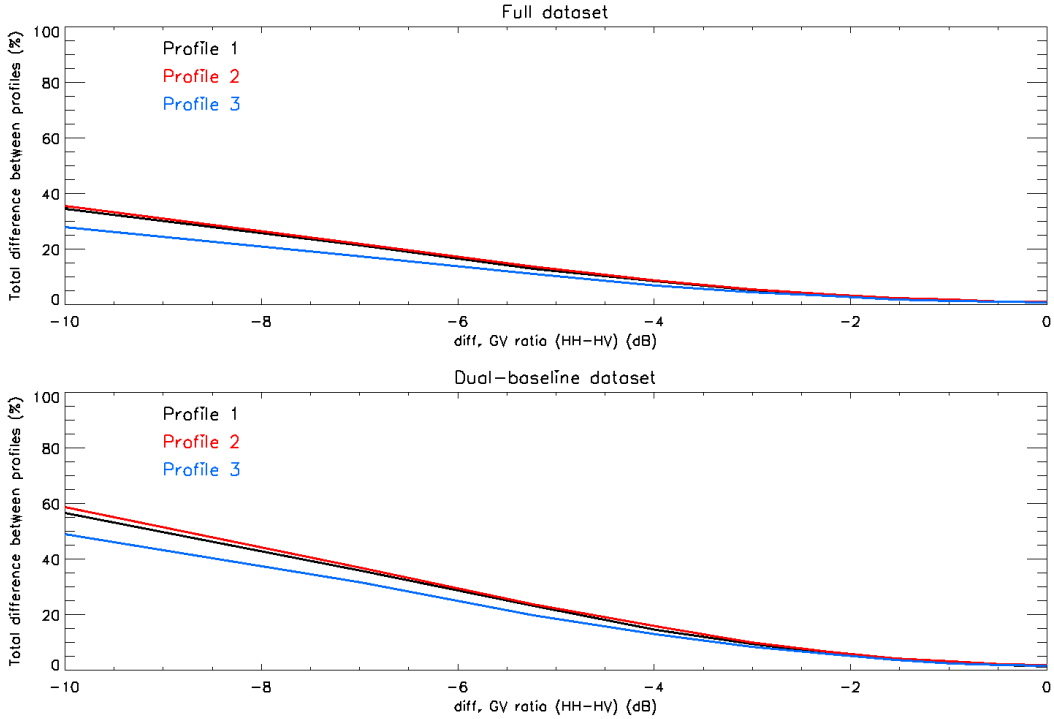

Figure 3.26 – RMS(ξ) as a function of a_{HV}^2, CT estimated profiles in HH vs CT estimated profiles in HV for the three reference profiles, with μ_{HH} = 3dB. Top panel: full-baseline set; bottom panel: dual-baseline set.

- This page intentionally left blank -

CHAPTER 4

EXPERIMENTS WITH REAL AIRBORNE DATA

4.1 The TempoSAR 2008 data set

During the TempoSAR 2008 campaign, the airborne SAR system E-SAR of the Microwave and Radar Institute of DLR acquired fully-polarimetric and MB interferometric SAR data over the Traunstein test site, a forest in the south-east of Germany, in the frame of the TempoSAR 2008 campaign. The master image of the data set is presented in Fig. 4.1, left panel, superimposed to a Google Earth image. The acquisitions were carried out in 6 day distributed during two weeks of the month of June 2008 (7th June - 20th June 2008) with 6 flight tracks for each day, excepted for the 8th June in which only two images have been acquired. Nominally, the 5 slave tracks are distributed in space making in order to realize baselines of 5, 10, 15, 25m with respect to the master acquisition, together with a 0-baseline acquisition for temporal decorrelation analyses. Thus, the data set has a sufficient number of different SAR images to perform a tomographic analysis for each day of acquisition (except for the 8th June). In each day, the images were acquired in a 1-hour span, thus it is reasonable to neglect temporal decorrelation effects and to assume stable the weather conditions.

The Traunstein test site is characterized by a heterogeneous forest, with different tree species (spruce, beech and white fir). On a global scale this forest type is part of the temperate forest zone. It is a managed forest composed of even-aged stands which cover forest heights from 10m to 40m. The mean biomass level is on the order of 210t/ha, significantly higher than other managed forests in the same ecological zone, while some old forest stands can reach biomass levels up to 500t/ha. The terrain topography varies from 600m to 800m amsl, with only few steep slopes.

To facilitate the analysis, we selected 5 areas inside the central part of the forest. The requirements for the area selection were the following: (*i*) homogeneous tree height above 20m; (*ii*) Flat topography; (*iii*) different biomass levels; (*iv*) at least 100 multilook cells of 20m by 20m in slant range and azimuth, respectively, for statistical analyses. The right panel of Fig. 4.1 shows a cut of the master SLC amplitude with superimposed in red the 5 selected areas, and their average forest height and biomass levels are plotted in Fig. 4.2. The average height is slightly higher than 30m, and it is remains quite constant (standard deviation in the order of 10% for each area). On the contrary, the average biomass varies from around 300t/ha of area no. 1 to 500 t/ha for area no. 5. This might indicate that area no. 5 is very rich of vertical structure.

Meteorological data for the Traunstein forest are available through the Bavarian State Research Centre for Agriculture (Bayerische Landesanstalt für Landwirtschaft, www.lfl.bayern.de), and they have been obtained from two local weather stations, Schönharting and Nilling, about 24 km north-east and north-west, respectively. Different meteorological measurements as air temperature (at a height of 20 and 200cm), soil temperature (in a depth of 5 and 20cm), relative humidity, wind velocity and precipitation were collected at an hourly rate. For this first analysis, the changes in humidity and temperatures (air and soil) are not taken into account. Only the wind velocity and precipitations are considered, as they would reasonably influence the 3-D structure as retrieved by SAR Tomography. In Fig. 4.3, wind speed (in m/s) and rain amount (in mm/h) are plotted for the entire duration of the TempoSAR 2008 campaign and for the two weather stations. Looking at the weather parameters, a wind speed up to 2.5m/s was measured on 7th June, which amounts to the double of the wind speed measured on 10th and 12th June. Hence, the MB acquisition on 7th June is discarded from our analyses, as it is expected to be more corrupted by temporal decorrelation. Concerning rain, the days between 7th and 10th June were dry, while it rained between 10th and 12th June (more than 13mm/h of water precipitation). Hence, for simplicity, from here on the 10th will be called the "*sunny day"* whereas the 12th will be called the "*rainy day"*. Therefore, the analysis of rainfall-induced effects on the estimated tomograms has been carried out using these two days of the TempoSAR 2008 campaign.

For the sake of completeness, we also evaluated the tomographic PSF for each MB acquisition. Forst of all, it was found that the acquisitions of 19th and 20th June have to be carefully considered due to problem of ambiguities and poor peak sidelobe level. Therefore, they have been discarded as well. On the contrary, the already selected acquisitions of 10th and 12th June have similar and good PSF, that are not expected to introduce 3-D focusing artifacts in the tomogram comparisons.

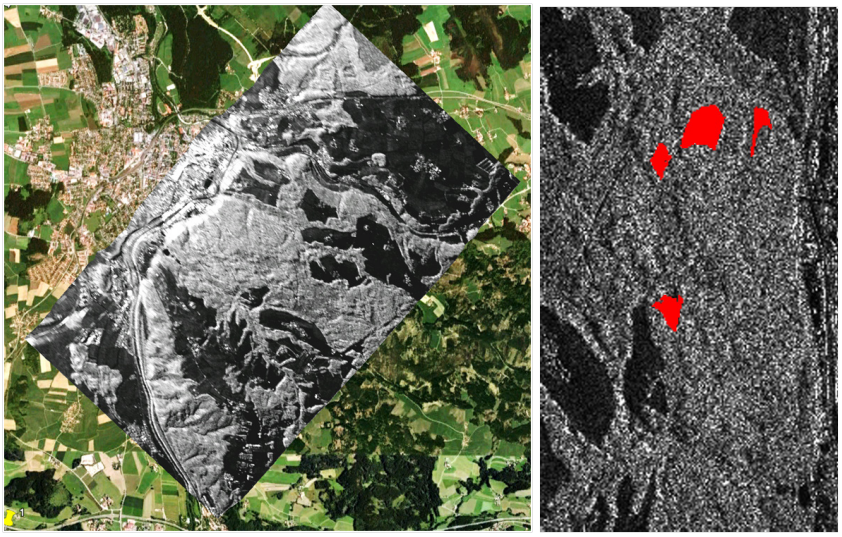

Figure 4.1 – Traunstein test site. Left panel: a SLC E-SAR SAR image of the test site, superimposed to a Google Earth image of the area. Right panel: selected areas for the analysis, colored in red and superimposed to a close-up of the SLC amplitude in slant range (horizontal) – azimuth (vertical) coordinates.

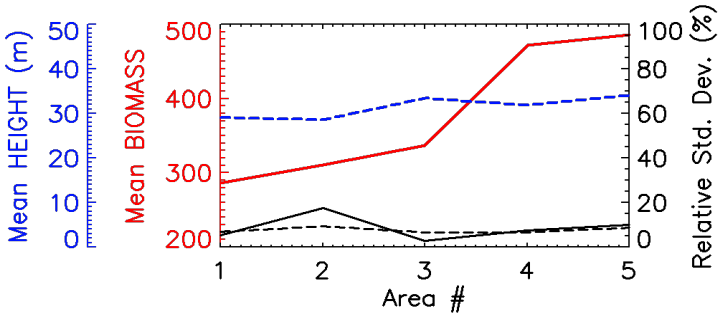

Figure 4.2 – Forest height and biomass characterizing the 5 selected areas in Fig. 4.1.

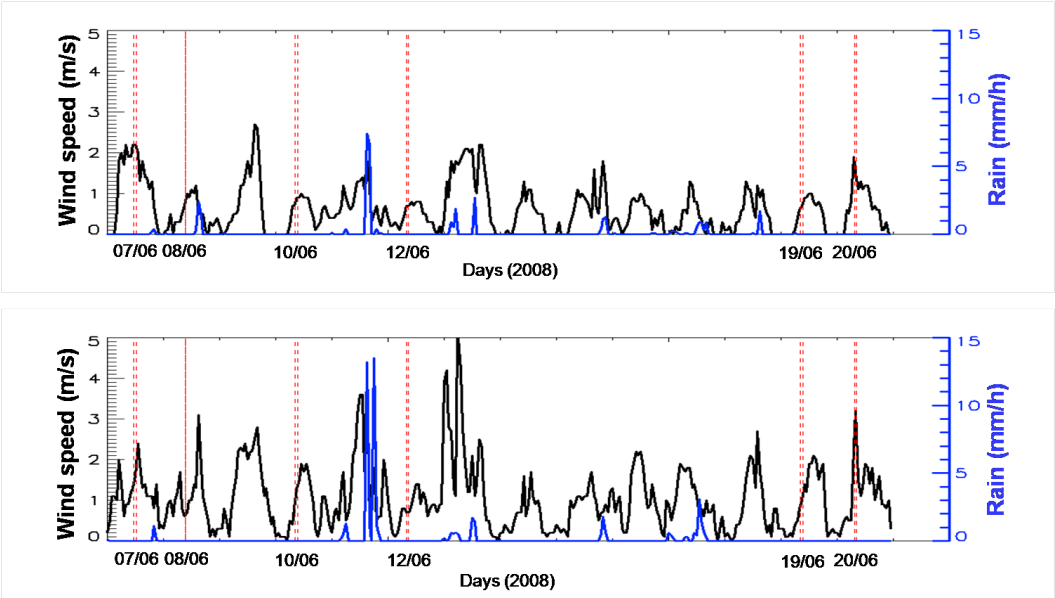

Figure 4.3 – Rain and wind measurements from Nilling (top panel) and Schönharting (bottom panel) weather stations. The red dotted line indicates beginning and end of the MB acquisition for each day.

4.2 Reference measurements

The forest of Traunstein has already been utilized for more than 100 years for forest growth and forest yield studies from the Chair of Forest Yield Science of the "Technische Universität München" (TUM), and therefore it is well documented with high precision ground measurements. Two extensive ground inventory surveys are available. The first ground survey took place in 1998, the second one in 2008. Both ground surveys were done by means of inventory plot measurements on a grid basis. A 100×100 m-spaced grid was laid over the test site with an inventory point at each cross section. Each plot is circular with a radius of 12.62m and represents an area of 500m². A map with all the inventory plots superimposed to a SAR image of the test site is shown in Fig. 4.4 (utmost left panel). Most important measurement parameters of the inventory survey for a validation of remote sensing products are tree height, tree diameter (dbh) and tree species information (needed for biomass estimation).

In 2008, the ground inventory survey was accompanied with a Laser scanning flight (July 2008) to provide complete forest height measurements all over the test site. Laser scanning data provided a digital terrain model (DTM, Fig. 4.4, mid panel) and a digital surface model (DSM), from which a forest height map (the so-called H100) was calculated (Fig. 4.4,utmost right panel). As mentioned in Section 4.1, the topography of the test site is characterized by moderate slopes, with slope angles usually lower than 15°. From the LIDAR H100 map, the heterogeneity of the forest in terms of tree height can be observed. Indeed, the tree heights in the Traunstein forest ranges from 10m up to40, with stands characterized by even taller trees.

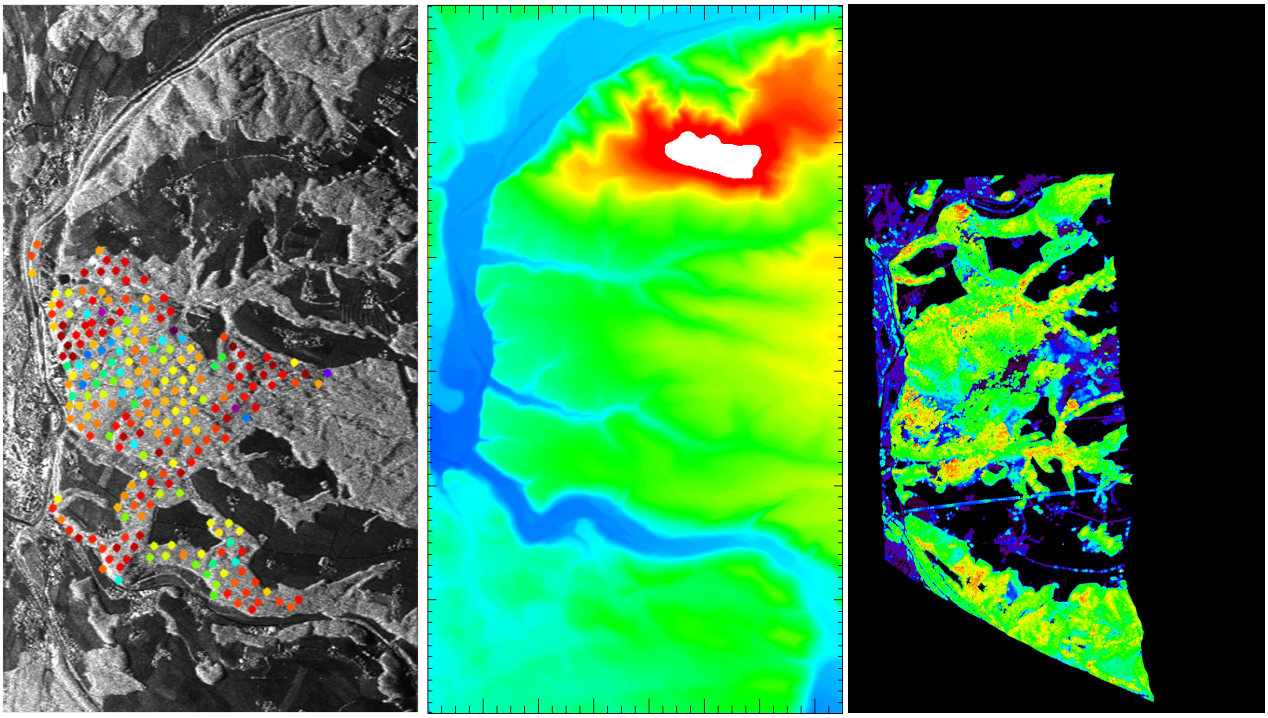

Figure 4.4 – Location of the inventory plots (left), colour-coded with tree height information, a LIDAR DTM (middle) and a LIDAR h100 map (right) .

4.3 Tomographic vertical structures and biomass profiles

The retrieval of 3-D above-ground biomass profiles in dense forests using SAR images is widely recognized as a challenging task, because of the saturation of the backscattered power at high biomass values. On the contrary, as already said, MB techniques allow the 3-D imaging of the forest volume and can therefore be employed to estimate biomass profiles and remove saturation effects intrinsic to a single image. In this section, some TempoSAR 2008 radar tomograms are shown and compared with measured biomass profiles. Biomass profiles have been calculated by feeding an ecological model with tree parameters like trunk and canopy diameters. Six out of 240 biomass profiles are presented in Fig. 4.5 (top panel), and they have been extracted in correspondence of very tall plots. Counting from the left side, the 3rd, 4th and 6th profile present also non-negligible understory contributions. Tomographic profiles have also been estimated by the radar MB data vectors in the same coordinates by processing HH, HV, and VV channels (Fig. 4.5, bottom panel). From 4.5, it is apparent that the different biomass components are mapped into the radar profiles. Moreover, it can also be generally observed that for instance, when the canopy layer is characterized by a low biomass level, also the backscattered power contribution on the correspondent radar estimated structure is usually lower than for the other tomographic profiles. Moreover, the estimate radar profile changes with the polarization channel. As a consequence, the polarization-diversity can be exploited to retrieve more information about the real biomass profile.

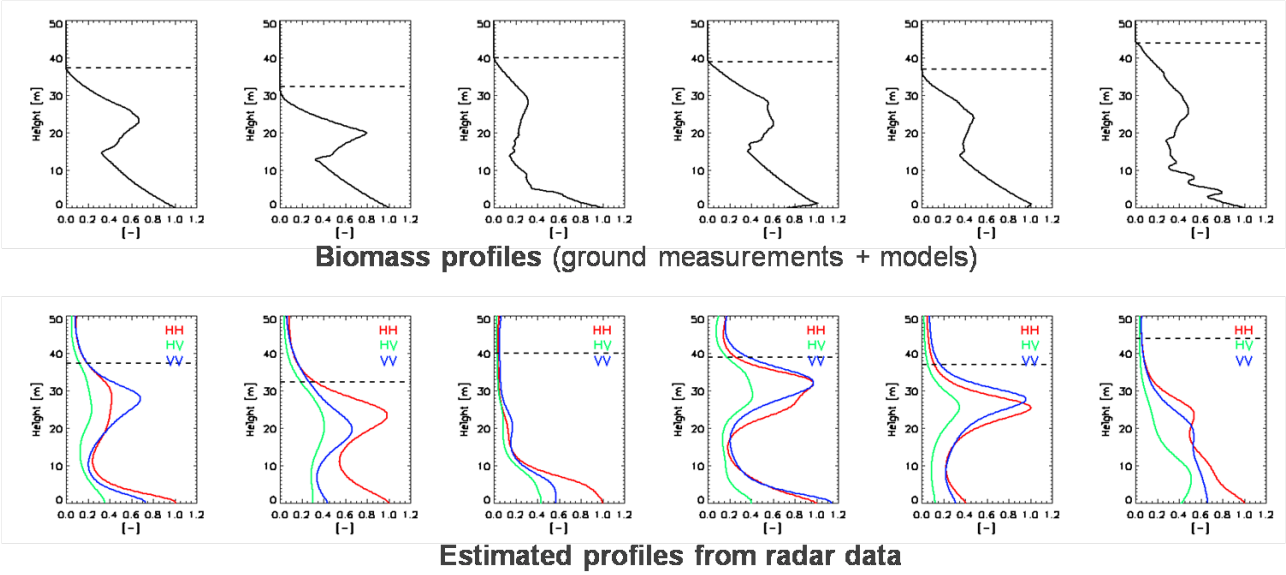

Figure 4.5 – Examples of biomass profiles (top panels) and corresponding ABF tomographic profiles (bottom panels).

4.4 Expected rainfall-induced effects

SAR systems operating at L-band are characterized by deep penetration capabilities into volumes, enabling the generation of maps of forest biomass, forest type, tree moisture content, and even soil moisture content and flooding under forest canopies from radar images [*Way*, 1990], [*Dobson*, 1991], [*Ahern*, 1993], [*Rignot*, 1994], [*Proisy*, 2000]. Although during the last years the interest is continuously grown in the

estimation of forest parameters employing SAR systems, no works examine the 3-D backscatter changes when a forest becomes wet. Before presenting our observation from real data experiments, a small summary of the expected rainfall-induced effects on the estimated vertical profile is presented according to the available literature [*Ulaby*, 1987], [*Monteith*, 1965], [*Hinckley*, 1978], [*Horton*, 1919].

A Tomo-SAR L-band profile of a forest includes backscattering components from both tree volume structure and ground level. The radar backscatter of trees is mostly related to the dielectric constant of tree tissues, which in turn depends strongly on their water content [*Ulaby*, 1987]. These tissues, especially the leaves, control their water content by transpiration [*Monteith*, 1965], [*Hinckley*, 1978]. During a rainfall, the water is retained in the form of small droplets or as a thin waterfilm upon the surface of leaves and branches [*Horton*, 1919]. A canopy can retain up to a certain amount of water, the so-called *maximum storage capacity*, and then, if it is still raining, the extra amount of water drops to the ground. As a consequence, immediately after a rainfalls the hydrologic properties of the tree structure change. This makes the dielectric constants change. In terms of backscattered power, an increase of the backscattering contribution from the top of the canopy is expected, due to the waterfilm on the leaves that makes these tissues less transparent to the radar waves. Later on, the waterfilm reduces the transpiration of the leaves, and so doing their water content increases. In radar terms, an increase is observed of the canopy backscattered power and of the extinction of the volume layer due to absorption phenomena. Concerning the ground, after maximum storage capacity is reached, the dropping water increases the soil moisture. Therefore, the backscattered power from the ground should increase, but this effect is counter-balanced by the higher extinction of the volume which reduces the electromagnetic power reaching the ground.

To sum up, by comparing a Tomo-SAR profile after a rainfall with the same profile before the rainfall, we expect to observe the following effects: a decrease of the ground-to-volume power ratio (due to an higher extinction), an increase of the phase center height of the estimated vertical profile (due to both a stronger power contribution of the top of canopy and a lower penetration of the electromagnetic waves), and a general change of layer powers. The effects on a possible estimated vertical structure are sketched in Fig. 4.6, where a vertical structure and a possible extinction profile in dry condition are reported in red lines, while the two curves modified following the expected induced-weather effects are reported in green lines.

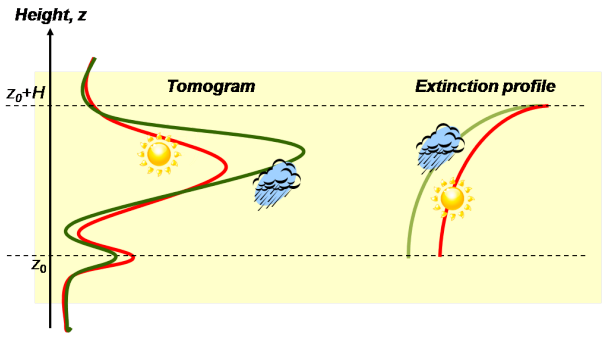

Figure 4.6 – Induced-weather effects on a tomographic profile: model of a vertical estimated structure (left) and the extinction profile (right), in dry condition (red lines) and in wet condition (green lines)

4.5 Observed rainfall-induced effects

In this section, experiments with real E-SAR data are presented. First of all, differences in the profiles between the sunny and rainy day are quantified height by height by means of ABF. Secondly, variations in the total backscattered powers coming from ground and volume layers of the structure are estimated and analyzed using M-RELAX. Since it has been demonstrated that low vertical frequency components of the profile [*Toraño*, 2010] are related to the biomass components, the CT profiles are estimated and compared to the ABF ones, which express the whole vertical frequency spectrum.

4.5.1 Analysis of the ABF profiles

The objective of this first analysis is to observe differences between the backscattering powers coming from some significant heights in the MB data acquired in a rainy day and a sunny day. The ABF has been used to estimate the power at each height due to its high vertical resolution capabilities. In order to ensure the highest possible radiometric fidelity, an accurate MB phase calibration had been carried out before the tomographic processing, and the ABF was implemented by carefully selecting the diagonal loading factor. The LIDAR DTM and H100 information were used to define the ground height, to divide forest areas to bare soil and to obtain information about the height of the trees.

The powers backscattered at the ground level are shown in Fig. 4.7 for the sunny and the rainy day in the HH channel. Very low backscattering powers are found on bare soil, especially in far range where the look angle reaches 40°-50°, mainly due to reflection phenomena due to surface scattering. Regarding the influence of weather conditions, higher backscattering powers are observable in the forest areas dry conditions with respect to the same areas after a rainfall. As mentioned in the previous section, this can be explained supposing that the higher extinction of the canopy dominates on the increase of ground backscattering due to an increase of moisture. This trend is more visible in areas with tall (dense) trees in which the attenuation of the canopy layer is stronger. At 10m over the ground (Fig. 4.8), stands shorter than 10m present no backscattering, as it is reasonable to expect. Where the tree height is around 10m, the backscattering comes from the top of the canopy. In this case, higher power levels are observable in the wet day with respect to the dry day, probably due to a higher amount of water inside and on the leaves. Focusing now on the 20m-layer above the ground (Fig. 4.9), in which trees are supposed to be more dense and mature, the backscattered power is much higher in the wet day than in the sunny day, and differences are more apparent than in the lower layer. This effect is further amplified in the 30m-layer (Fig. 4.10), although in this case, the number of stands backscattering in this layer are much less than in the other layers.

This very simple comparison demonstrate very clearly that the estimated structure at L-band is sensitive to different weather conditions and, in particular, the backscattered power coming from the top of the canopy is higher after rainfalls than in dry conditions, probably mostly due the increased extinction and in a minor part to an higher amount of water held by the canopy layer.

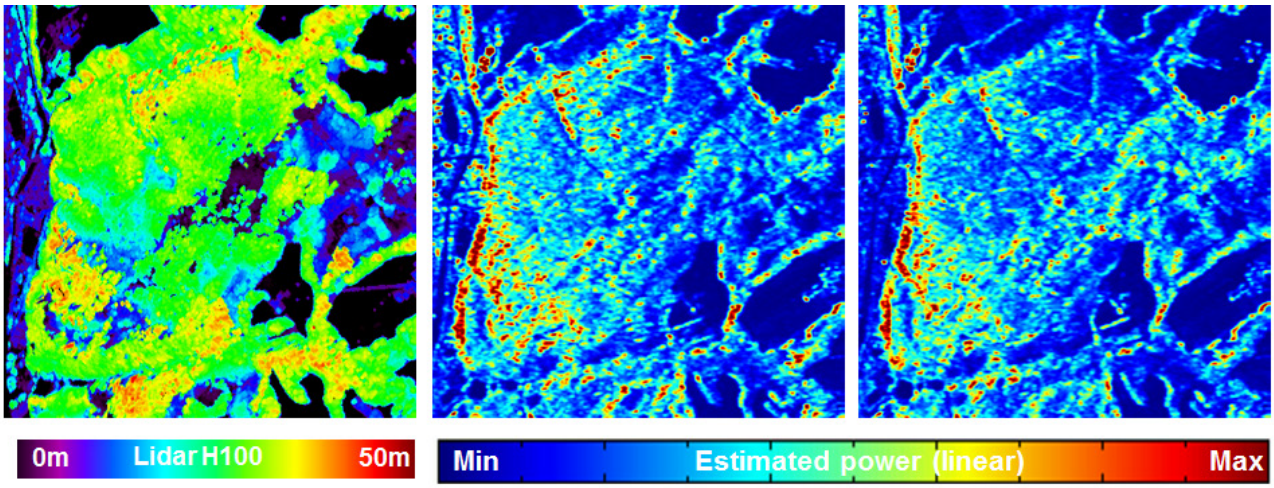

Figure 4.7 – Ground layer: Lidar H100 (left), ABF powers in the sunny (mid) and in the rainy day (right).

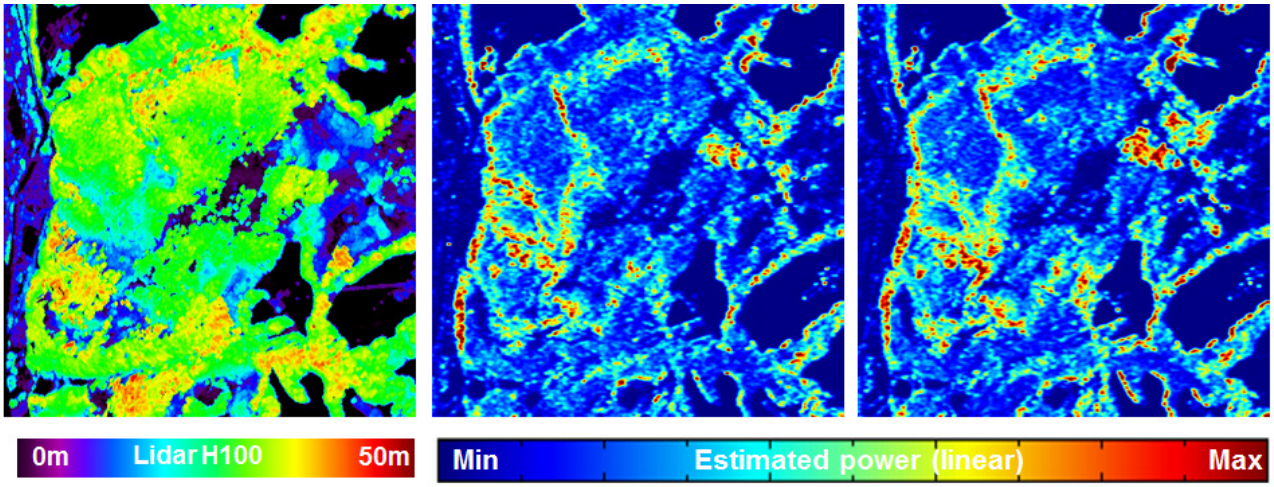

Figure 4.8 – Layer 10m above ground: Lidar H100 (left), ABF powers in the sunny (mid) and in the rainy day (right).

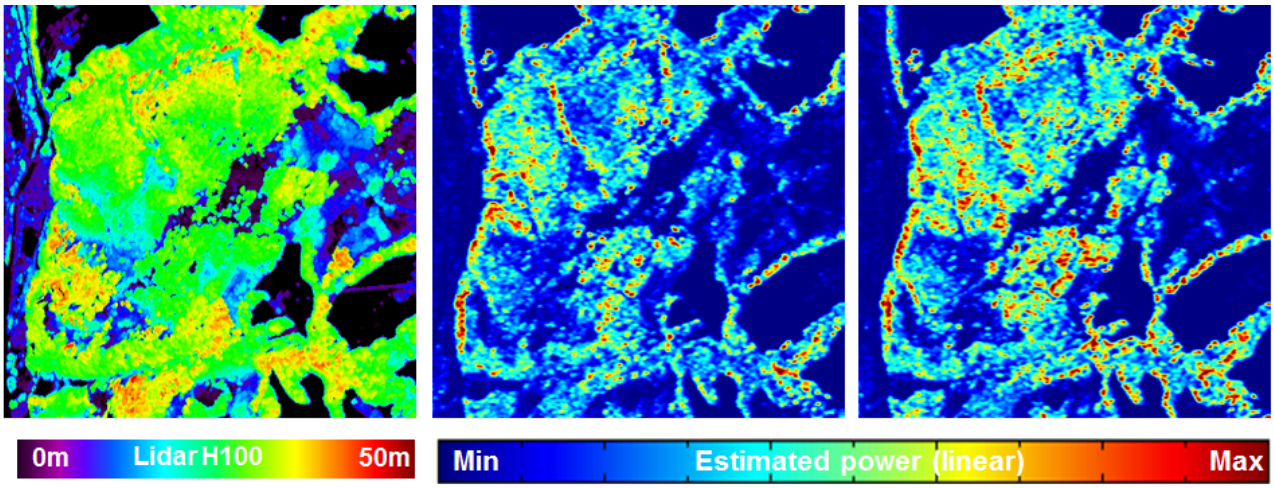

Figure 4.9 – Layer 20m above ground: Lidar H100 (left), ABF powers in the sunny (mid) and in the rainy day (right).

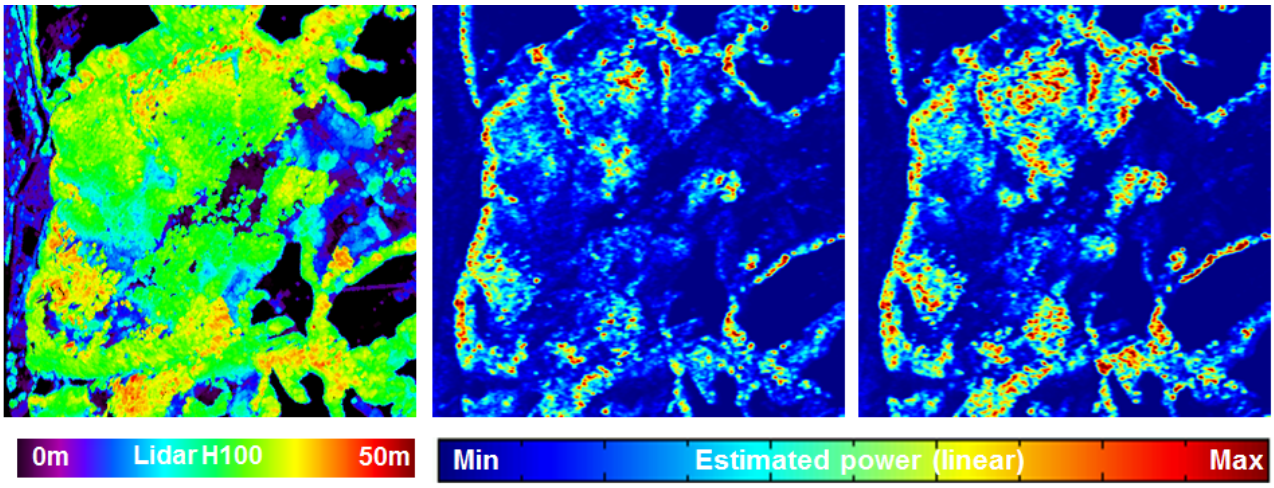

Figure 4.10 – Layer 30m above ground: Lidar H100 (left), ABF powers in the sunny (mid) and in the rainy day (right).

4.5.2 Change of the phase center height of the ABF profiles

In this section, the changes of the phase center height of the ABF profiles are quantified. Fig. 4.11 shows the maps of the phase center height in the central forest area of Traunstein in the sunny and in the rainy day. Sensitive differences between the two days are visible, especially in the areas with tall trees (see figures before for the H100 corresponding to the area). The phase center of profiles estimated from data acquired in wet conditions is usually higher than in dry conditions. This trend is a direct consequence of the higher extinction, but it could also be due to changes on the estimated structure.

The phase centers calculated on profiles estimated after and before the rainfall are compared in a scatterplot for areas no. 1 and no. 5 (see Section 4.1), reported in Fig. 4.12. The motivation behind the choice of these two areas is that they are characterized by approximately the same forest height, but very different biomass levels, thus indicating a high difference also in terms of vertical structure. In area no. 1, in the HH channel, after the rainfall the 99% of multilook cells exhibits an increase of the phase center height, amounting in average to 2,75m. In the remaining 1% of cells a decrease of 0.57m can be observed. In HV channel, an average increase of 1.97m of the phase centers height is observed in the 85% of cells, while in the remaining 15% of cells the decrease amounts to 0.92m. This trend is apparent also for area no. 5, though with different numbers. In HH polarization, the increase of the phase center height after a rainfall reaches the average of 3.55m (the 97% of cells), and a decrease of 0.53m (3% of cells). In HV polarization, the 92% of cells shows an increase of 1.97m and the 8% a decrease of 0.35m. In general, for both the areas, it can be observed that the HV channel is less sensitive than the HH channel to different weather conditions, reasonably due to a lower backscattering from the ground layer. Therefore, the change of phase center height in HV can be considered (at least at the first order) as an indication of the change of Tomo-SAR profile of the vegetation component.

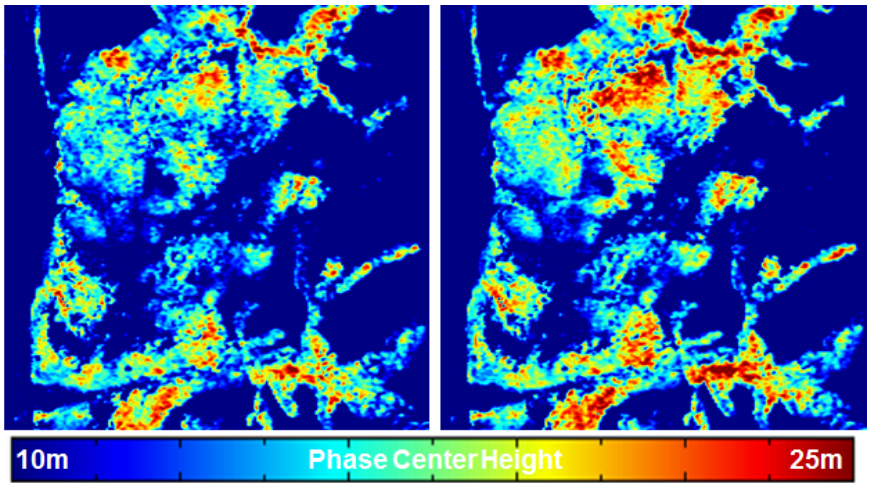

Figure 4.11 – Phase center height calculated by means of ABF profiles in the sunny day (left) and the rainy day (right).

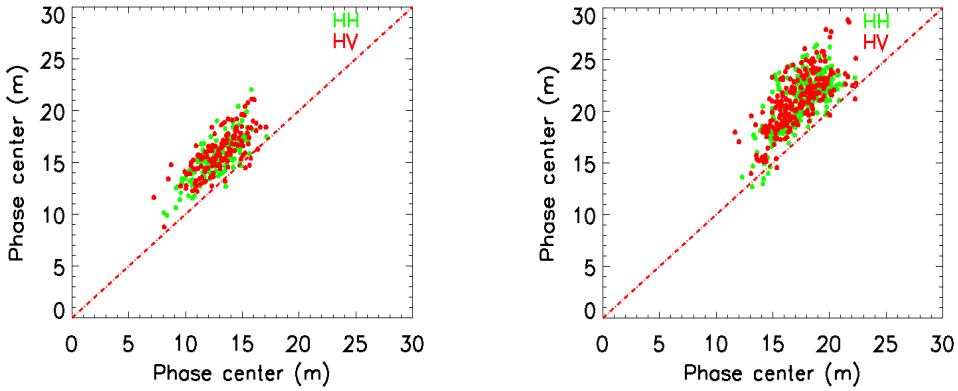

Figure 4.12 – Scatterplot of ABF phase center heights, area no. 1 (left) and area no. 5 (right). Horizontal axis: before the rainfall; vertical axis: after the rainfall.

4.5.3 Change of the ground-to-volume power ratio

In this section, changes of the ground-to-volume power ratio μ are under investigation. The M-RELAX algorithm is used to estimate this parameter (see Chapter 2). The maps of μ estimated for the dry day and for the wet day are shown in Fig. 4.13. The observation of these maps does not allow a straightforward interpretation of the results. Indeed, Traunstein is a very heterogeneous forest and μ ranges from -8dB to 3 dB, a large interval of values. Anyway, some differences can be recognized especially in the areas with tall trees (found by using the LIDAR H100), with usually lower μ for the wet day with respect to the dry day. Considering again areas no. 1 and no. 5, this trend is more visible and it is possible to quantify the changes. For area no. 1 (Fig. 4.14, left panel), in HH channel the 81% of the cells exhibits a decrease of μ of 1.45dB in average in the wet day with respect to the dry day, whereas in only the 19% of the cells an increase of μ of only the 0.56dBcan be observed. In the HV channel, the values of μ in both days are usually

lower with respect to the HH channel and also with smaller changes in average. In detail, the 64% of cells show a decrease of μ of 1.23dB in average in the wet day with respect to the dry day, whereas in the remaining 36% of cells an increase of 1.03dB can be seen. For area no. 5 (Fig. 4.14, right panel), the values are slightly different, but the trend is the same. For the HH channel, the 66% of cells shows a decrease of μ of 1.19dB, whereas in the 34% of cells μ increases of 1.10dB. Finally, regarding the HV channel, in the 64% of cells, μ decreases of 1.07dB in average, whereas in the 36% of the cells μ increases of 0.82dB.

To sum up, a decrease of μ after rainfalls has been observed in both areas. Three different causes can produce a variation of μ: a variation of the volume power, a variation of the ground power, or both at the same time. The differences (wet day with respect to dry day) of ground and volume powers at the change of the weather condition are shown in Fig. 4.15 for each cell inside areas no. 1 and no. 5. While the volume powers do not change significantly in average between the two days, a significant decrease of the ground powers is observable. Concerning the volume layer, a possible interpretation (to be further assessed) could be that some hours after rainfalls (therefore in absence of the water film on the leaves) the increase of the amount of water inside the tree trunk produces a different distribution of the backscattering powers along the volume layer, but the total power approximately does not change. On the other hand, the increase of the extinction of the canopy layer (due to the higher water absorption) produces a decrease of the ground backscattered power, and dominates on the increase of its backscattered power that should result from an increase of soil moisture. This trend is visible in both the selected areas, but the changes depend on the area itself. Hence, these power changes due to different environmental condition are structure-dependent.

In Section 4.5.2, different interpretations were given to explain the significant increase of the phase center height after the rainfall. One possible interpretation is that the increase of the phase center is only related to a decrease of the μ. Another possible explanation contemplates a change in the backscattering power distribution in height due to a variation of the hydrological properties along the whole tree. To have a first indication, in Fig. 4.16, the changes in μ ratio (after with respect to before the rainfall) are related to the variations in the phase center heights by means of a scatterplot. Considering area no. 1, usually the increase of the phase center height corresponds quite linearly to a decrease of μ. In area no. 5, this trend is still visible, but with a higher dispersion. More importantly, there is a considerable amount of cells in which an increase of the phase center height corresponds to an increase of μ. Thanks to this observation, it is possible to conclude that in general the changes in μ and in the phase center height are (linearly) related, but the hydrologic changes in the tree trunk and leaves after rainfalls cause changes in the estimated structure itself, modifying in this way the power contribution of each layer to the total Tomo-SAR vegetation-only structure without a predictable trend.

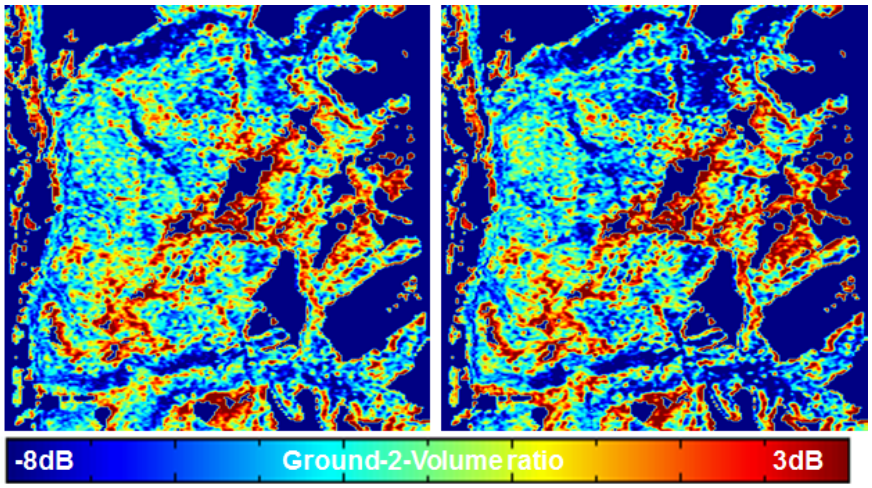

Figure 4.13 – Ground-to-volume power ratios calculated by means of M-RELAX in the sunny day (left) and the rainy day (right).

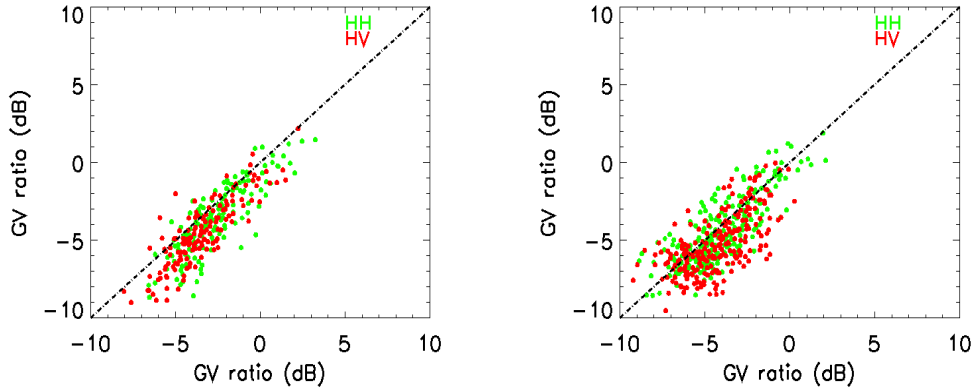

Figure 4.14 – Scatterplot of ground-to-volume power ratios, area no. 1 (left) and area no. 5 (right). Horizontal axis: before the rainfall; vertical axis: after the rainfall.

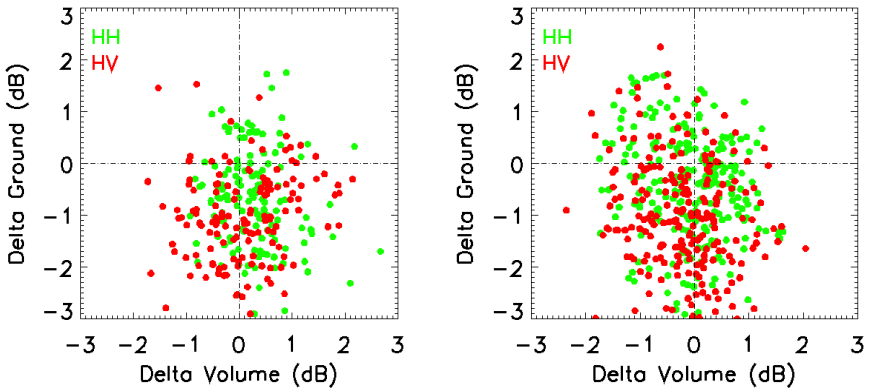

Figure 4.15 – Estimated power differences (wet with respect to dry) at the ground level against volume, area no. 1 (left) and area no. 5 (right).

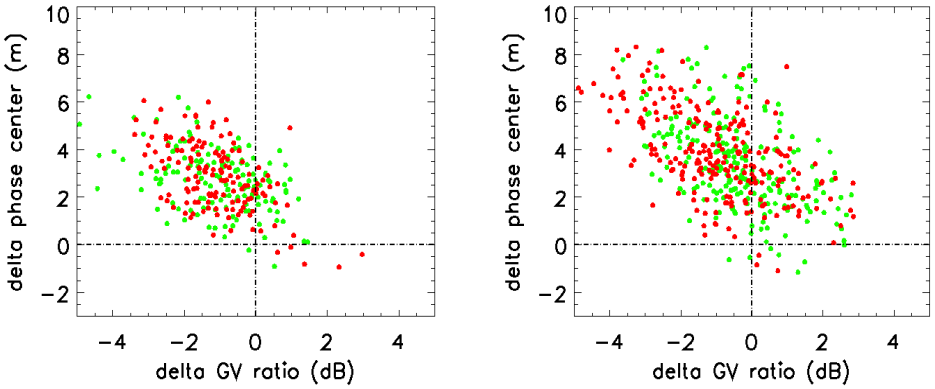

Figure 4.16 – Estimated phase center height differences against power differences (wet with respect to dry), area no. 1 (left) and area no. 5 (right).

4.5.4 Dependence of the rain-induced effects on the tree species

In the previous experiments, it was apparent that weather-induced effects are structure-dependent. Here we present a first experiment to understand if they also depend on the tree species. By means of the ground measurements, it was possible to discriminate between cells dominated by broadleaves and cells discriminated by conifers. The leaves of these two classes of trees have different characteristics, and they could therefore influence differently the propagation after a rainfall. The scatterplots in Fig. 4.17 show the changes in μ and phase center height for the cells in which ground information was available. Conifers do not seem to be sensitive to different weather conditions on average. On the other hand, changes on the can be observed in the cells dominated by broadleaves, especially concerning μ. Indeed, μ decreases of 1.5 dB on average after a rainfall, with values greater than 3dB for some points. These first results indicate a species dependency, however further investigations are needed to definitely asses this issue.

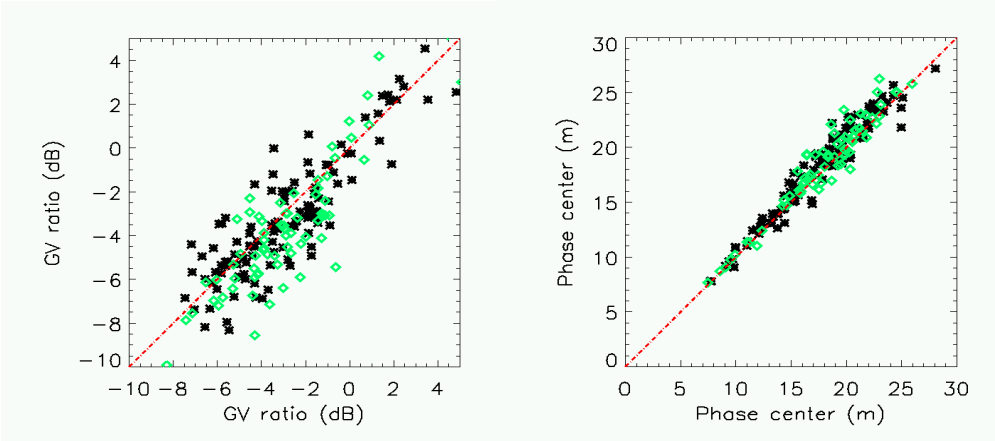

Figure 4.17 – Scatterplots of ground-to-volume power ratios (left) and phase center height (right). Horizontal axis: before the rainfall; vertical axis: after the rainfall. Green diamonds: broadleaved cell; black crosses: conifer cell.

4.5.5 Changes in the estimated profiles

In this section, the changes of the entire tomogram are quantified. The analysis is carried out only inside the selected areas, considering both the total difference of the profiles (as defined in equation (3.4)) and the changes height-by-height. The ABF estimator is firstly considered, taking advantage of its high resolution even with a small number of baselines. The ABF estimator is non-parametric, and it conveys information about *all* of the backscattering vertical frequencies in the profile. Beside ABF, the CT profiles are considered as well. Here, CT is implemented by using the Legendre polynomials as expansion basis. In this way, limiting to the expansion to the first four coefficients (i.e. until the third order polynomial), CT estimates only the low-vertical frequency backscattering components.

4.5.5.1 Differences in the ABF profiles

In the comparison of profiles estimated in different weather conditions, a first objective is to quantify the height-integrated difference ξ, calculated as in equation (3.4), taking as a reference the profile obtained in the dry day. Maps of ξ for the selected areas are shown in Fig. 4.18 for the selected areas in the HH (top panel) and in the HV (bottom panel) polarization channels, color coded from 0% (blue) to 100% (red). high values can be observed. These height-integrated differences are also plotted through histograms in the same figure. Different total differences have been obtained in different areas. In the areas no. 1, no. 2 and no. 5 ξ is considerably high, while it is lower than 30% in the most of the cells in the areas no. 3 and no. 4. A more detailed analysis can be carried out by interpreting the normalized histograms. Regarding the HH polarization, areas no. 3 and no. 4 are less sensitive to different weather conditions than the others, with values of total difference grouped around 10-20%. On the contrary, the histograms corresponding to areas no. 1, no. 2 and no. 5 are more spread along the entire range of values of ξ, even higher than 80%. These trends are visible also for the HV channel, but the values are usually lower than in the HH polarization. As said in the previous sections, this lower sensitivity to rainfalls of the HV channel with respect to the HH channel might be reasonably due to a general lower sensitivity to the ground layer.

The next objective is to quantify the change of the profiles for each height. Fig. 4.19 plots the average normalized profile change as a function of the height, taking as a reference the profile of the dry day. It is apparent that the power contributions from the canopy layer (around 25-30m in height) are higher in a wet day than in a dry day, for both the polarizations, and the difference is higher than 50%. Going down to 20m height (i.e. after 5-10m of canopy towards the ground), the profile difference vanish. For lower heights, close and onto the ground level, the increase of the extinction after the rainfall produces attenuation, and the backscattered power decreases between the 10% and the 40%.

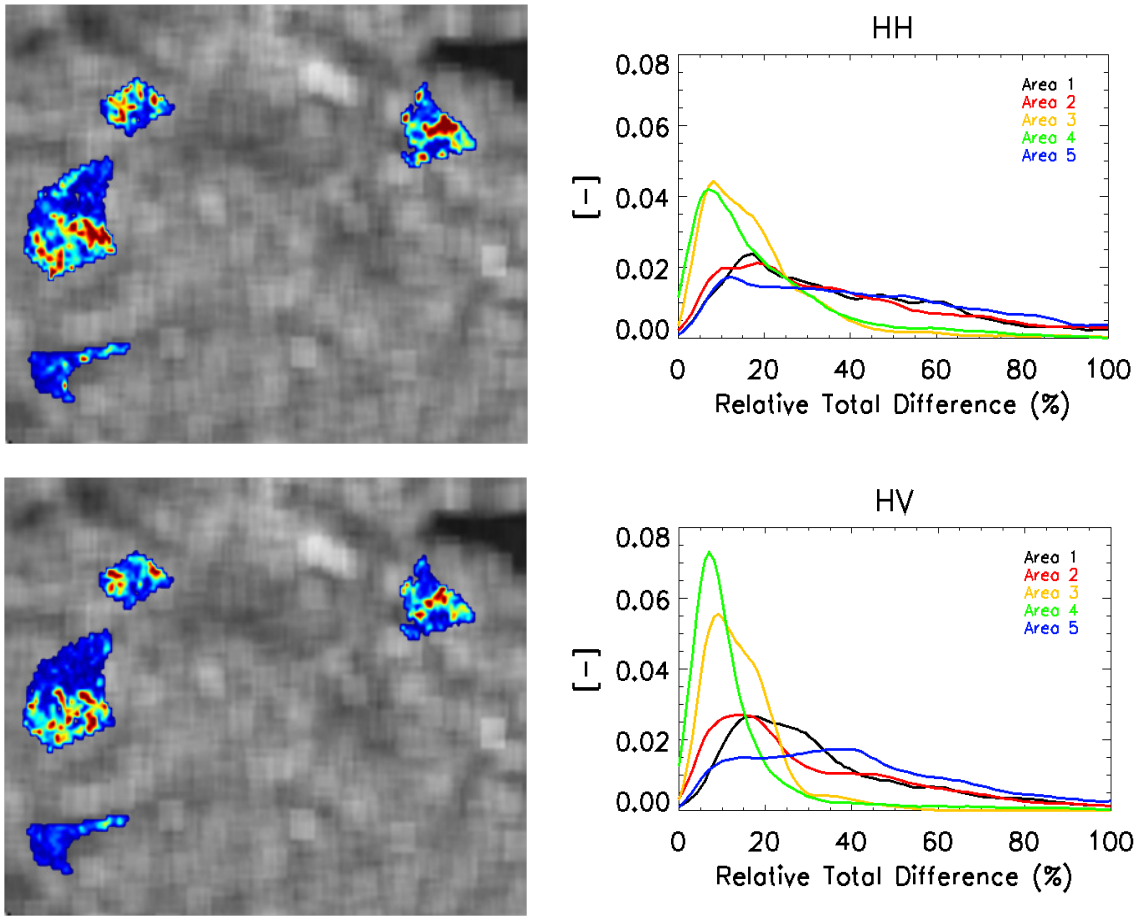

Figure 4.18 – Total integrated difference of the ABF profiles in the wet day with respect to the dry day, expressed in %. Right panel: difference maps in range-azimuth for the areas of interest color-coded between 0% (blue) and 100% (red); right panel: normalized histograms of the integrated profile difference for the selected areas. Top panel: HH polarization channel; bottom panel: HV polarization channel.

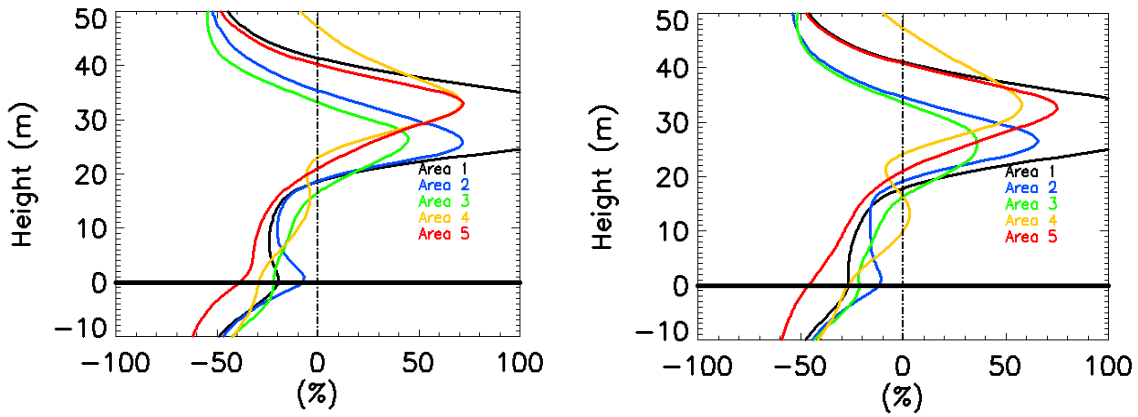

Figure 4.19 – Average profile difference as a function of height, ABF profiles, wet day with respect to dry day. Left panel: HH polarization channel; right panel: HV polarization channel.

4.5.5.2 Differences in the CT profiles

The estimated CT coefficients on the central forest part of Traunstein are shown in Fig. 4.20 for both the dry and the wet days. Here, the coefficient related to the first, second and third order polynomials are shown, as the zero-order coefficient is set to 1 (see Chapter 2). It is apparent how different stand produce different sets of coefficients in each acquisition day. Furthermore, relevant differences are observable between the homologous maps estimated in the dry and in the wet day. This is a first indication that CT is sensitive also to both different stands and to different weather conditions, although only a very low number of coefficient is used.

Analogously to Fig. 4.18, in Fig. 4.21 shows the total differences ξ of the profiles estimated in the wet day with respect to the dry day. Again, only the selected areas are taken into account, and the results are presented in color-coded maps with the relative total difference expressed in percentage, together wittheir normalized histograms. It is apparent how, considering only the low vertical frequency components of the backscattering, the changes on the estimated profiles due to different weather conditions are lower with respect to the all-frequency ABF case, shown in Fig. 4.18. Some changes are still visible, but at a much lower extent. Looking at the normalized histograms and considering the HH polarization, the values of ξ are mostly concentrated around 5-15% with lower values on the tails with respect to the histograms calculated from the profiles estimated with the Capon method. Only the histograms of area no. 5 are more spread, with high values also on the tails. No significant differences can be found between the histograms in the HH and in the HV channel.

The average height-by-height profile difference of a wet day with respect to a dry day are shown in Fig. 4.22 for area no. 1. The mean profile is plotted in red, while in blue are plotted the profiles calculated adding and subtracting the standard deviation to the mean values. An increase of the phase center after the rainfall is still visible also on the low vertical frequency component. Furthermore, an increase of the extinction is also observable, as the profile estimated in wet conditions presents a higher slope in correspondence of the canopy layer. The same trend is visible also for area no. 5 (Fig. 4.23). For this area, the phase center height increases more than in area no. 1. This trend was also observed for the all-frequencvy ABF profiles. Considering now the component at the ground level, something unexpected can be noticed in these profiles. Indeed, in wet conditions the ground component is higher than in dry condition for both the areas, although the presence of a higher extinction. On the contrary, a decrease of the ground component was found during the analysis with the ABF and the M-RELAX estimators. It is worth noting that a big change of the CT profiles with and without ground was already noticed in Chapter 3.

One way to investigate this disagreement between the different profile estimators is to resort to a simulated analysis. The results are presented in Figs. 4.24 and 4.25. A model constituted by a set of Gaussian-shaped functions multiplied by a negative exponential to simulate extinction (calling σ the exponent) has been employed to create a parametric synthetic structure. By modifying the model parameters using the E-SAR settings, it is possible to simulate different sets of coherences corresponding to different structures, and to derive the related CT coefficients. The model parameters have been set in order to achieve

a CT profile similar as much as possible similar to the average one in the area no. 1 in dry conditions. In the first simulation (Fig. 4.24), only the extinction (governed by the negative exponential) is changed. The extinction parameter σ assumes values of 0.01, 0.03 and 0.05. The slope of the CT profiles at the canopy level increases at the increase of the extinction, and the ground component increases in amplitude, as observed in real data. Therefore, it is possible to conclude that the increase of the ground component is an artifact, probably due to the specific basis of polynomials used to reconstruct the profile. In the second simulation (Fig. 4.25), only the phase center height (governed by the position in height of the Gaussian functions) varies from the reference structure. Also for this simulation, the effects of the increase of the phase center height are visible, and follow the same effects observed on the real data. Again, these changes produce an increase of the ground component, probably due to the shape of the polynomials, and therefore to a mere fitting artifact.

In conclusion, the low vertical frequency presents the same weather-induced effects as observed in the all-frequency case, but at a much lower extent. Thus, low frequency components are robust to weather variations, and are therefore suitable for applications like forest classification or biomass estimation. However, the price to pay is a reduced simplicity of interpretation of the profile. A possible way to overcome this (minor?) shortcoming could be to change the expansion basis, but still maintaining the vertical frequency selectivity of the basis functions. This aspect could be further investigated in future works.

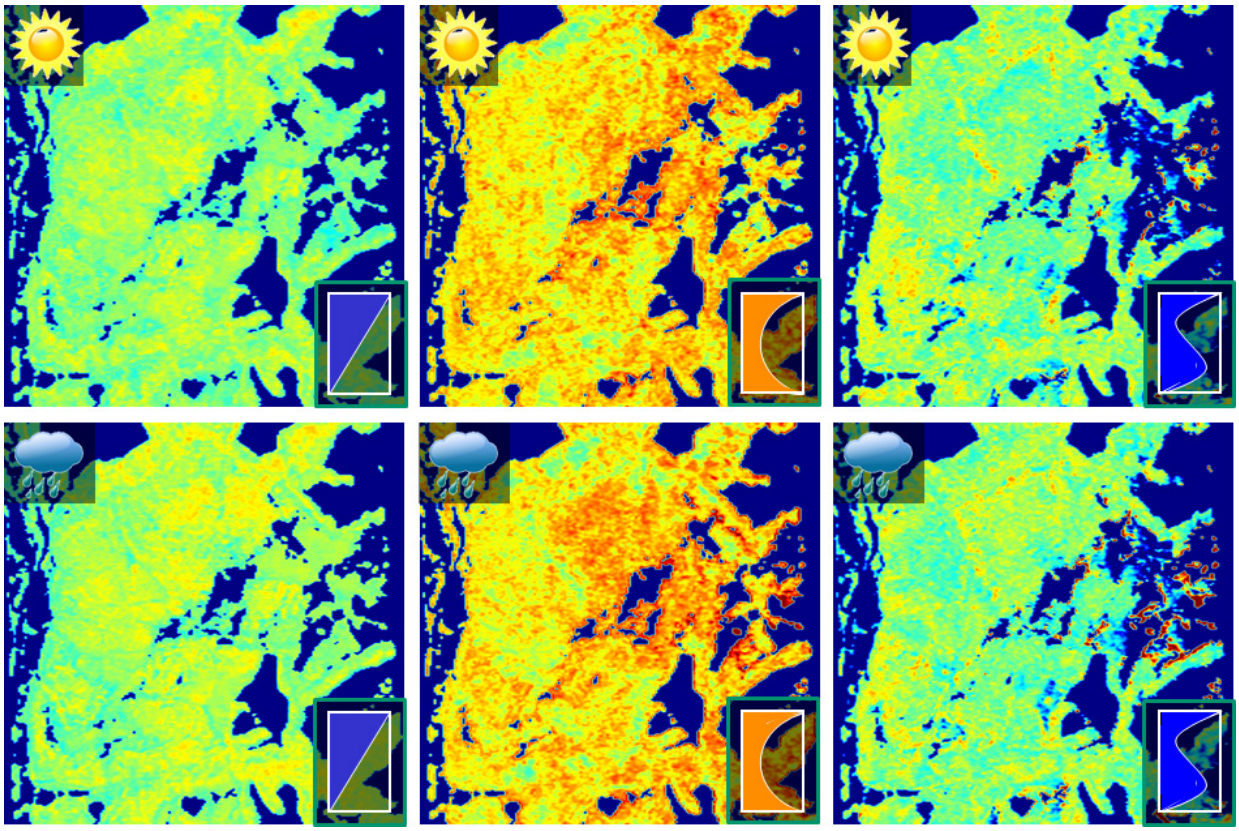

Figure 4.20 – Estimated CT coefficients in the range-azimuth plane. From left to right: coefficient corresponding to the first, second and third order polynomials of the Legendre basis. From top to bottom: dry day and wet day.

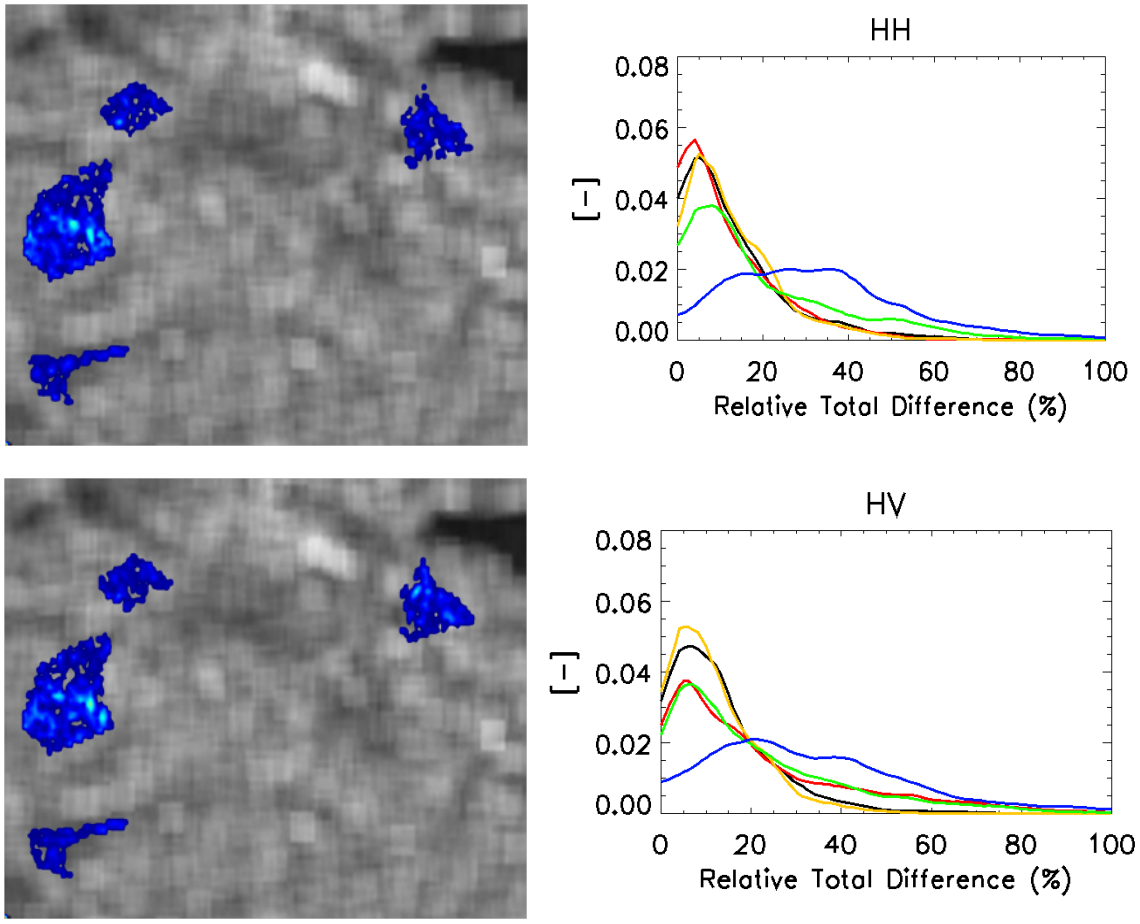

Figure 4.21 – Total integrated difference of the CT profiles in the wet day with respect to the dry day, expressed in %. Right panel: difference maps in range-azimuth for the areas of interest color-coded between 0% (blue) and 100% (red); right panel: normalized histograms of the integrated profile difference for the selected areas. Top panel: HH polarization channel; bottom panel: HV polarization channel.

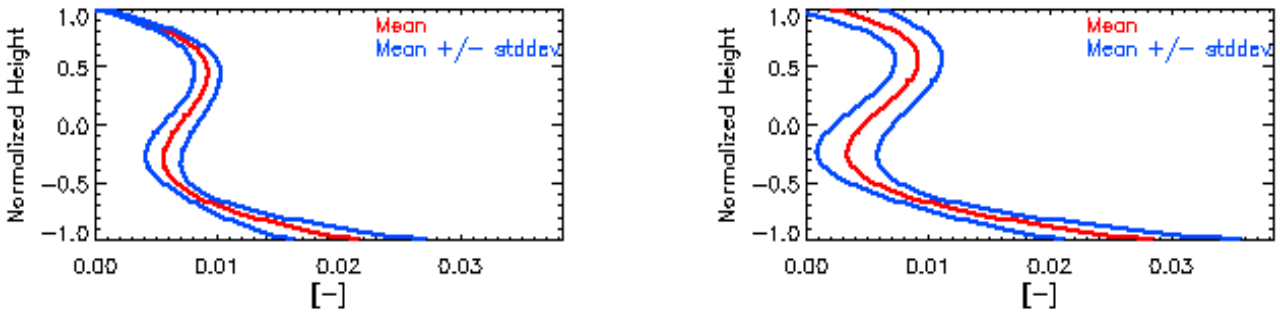

Figure 4.22 – CT average profiles, area no. 1, dry day (left) and wet day (right).

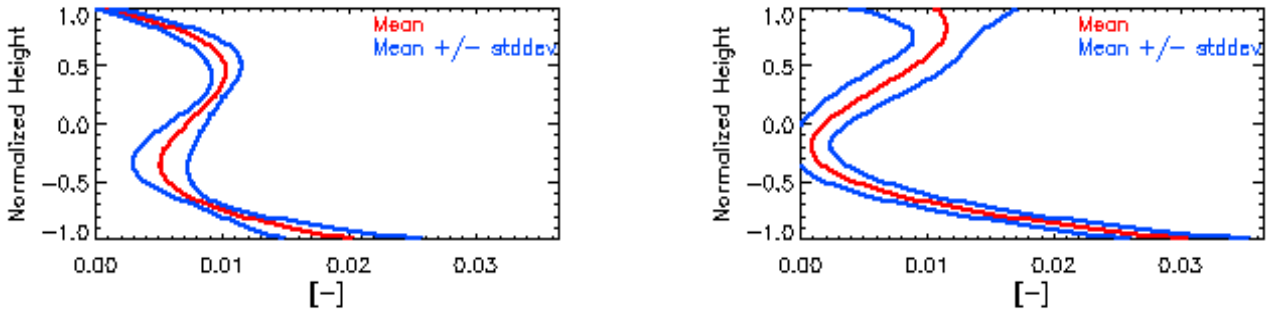

Figure 4.23 – CT average profiles, area no. 5, dry day (left) and wet day (right).

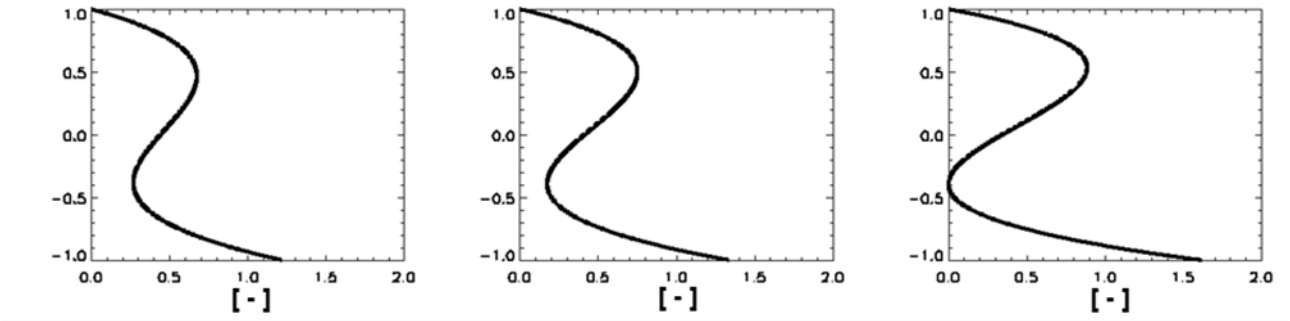

Figure 4.24 – CT simulated profiles, obtained by increasing the canopy extinction. Height (vertical axis) is in normalized units.

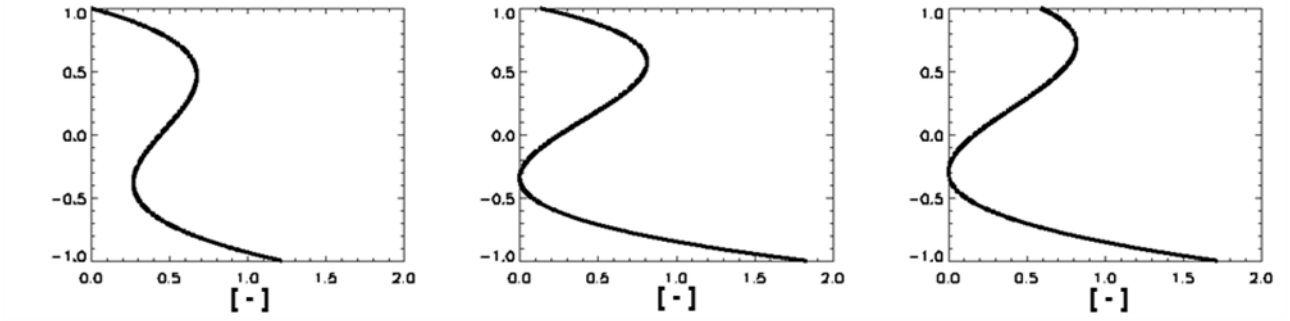

Figure 4.25 – CT simulated profiles, obtained by increasing the canopy phase center height. Height (vertical axis) is in normalized units.

4.5.6 Profiles estimated from mixed coherences

Differences between profiles estimated from data acquired in different weather conditions have been quantified in the previous sections. Considering a spaceborne single-pass (Pol)InSAR implementation in which the time between the passes is on the order of days/weeks, weather conditions can change at each revisit. For this reason, in this section coherences acquired in dry and wet conditions are mixed together to reconstruct the vertical structure, and the obtained profiles are compared to the profile obtained in dry conditions, taken as a reference. The histograms of the total difference ξ calculated according to equation (3.4) between the reference profiles and the mixed ones for the areas no. 1 and no. 5 are presented in Fig. 4.26. For all of the possible combinations of coherences, we fixed the coherence estimated at the longest baseline as the one set acquired in dry conditions. In this way, the height resolution was the same for each

combination, and it was identical to the one of the reference data set. In Fig. 4.26 only the HH results are shown, since no relevant differences were observed with the HV channel. In each plot, the green-coloured curves refer to combinations in which one coherence is "wet" and the remaining three are "dry". In the blue-couloured curves, two coherences are "wet", and two "dry". Finally, in the curve, three coherences are "wet" and one is "dry". Comparing the results of the two areas, an area-dependency, and consequently a structure-dependency, is apparent. Regarding area no. 1, low values of ξ are obtained for all the combination of coherences, with histograms centered around 5-10%. Regarding area no. 5, instead, some combinations produce histograms with relevant values also around 30-40%. It is also worth noting that there is no apparent relationship between the number of "wet" coherences and the amount of change of the profiles. Changing one coherence only can be worse than changing three.

A final remark is in order. This analysis has been carried out only within two stands. Therefore, it gives just a first insight on the change of the estimated profiles that can occur by mixing data acquired in different weather conditions. However, as in a spaceborne implementation of Tomo-SAR the weather conditions can change among different revisits, the effects of different environmental conditions have to been taken into account to avoid a misinterpretation of the obtained profiles.

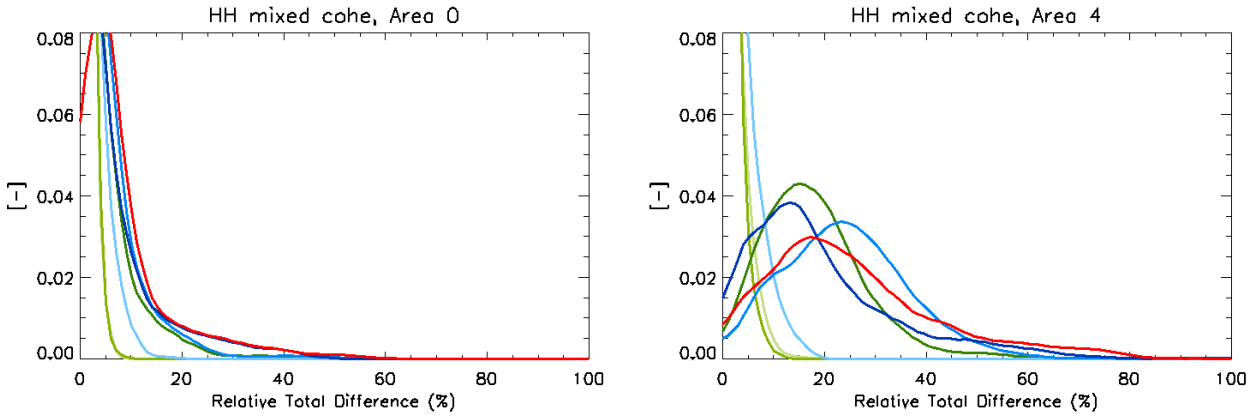

Figure 4.26 – Total integrated difference of the CT profiles obtained by mixing coherences acquired in different weather conditions, HH channel. Left panel: area no. 1. Right panel: area no. 5.

4.6 First results with a dual-baseline configuration

From an algebraic point of view, the CT inversion can estimate the first four coefficients even with only two baselines. This section investigates the accuracy of the CT inversion with a dual-baseline acquisition, taking as a reference the full-baseline inversion.

Remembering the simulated analysis of the inversion accuracy reachable by different dual baseline combinations (Section 3.2), and considering the baselines available from the TempoSAR campaign, two dual-baseline configuration have been chosen for further analyses. One of them will be called "*best*" configuration as it produced the best accuracy with simulated data. It is composed by the 10m and 25m baselines. The other one, called "*worst*" configuration, is composed by the 15m and 25m baselines, and it

was shown to be critical in terms of inversion accuracy. This section shows the differences between the reconstructed profiles, analyzing the coefficients estimated by the CT method. Only data acquired in dry conditions and in HV polarization are chosen to investigate the impact on CT inversion of different baseline configurations. As before, for this analysis the results about the same two areas are presented in Fig. 4.27 (area no. 1) and Fig. 4.28 (area no. 5). In the area no. 1, the dual-baseline coefficients estimated by the *best* configuration have a good correlation with the reference ones. Using the *worst* configuration produces a lower correlation than before, especially as regards the coefficient #3. For area no. 5, the correlation between the coefficients estimated by a dual-baseline set and the reference ones is very high for both *best* and *worst* configurations. This preliminary results confirm that a dual-baseline inversion is more sensitive to different structures than the full-baseline one. In conclusion, a dual-baseline implementation of CT with two baselines is possible, but the choice of the baselines is crucial to obtain a required accuracy.

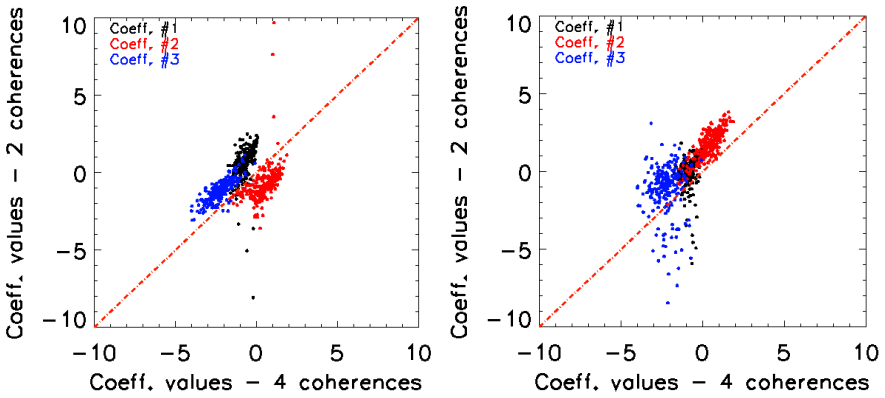

Figure 4.27 – Comparison of inverted coefficients, dual-baseline with respect to full-baseline, area no. 1. Left panel: best case. Right panel: worst case.

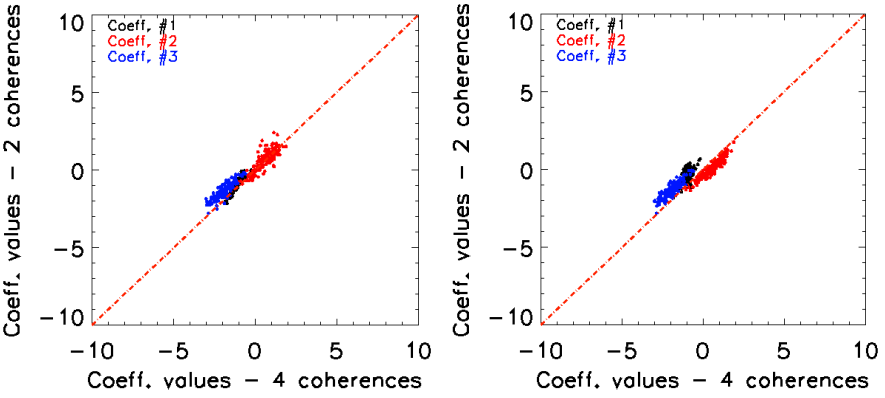

Figure 4.28 – Comparison of inverted coefficients, dual-baseline with respect to full-baseline, area no. 1. Left panel: best case. Right panel: worst case.

- This page intentionally left blank -

CHAPTER 5

CONCLUSIONS AND OUTLOOK

SAR tomography allows the resolution of different scatterers belonging to the same range-azimuth cell along the height dimension. In this framework, this work is focused on the performance obtainable in the estimation of forest vertical structure by means of SAR Tomography in the perspective of a space borne implementation. Moreover, since tomographic applications like biomass estimation needs the estimated vertical profile to be independent from environmental conditions, it is also investigated how tomographic methods are sensitive to different environmental conditions in order to understand and, if possible, correct their induced effects on the profiles. In this work, two tomographic methods are employed and analyzed with simulated data and real DLR E-SAR airborne data. The first method is the well-known adaptive beam forming (ABF, Capon-based) filtering, which reconstruct all of the vertical components of the profile. The second one is the CT technique that aims to reconstruct only the low vertical components of the profile. Considering a single-pass spaceborne interferometric implementation, as proposed by DLR for the Tandem-L mission, CT is a suitable algorithm to reconstruct the vertical structure above forest scenarios as it can process directly the single-pass temporal decorrelation-free coherences. A performance analysis with simulated data of the CT inversion has been presented in Chapter 3. Different baseline sets have been tested, concluding that problems of inversion are not expected in realistic acquisition scenarios (i.e. say 5 baselines with k_z lower than around 0.5). In principle, low frequency components of the profile can be reconstructed by means of a simple dual-baseline acquisition. For this reason, the CT inversion with different dual-baseline configurations has been investigated as well. The main result is that the ill-conditioning of the inversion can heavily affect the estimation of the profile. Unfortunately, this ill-conditioning depends on both the forest height and the baseline set.

Chapter 4 focuses on the analysis of weather-induced effects on the estimated profiles. Monitoring a forest area for a long time, it is important to recognize real changes on the vertical structure (for instance, due to deforestation) with respect to changes due to possible weather-induced changes. Operating with L-band

sensor above forest scenarios, the backscattering power is mainly governed by the water content inside and above the vegetation structure, which depends on the amount of rain among other different factors. For this purpose, considering the weather conditions during the campaign and the acquisition parameters, two days of the TempoSAR 2008 campaign have been chosen for this analysis. Indeed, one of them is clearly after a dry period, whereas the other one is after an important rainfall. Furthermore, the real baseline distributions along these two days have similar PSF, allowing a consistent analysis of the changes.

Considering the full-frequency components of the profiles estimated with ABF, clear effects due to rainfalls have been observed. From the top of the canopy layer, higher backscatterered powers have been observed (as expected), whereas the increase of the extinction produces stronger effects than the increase of the soil moisture, generally reducing the ground contribution, especially inside the areas with tall trees. After a more detailed analysis inside two selected areas of the test site with different biomass levels, an average decrease of ground-to-volume ratio ranging from 1dB to 1.5dB has been measured in the HH channel. Looking specifically to the Capon estimated profiles, also an increase of the phase center height has been observed ranging from 20% to 30% of the total structure height. Furthermore, it is worth noting that while the phase center generally increases (the 99% of points in some areas), the related ground-to-volume ratio can also increase, therefore indicating changes in the structure itself, not only in the extinction. Finally, the relative total difference between the profiles estimated by the two acquisition days has been quantified, and it reaches values around 10-30% for some areas, and can be higher than 80% for other areas. Generally, a lower sensitivity to different weather conditions of the HV channel with respect to HH has been observed.

The same analysis has been repeated for the CT inversion in the Legendre basis and considering only the low vertical frequency components. Looking at the two sets of estimated expansion coefficients, a relevant sensitivity to different vertical structures has been observed. Moreover, comparing the low vertical frequency components of the profiles estimated in different weather conditions, some differences have been found, and have been correlated to an increase of volume extinction, as in the full-frequency case. However, a lower sensitivity to weather conditions than the full-frequency profiles has been found. Indeed, the total profile differences are concentrated around the 10%, and rarely they are higher than 30%. Only the area with the highest level of biomass produces significant differences between the profiles. In conclusion, the all-frequency profiles are particularly sensitive to different environmental conditions, whereas the low-frequency ones vary at a lower extent.

Still in Chapter 4, it was pointed out that repeated single-pass InSAR spaceborne acquisitions can acquire coherences in different weather conditions. Therefore, the vertical profiles have to be estimated from "inhomogeneous" coherence sets. The impact of the inhomogeneity has been found to be dependent on the specific structure. For one of the selected areas, all of the tested combinations of coherences do not produce significant changes on the profiles with respect to reference ones (dry), whereas for a different area, even by changing only one coherence, the total difference between the profiles can reach values higher than 30-40%.

Finally, two different dual-baseline CT implementations have been tested. Comparing the CT coefficients estimated by each dual-baseline set with the coefficients estimated by the full-baseline set, non-

negligible deviations of the dual-baseline coefficients from the full-baseline ones have been observed for some areas and for some baseline configurations, confirming the analysis with simulated data carried out in Chapter 3. Therefore, dual-baseline configurations are hardly suitable for CT vertical structure inversion, at least with the Legendre polynomials.

In summary, it has been found that forest tomograms depend in general on the environmental conditions. Therefore, special care has to be taken when deriving products that exploit the "static" components of the vertical structure, for instance in the case that tomograms are used for estimating biomass, or for forest classification. On the other hand, it has also been seen that low vertical frequency components of the profile (that can be retrieved with a CT-based approach) are more insensitive to weather-induced changes, and therefore they represent an appealing direction of investigation.

- This page intentionally left blank -

REFERENCES

[*Ahern*, 1993] Ahern F. J., Leckie D. J. and Drieman J.A. (1993), *Seasonal changes in relative C-band backscatter of northern forest cover types*, IEEE Trans. Geosc. Remote Sensing, vol.31, pp. 668-680

[*Bamler*, 1998] Bamler R. and Hartl P. (1998), "Synthetic Aperture Radar Interferometry", Inverse Problems, vol.14, pp. R1-R54, August.

[*Berardino*, 2002] Berardino P., Fornaro G., Lanari R., and Sansosti E. (2002), *A New Algorithm for Surface Deformation Monitoring Based on Small Baseline Differential SAR Interferograms*, IEEE Transactions on Geoscience and Remote Sensing, vol. 40, no.11, pp. 2375-2383.

[*Bianco*, 2011] Bianco V., Pardini M. and Papathanassiou K. (2011), *Phase Calibration of Multi-Baseline Pol-InSAR Data Stacks,* M.Eng. thesis work

[*Campbell*, 2002] Campbell J. B. (2002), *Introduction to Remote Sensing*, Taylor & Francis, London.

[*Capon*, 1969] Capon J. (1969), High resolution frequency wavenumber spectrum analysis, *Proc. IEEE*, vol.57, pp1408-1418.

[*Cloude*, 1992] Cloude S. R. (1992), *Uniqueness of target decomposition theorems in radar polarimetry*, in Direct and Inverse Methods in Radar Polarimetry, Part1, NATO-ARW, Boerner et al., Eds. Norwell, MA: Kluwer, pp. 267-296, ISBN 0-7293-1498-0.

[*Cloude*, 1998] Cloude S. R. and Papathanassiou K. P. (1998), *Polarimetric SAR Interferometry*, IEEE Transactions On Geoscience And Remote Sensing, vol. 36, no. 5, pp. 1551-1563.

[*Cloude*, 2003] Cloude S. R., Papathanassiou K. P. (2003), *Three-stage inversion process for polarimetric SAR interferometry*, IEEE Proc.-Radar Sonar Navig., vol. 150, no. 3, pp. 125-134.

[*Cloude*, 2006] Cloude, S. R. (2006), *Polarization coherence tomography*, *Radio Sci., 41,*

RS4017.

[*Cumming*, 2004] Cumming I. G. and Wong F.H. (2004), *Digital Processing of Synthetic Aperture Radar Data, Algorithms and Implementation*

[*Dobson*, 1991] Dobson M. C., Pierce L., McDonald K. and Sharik T. (1991), *seasonal change in radar backscatter from mixed conifer and hardwood forest in Northen Michigan*, Proc. IGARSS 91, pp. 1121-1124

[*Fornaro*, 2003] Fornaro G., Serafino F., and Soldovieri F. (2003), *Three Dimensional Focusing With Multi-pass SAR*, IEEE Transactions on Geoscience and Remote Sensing, vol. 41, pp. 507-517.

[*Fornaro,* 2005] Fornaro G., Lombardini F.and Serafino F. (2005), *Three-Dimensional Multipass SAR Focusing: Experiments with Long Term Data*, IEEE Transactions on Geoscience and Remote Sensing, vol. 43, no. 5, pp. 702-714.

[*Freeman*, 1998] Freeman A. and Durden L. (1998), *A Three-Component Scattering Model for Polarimetric SAR Data*, IEEE Transactions On Geoscience And Remote Sensing, vol. 36, no. 3, pp. 963-973.

[*Garestier*, 2010] Garestier F. and Toan T. L. (2010), Forest Modelling For Height Inversion Using Single-Baseline InSAR/POL-InSAR Data, *IEEE Trans. Geosci. Remote Sens., 48,* 1528-1539.

[*Gini,* 2002] Gini F., Lombardini F. and Montanari M. (2002), *Layover Solution in Multibaseline SAR Interferometry*, IEEE Trans. On Aerospace and Electronic Systems, Vol. 38, No.4, pp. 1344-1356

[*Gini*, 2005] Gini F., Lombardini F. (2005), *Multibaseline Cross-Track SAR Interferometry: A Signal Processing Perspective*, IEEE Aerospace and Electronic Systems Magazine, vol. 20, no. 8, pp. 71-93.

[*Hinckley*, 1978] Hinckley T. M., Lassoie J. P. and Running S. W. (1978), *Temporal and Spatial Variations in the Water Status of Forest Trees*, Bethesda: Soc. Of Am. Foresters, 71 pp.

[*Horton*, 1919] Horton R. E. (1919), *Rainfall Interception*, Month Weather Rev., vol 47, pp. 603-623

[*Lee*, 2011] Lee S.K., Kugler F., Papathanassiou K., Hajnsek I (2011), *Multibaseline Polarimetric SAR Interferometry Forest Height inversion Approaches*, Proc. of ESA POLINSAR Workshop, Frascati (Italy).

[*Li*, 1996] Li J. and Stoica P. (1996), *Efficient Mixed-Spectrum Estimation with Applications to Target Feature Extraction*, IEEE Trans. On Signal Processing, vol. 44, No. 2, pp. 281-295

[*Lombardini*, 2003] Lombardini F.and Reigber A. (2003), *Adaptive Spectral Estimation for Multibaseline SAR Tomography with L-Band Data*, Proc. of 2003 IEEE

International Geoscience and Remote Sensing Symposium (IGARSS), Tolouse (France).

[*Lombardini*, 2005] Lombardini, F. (2005), Differential tomography: A new framework for SAR interferometry, *IEEE Trans. Geosci. Remote Sens., 43*, 37-44.

[*Lombardini*, 2009] Lombardini F. and Pardini M. (2009), *Experiments of Tomography-Based SAR Techniques with P-band Polarimetric Data*, Proc. of ESA Pol-InSAR Workshop, Frascati, Italy

[*Lopez*, 2010] López-Martínez C., Alonso A., Fàbregas X., Papathanassiou K. P. (2010), *Ground topography estimation over forests considering Polarimetric SAR Interferometry*, pp. 3612-3615, IGARSS, Honolulu, Hawaii, USA.

[*Monteith*, 1965] Monteith J. L. (1965), *Evaporation and environment*, Symp. Soc. Expl. Biology, 19, pp. 205-234

[*Olmested*, 1993] Olmested C. (1993), *Alaska SAR Facility Scientific SAR User's Guide*

[*Papathanassiou*, 2001] Papathanassiou K. P., Cloude S. R. (2001), *Single-Baseline Polarimetric SAR Interferometry*, IEEE Transactions On Geoscience And Remote Sensing, vol. 39, no. 11, pp. 2352-2363.

[*Pardini*, 2006] Pardini, M. and Papathanassiou, K. P. (2001), *Robust Estimation of the Vertical Structure of Forests with Coherence Tomography*, Proc. of 2011 ESA PolINSAR Workshop, Frascati, Italy.

[*Pardini*, 2010] Pardini M. (2010), *Advances and Experiments of Tomographic SAR Imaging for the Analysis of Complex Scenarios*, Ph.D. Thesis, University of Pisa, Italy.

[*Pardini*, 2011] Pardini M. and Papathanassiou K. (2011), *Sub-Canopy Topography Estimation with Multibaseline Pol-InSAR Data: A RELAX-Based Approach*, Proc. of ESA FRINGE Workshop, Frascati, Italy

[*Pardini*, 2012] Pardini M. and Papathanassiou K. (2012), *Sub-Canopy Topography Estimation: Experiments with Multibaseline SAR Data at L-band*

[*Proisy*, 2000] Proisy E., Mougin E., Dufrene E. and le Dantec V. (2000), *Monitoring seasonal changes of a mixed temperate forest using ERS-SAR observations*, IEEE Trans. Geosc. Remote Sensing, vol. 38, pp. 540-552

[*Reigber*, 2000] Reigber A., Moreira A. (2000), *First Demonstration of Airborne SAR Tomography Using Multibaseline L-Band Data*, IEEE Transactions On Geoscience And Remote Sensing, vol. 38, no. 5, pp. 2142-2152.

[*Rignot*, 1994] Rignot E., Way J.B., McDonald K., Viereck L., Williams C., Adams P., Payne C., Wood W. and Shi J. (1994), *Monitoring of environmental conditions in Taiga forest using ERS-1 SAR*, Remote Sens. Environ., vol. 49, pp. 145-154

[*Rosen*, 2000] Rosen P., Hensley S., Joughin I. R., Li F. K., Madsen S. N., Rodriguez E. and R. M. Goldstein (2000), *Synthetic Aperture Radar Interferometry*, Proceedings

of the IEEE, vol. 88, pp. 331-382.

[*Lee*, 2013] Lee S.-K., Kugler F., Papathanassiou K. and Hajnsek I. (2013), *Quantification of Temporal Decorrelation Effects at L-Band for Polarimetric SAR Interferometry Applications*, IEEE Journal of Selected Topics in Applied Earth Observations and Remote Sensing.

[*Stoica*, 1997] Stoica P., Moses R.L. (1997), *Introduction to Spectral Analysis*, Prentice-Hall.

[*Tebaldini*, 2010] Tebaldini S., Monti Guarnieri A., *Methods and Performance for Multipass SAR Interferometry*, in Geoscience and Remote Sensing. New Achievements, Intech Online Publisher.

[*Tebaldini*, 2009] Tebaldini S. (2009), *Algebraic Synthesis of Forest Scenarios From Multibaseline PolInSAR Data*, IEEE Trans. on Geoscience and Remote Sensing, vol. 47, 2009.

[*Toraño*, 2010] Toraño Caicoya A. and Kugler F., *et al.* (2010), *Biomass estimation as a function of vertical forest structure and forest height. Potential and limitation for radar remote sensing*, Proc. of EUSAR

[*Ulaby*, 1987] Ulaby F. T. and EL-Rayes M. A. (1987), *Microwave dielectric spectrum of vegetation – Part II: dual-dispersion model*, IEEE Trans. Geosc. Remote Sensing, vol. 25, pp. 550-557

[*Way*, 1990] Way J., Paris J., Kasischke E., Slaughter C., Viereck L., Christensen N., Dobson M. C., Ulaby F., Richards J., Milne A., Sieber A., Ahern F. J., Simonett D., Hoffer R., Imhoff M and Weber J. (1990), *The effect of changing environmental conditions on microwave signatures of forest ecosystems: Preliminary results of the March 1988 Alaskan aircraft SAR experiments*, Int. J. Remote Sensing, vol.11, pp. 1119-1144